Modelling Lyman-α Emitters in the Epoch of Reionization

Author:
Emma Giovinazzo

Supervisors:
Dr. Maxime Trebitsch
Dr. Pratika Dayal

Abstract

Lyman-α emitters are a class of star forming galaxies selected for their strong emission in the Lyman-α line. These galaxies are uniquely useful to study the end of the Epoch of Reionization as light bluer than Lyman-α is absorbed by neutral gas and is therefore invisible during the EoR. However, Lyman-α is a resonant line, so its complex radiative transfer effects make the interpretation of the line challenging and require the use of appropriate radiative transfer codes for anything but the simplest gas distributions. I have used the RASCAS radiative transfer code to perform synthetic observations on a sample of galaxies from the OBELISK simulation at redshift $z = 6$ to study a variety of galaxy properties. I have also explored how the ionizing radiation escape fraction in the simulation compares to the value inferred from the Lyman-α spectrum. Lastly, I have studied how the dust distribution affects the Lyman-α line by comparing two different dust models, one where the dust follows the metals and another one where the dust was taken directly from OBELISK. Overall, I have concluded that weak trends seem to exist between observable and intrinsic properties, with a large scattering possibly due a large variation in galaxy properties and that my sample only partially follows the relation between Lyman-α peak separation and ionizing radiation escape fraction. Moreover, the two dust models produce similar results, although with a small systematic effect hinting that the models might start diverging at high gas masses, and some spatial variation.

Acknowledgements

I would first like to thank Prof. Dr. Pratika Dayal for suggesting this project to me, and Dr. Maxime Trebitsch for being a great supervisor, for all the invaluable insight on the topic, and for always be willing to help with any issue that arose.

I would also like to thank Dr. Valentin Mauerhofer for providing me with the ionizing radiation escape fractions, as they were an indispensable part of this project.

Lastly, I would like to thank Nidhi Bangera for the emotional support and Thijs van Beers for always being willing to hear me rambling about this project and pose as a rubber duck.

Contents

Chapter 1

Introduction

The Epoch of Reionization is a milestone in the history of the Universe, as during this time the Universe underwent its last phase transition, the transitions of intergalactic gas from cold and neutral to hot and ionized (Dijkstra 2014). This period also marks the formation of the first luminous objects (Fan et al. 2006), which formed at the center of collapsed halos and produced high amounts of ionizing radiation, which started the ionization process. Overall, the transition was driven by objects emitting ionizing radiation (eg Barkana et al. 2001, Zaroubi 2012, Dayal et al. 2018), such as young stars or AGN, but it is not clear exactly how this took place or even how long this transition took.

A schematic representation of the timeline of the Universe is shown in fig. 1.1. In this figure we see the Universe start from the Big Bang, then progress through Recombination, which is the first phase transition, when the gas in the Universe became completely neutral, the Dark Ages, the formation of the first objects and then the Epoch of Reionization, which ionized once more the gas in the Universe, before reaching present day.

It is commonly believed that the main source of the reionization of hydrogen in the Universe is massive star formation in galaxies, as young and massive stars emit copious amounts of ionizing radiation. In this scenario, galaxies are able to ionize gas in their surroundings, forming growing bubbles of ionized gas around themselves until these bubbles overlap and the entirety of the intergalactic medium (IGM) will be ionized (Laursen 2010). As far as how long this whole process took, current constrains place the Epoch of Reionization around redshift z>12 to z≈6 (Planck Collaboration et al. 2016) but it is very challenging to set strong limits.
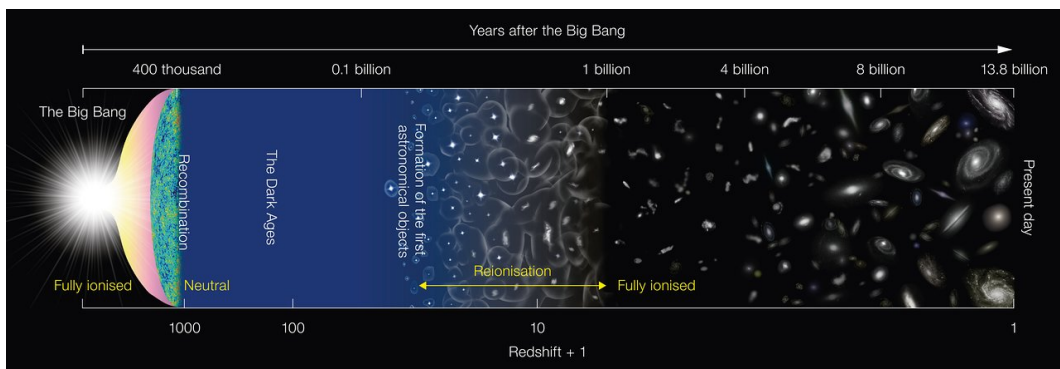

Figure 1.1: Timeline of the Universe. The first astronomical objects were formed during the Epoch of Reionazation. Credits: ESO/NAOJ

1.1 Constraints to the Epoch of Reionization

Setting these constraints is a problem that can be approached in multiple ways such as using the spectra of quasars, the CMB, and other methods. Observations of Gunn-Peterson troughs (Gunn et al. 1965) in the spectra of quasars (Wyithe et al. 2005, Fan et al. 2006, Schroeder et al. 2012, Becker et al. 2015) at redshift z>6 make it possible to infer that the Universe should have been fully ionized by redshift z≈6. This trough, just blueward of Lyman-α, where the flux goes to 0, is due to the presence of neutral hydrogen in the IGM, and therefore means that the space between quasar and the observer was not ionized yet and that reionization was not yet complete (Fan et al. 2006). The Gunn-Peterson effect can thus directly constrain the ionization state of the IGM. At around redshift z≲6 these troughs are replaced with a Lyman-α forest, whose presence indicates transmitted flux and therefore that there is ionized space around the object being observed.

The CMB can also be used to try to constrain the start of reionization, as it is affected by the total column density of free electrons along each line of sight, which is parametrized by the Thompson scattering optical depth τ, one of the six parameters at the baseline of the ΛCDM cosmological model, measured by the Planck Collaboration (Planck Collaboration et al. 2016). Their measurements, together with the constraints from lensing and Baryonic Acoustic Oscillations, would place the start of reionization at around z≈12. The method used by Planck Collaboration et al. 2016 assumes "instantaneous" reioniziation, meaning that they assume a redshift-symmetric reionization transition, and is therefore only an estimate.

Other methods to determine the constraint of reionization focus mostly on determining the end of the Epoch of Reionization and seem to agree with the limits brought forward by the Gunn-Peterson effect studies. Some of these methods are the measurements of the IGM temperature and thermal state evolution, the observation of Lyman-α damping wing in gamma ray after burst spectra and the observation of Lyman-α emitting galaxies (Fan et al. 2006, Dijkstra 2014).

The IGM temperature calculations use the fact that photoionization of neutral photons leaves an imprint on the IGM temperature itself (Raskutti et al. 2012). Reionization will in fact heat the IGM to several times 10^4 K and then the IGM will cool due to Hubble expansion. However, due to the long cooling time, the IGM will keep a thermal memory of the event, which leads to cooler IGM at lower redshifts in case of earlier reionization (Fan et al. 2006). The observation of the IGM temperature around multiple quasars at various redshifts can be thus used to constrain the redshift at which reionization was completed, as each observation gives a maximum redshift at which the gas around the specific source could have been ionized. While this method agrees with the Gunn-Peterson effect constraint, interpreting the results of these observations is complicated by the IGM heating due to the reionization of HeII, which happened at lower redshift (Sokasian et al. 2002).

Observations of the red side of the Lyman-α line from gamma ray bursts afterglow can also be used to constrain the global neutral fraction of the IGM, although with quite a large uncertainty (McQuinn et al. 2008). In theory this is possible because in the case of a gamma ray bursts coming from the Epoch of Reionization most optical and near-infrared light will be obscured by the Lyman-α forest, which should enable a strong constraint on the on the neutral fraction of the IGM at the burst's redshift (McQuinn et al. 2008).

Lyman-α emitters can also be used to determine the end of reionization, as LAEs observed in the Epoch of Reionization are expected to have a strongly attenuated Lyman-α emission and their Lyman-α profiles should have a stronger red wing (Fan et al. 2006). A magnitude deficit was noticed in the bright end, as that is the only constrained part, of the luminosity function of LAEs when compared to lower redshifts just outside of reionization, which is interpreted to mean that the light was not able to reach us due to the Universe being partially neutral (Kashikawa et al. 2006).
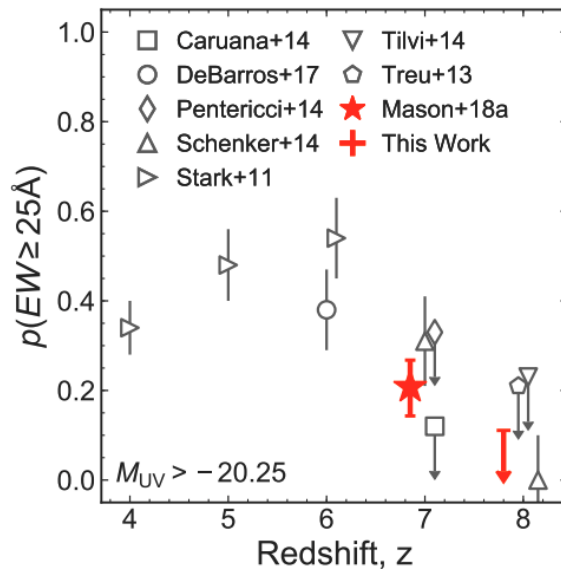
Figure 1.2: Redshift evolution of the Lyman-α fraction taken from Mason et al. 2019. It it possible to notice the decline in Lyman-α emitting galaxies as the redshift increases.

1.2   Lyman-α Emitters

Lyman-α Emitters (LAEs) are a class of galaxies notable for their Lyman-α emission, as they are particularly bright in the Lyman-α line. According to Partridge et al. 1967, as much as 6 to 7 % of the total galaxy luminosity can be converted to Lyman-α luminosity in a Milky Way mass halo (Dijkstra et al. 2020). This is because of their star forming nature (Dijkstra 2014), as will be explained in more details in the upcoming section, where the mechanisms of emission of the Lyman-α line will be explained and the connection between a high Lyman-α emission and young, star forming regions will become apparent.

LAEs have been observed and studied at low redshift (Orlitová et al. 2018), although they are quite rare in the nearby universe (Hayes 2015), but, as already mentioned, are particularly interesting when used to study the Epoch of Reionization (EoR), both as probes of the ionizing fraction of the IGM and as contributors of reionization.

Lyman-α is a resonant line, meaning that photons at Lyman-α frequency are absorbed by neutral hydrogen and then quickly re-emitted (eg. Dijkstra 2014), in a process extremely similar to scattering, called resonant scattering. Resonant scattering has the peculiarity, unlike normal scattering, to slightly change the frequency of the photon being scattered. The intergalactic medium in the Epoch of Reionization was mostly neutral, which makes it very challenging for the photons emitted at that time to reach us, since they will be unlikely to escape the neutral gas. This adds a layer of difficulty to the study of this kind of galaxies at this point in the history of the Universe and we do indeed see that the fraction of visible galaxies with Lyman-α emission decreases with increasing redshift (Mason et al. 2019), as shown in fig. 1.2. However, although this characteristic of the Lyman-α line makes LAEs difficult to observe at high redshift, it is also what makes LAEs great candidates to study the evolution of the neutral hydrogen fraction in the Universe (Ouchi et al. 2020), as already discussed in section 1.1.

Another, possibly more important, reason to study LAEs in the Epoch of Reionization is their role in the reionization of the Universe. The escape of Lyman-α photons is expected to be correlated with the escape of ionizing photons, as they are expected to escape from similar channels of low neutral hydrogen column density (Gazagnes et al. 2020), and therefore LAEs are expected to be contributors to the reionization of the Universe.

3

1.3   This work

In this work I have studied models of LAEs in the context of the Epoch of Reionization using synthetic observations of the Lyman-α emission in a cosmological galaxy formation simulation, the OBELISK simulation. My main goal was to connect the synthetic observation to various intrinsic galaxy properties, such as the escape fraction of Lyman-α photons, the intrinsic luminosity and the mass. Another goal of this work was to compare the ionizing radiation escape fraction intrinsic to the galaxies to that calculated with an empiric relation, as the ionizing radiation escape fraction is a very valuable quantity to the study of the Epoch of Reionization. Lastly, I studied the impact of dust physics on the properties of the Lyman-α line, by comparing two different dust models, one where the dust was added later, following the metals, and one where the dust is taken directly from the simulation.

This work will be structured as follows. In chapter 2 I will delve deeper into the theory of LAEs and especially the Lyman-α line itself. I will talk about the mechanisms that lead to the emission of Lyman-α photons, how these photons transfer through neutral gas and how LAEs can be modelled to aid our understanding of this class of galaxies. Then, in chapter 3, the Monte Carlo method and the RASCAS radiative transfer code will be detailed. Here I will also explain the setup used to perform the radiative transfer, the method used to create the synthetic observations and how I have calculated various quantities from the results of the radiative transfer code. Chapter 4 will cover the most interesting results achieved with the RASCAS code for a set of galaxies taken from OBELISK. Here I will go into details on the conditions of creation and escape of the photons, I will analyze the spectra, discuss the properties of the Lyman-α line, estimate the ionizing radiation escape fraction from the spectra, and compare the two dust models. Lastly chapter 5 will present the main conclusions and some improvements and follow up research that could be performed with the same methods used here.

Chapter 2

Physics of Lyman-α

As Lyman-α emitters are identified by their Lyman-α line, the first step towards understanding their physical properties is to understand the physics of the Lyman-α line.

The Lyman-α line, discovered in 1906 by Theodore Lyman, is the first line in the Lyman series, which is a series of radiative transitions in the hydrogen atom which happen when the electron decays from $n \geq 2$ to $n = 1$ (eg. Dijkstra et al. 2020). Lyman-α being the first in the series, it is the transition from $n = 2$ to $n = 1$, which emits a photon at wavelength λ = 1215.67 Å. To add some clarity, in this context n is the principal quantum number and it represents the energy levels the electrons can take within the atom.
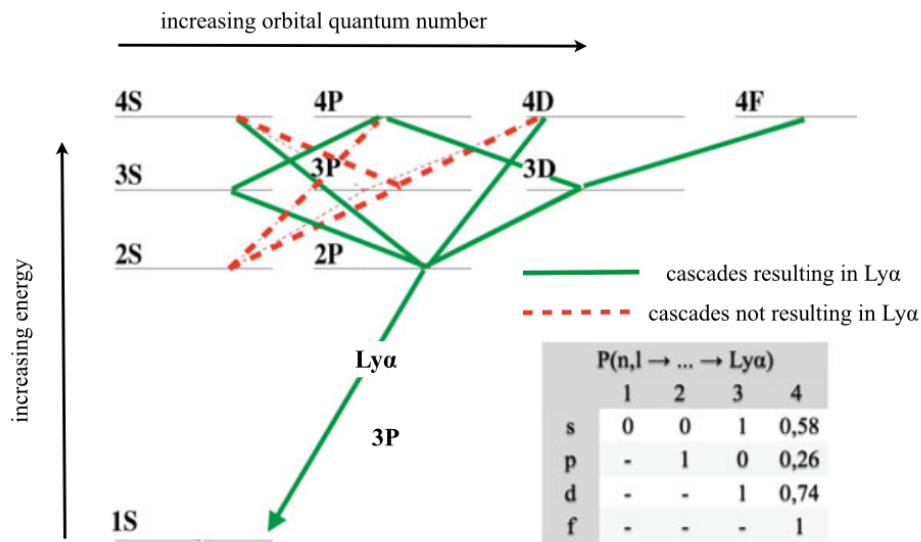

Figure 2.1: Radiative cascade paths of electrons from excited states to stable states. In green is the path that leads to Lyman-α emission and in red is the cascade path to the $2s$ state, which does not produce Lyman-α, as the transition $2s \to 1s$ is forbidden. Credits: Dijkstra 2014

The path that the electron can take while cascading from higher values of n to the ground state is shown in figure fig. 2.1, with the path leading to Lyman-α emission shown in green. In this figure we can see more distinction within the levels given by the primary quantum number, represented by letters. These letters correspond to sublevels of the energy levels, and they represent the angular momentum quantum number, which represents the shape of the orbital in which the electron resides (Morrison 2015).

In fig. 2.1 we also see a red dashed line, which represents a cascade not emitting Lyman-

α. This cascade differs from that represented with the green solid line as it does not end up in the $2p$ state but in the $2s$ state, and only electrons cascading to $2p$ will be able to reach the ground state, as only transitions of the form $|\Delta l| = 1$ are allowed by "selection rules" (Griffiths et al. 2018). Realistically, all the electrons do end up decaying to the ground state, since forbidden transitions can happen with the emission of two photons rather than one, but what is important in this context is that this transition is improbable and it will not produce Lyman-α photons.

We will now review the mechanisms through which an hydrogen atom can be excited to states of $n > 1$. There are two main mechanisms to achieve this, recombination and collision (Dijkstra et al. 2020), both of which will be analyzed in this chapter.
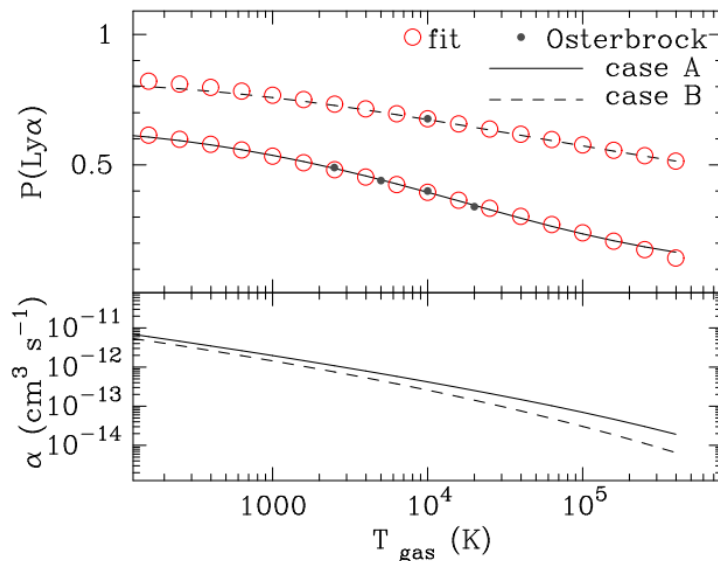

Figure 2.2: The top panel shows the probability that a recombination event will lead to Lyman-α emission, as a function of the gas temperature. The bottom panel shows the recombination rate, still as a function of the gas temperature. In both panels the solid line represent case A recombination and the dashed line represents case B recombination. Credits: Dijkstra 2014

Recombinations

One way to put an electron in an excited state in an hydrogen atom is through recombination, which is the capture of an electron by a proton, following the ionization of hydrogen by hot young stars. Not all recombination events can lead to Lyman-α emission (Dijkstra 2014), as already shown in fig. 2.1, and the percentage of recombination that actually emits Lyman-α is shown fig. 2.2 as a function of temperature, and it about 68 % at a temperature of 10^4 K. In this figure, case A indicates recombination that takes place in a medium that is optically thin to all photon frequencies and case B indicates a medium which is opaque to all Lyman series photons and to ionizing photons emitted following direct recombination (Dijkstra 2014). Here and in the rest of this work, only case B recombination will be taken into account, as galaxies are generally optically thick to Lyman radiation.

The production rate of photons following recombination is (Dijkstra 2014)

$$R_{rec}^{Ly\alpha}(n, T) = P(Ly\alpha)n_e n_p \alpha_B(T)\text{cm}^{-3}\text{s}^{-1} \qquad (2.1)$$

where n_e and n_p are the number density of free electrons and protons, $\alpha_B(T)$ is the recombination coefficient, and $P(Ly\alpha)$ is the fraction of recombination events resulting in Lyman-α

(Dijkstra [2014]), which can be read off fig. 2.2 for any given temperature. The relation between the gas temperature and the probability of Lyman-α emission after ionization was derived by Dijkstra [2014] but it is out of the scope of this section to present it in full.

Collisions

The other mechanism responsible for the excitation of an electron in an hydrogen atom is collisions, although this kind of emission contributes much less to the overall Lyman-α emission of a galaxy than the emission coming from recombination. A Lyman-α photon can be created when the hydrogen atom collides with an electron, which, depending on the respective kinetic energies, is a process that could leave the hydrogen atom in an excited state. This process is known as collisional excitation.

Once the electron finds itself in an excited state, if it is in the state $2p$, it can cascade down to the ground state and emit a Lyman-α photon, as explained earlier. Due to the nature of this process, the total Lyman-α production rate is dependent on the number density of both hydrogen and free electrons and on the relative velocity of the two particles. The Lyman-α photon emission rate following collisional excitation is then given (Dijkstra et al. [2020])

$$R_{coll}^{Ly\alpha}(n,T) = n_e n_{HI} q_{1s2p}(T) \text{cm}^{-3}\text{s}^{-1} \tag{2.2}$$

where q_{1s2p} quantifies the velocity dependence of the process, and it is generally defined as (Dijkstra et al. [2020])

$$
\begin{aligned}
q_{lu}(T) &= \frac{h_P^2}{(2\pi m_e)^{3/2}(k_B T)^{1/2}} \frac{\langle \Omega_{lu}\rangle(T)}{g_l}\exp\left(-\frac{\Delta E_{lu}}{k_b T}\right) \\
&= 8.63 \times 10^{-6} T^{-1/2} \frac{\langle \Omega_{lu}\rangle(T)}{g_l}\exp\left(-\frac{\Delta E_{lu}}{k_b T}\right) \text{cm}^3\text{s}^{-1}
\end{aligned}
\tag{2.3}
$$

where l and u indicate respectively the upper and lower energy state and $\langle \Omega_{lu}\rangle(T)$ is the velocity averaged collision strength.
Calculating the collision strength is complex, due to the possible occurrence of quantum mechanical interactions, so there is still some uncertainty in the collisional excitation rates (Dijkstra et al. [2020]).

Line Profile

To fully understand Lyman-α emission we also need to take its line profile into account. This is particularly important for Lyman-α, unlike for non-resonant lines because the absorption cross section, which plays a role in the resonant scattering, as the same line shape, as we will see later. The Lyman-α emissivity will then be

$$j(n,T,\nu) = R^{Ly\alpha}\phi(\nu)E_\alpha/(\sqrt{\pi}\Delta\nu_D) \tag{2.4}$$

where $E_\alpha = 10.2$ eV is the energy of a Lyman-α photon, $\phi(\nu)$ is the Voigt profile, which is the shape of the Lyman-α profile, shown in fig. 2.3, and $(\sqrt{\pi}\Delta\nu_D)$ is the normalization of the Voigt profile, with $\Delta\nu_D = 1.1\times 10^{11}(T/10^4 K)^{1/2}$ Hz being the thermal broadening of the line. The Voigt profile is described as (Dijkstra [2014])

$$\phi(x) = \int_{-\infty}^{+\infty} dy \frac{\exp(-y^2)}{(x-y)^2 + a_V^2} \tag{2.5}$$

where a_V is the Voigt parameter and x is a dimensionless variable defined as $x \equiv (\nu - \nu_\alpha)/\Delta\nu_D$, with $\nu_\alpha = 2.46 \times 10^{15}$ Hz, which is the frequency corresponding to Lyman-α. The variable x is a common and simple way to represent the frequency shifts of photons with respect to the central Lyman-α frequency. The particular shape is due to the natural Lorentzian line shape in the frame of the hydrogen atom emitting the photon and its velocity, drawn from a Maxwellian distribution (Dijkstra et al. [2020]).
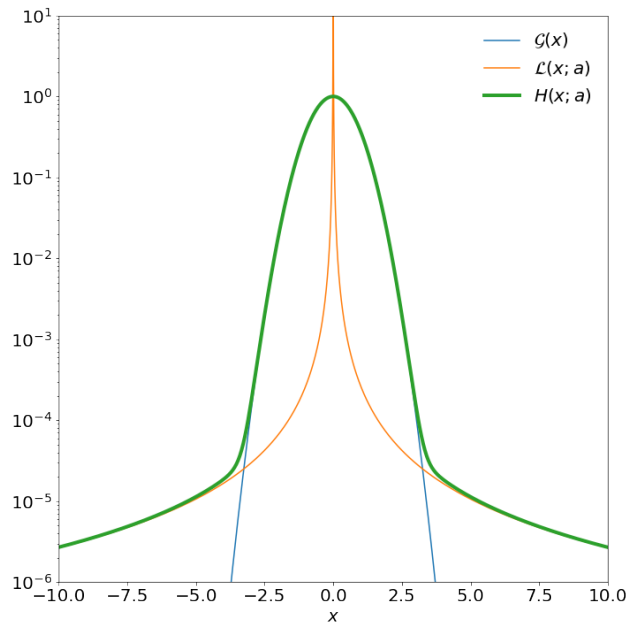
Figure 2.3: Voigt profile (green) shown together with the Gaussian (blue) and Lorentzian (orange) profiles, which are the two components of the Voigt profile, for a temperature of T=10^4 K. Here we can see the change from Gaussian to Lorentzian at $x \approx 3.2$.

These two very different mechanism of Lyman-α production imply that Lyman-α photons are created in different environments. In fact, with Lyman-α is possible to observe both HII regions of star formation and AGN but also the neutral gas in the circum-galactic and intergalactic medium (Ouchi et al. 2020).

Photons created through the recombination mechanism require the presence of ionized gas, which can be found in interstellar HII regions, created by massive young star, which are bright in the UV and are therefore able to produce a lot of ionizing radiation to ionize the gas around them. This makes it clear that a strong Lyman-α emission is a good indicator of star formation, as star formation is inherently linked to the Lyman-α radiation coming from recombinations, which is the strongest component in the emission, being orders of magnitude brighter than the radiation coming from collisions.

Photons created through collisions have instead a more diffuse origin, as they can be emitted anywhere neutral hydrogen and free electrons are present, and given that most of the interstellar medium is indeed neutral hydrogen (Saintonge et al. 2022), the Lyman-α emission created trough collisions can have more diffuse origins. It can in fact be emitted almost anywhere in the galaxy and is also expected to come from cold accretion streams (Rosdahl et al. 2012).

2.1 Lyman-α transfer

A peculiar characteristic of the Lyman-α line is its resonant nature, which means that that photons at Lyman-α frequency scatter on the neutral gas. To be more precise, Lyman-α photons, after they are emitted and encounter a neutral hydrogen atom, will be absorbed and instantly re-emitted, which is a process that effectively resembles scattering (Dijkstra 2014).

The Lyman-α absorption cross section is frequency dependent, and is described by a Voigt function, which has already been defined in eq. (2.5). The cross section is described
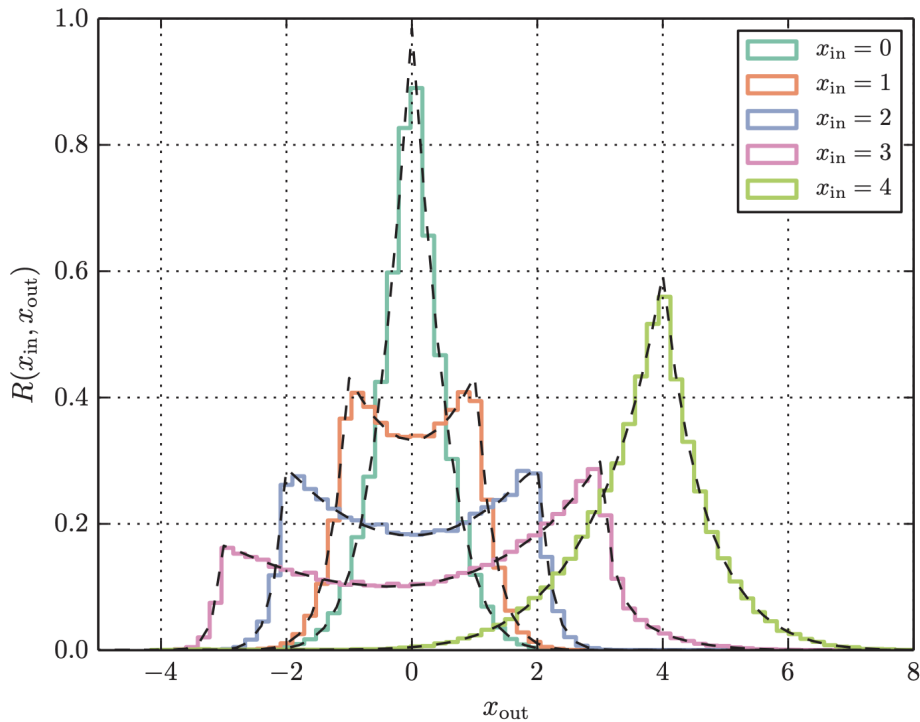
Figure 2.4: Redistribution functions, i.e. the probability a photon will have a frequency after scattering x_{out} for five different frequencies before scattering x_{in} after a partially coherent scattering event. Here is shown that photons in the core can slowly move to the wings, due to the Doppler shift caused by the atom's intrinsic motion, and that photons in the wings are extremely likely to stay in the wings. Credits: Dijkstra 2014

as

$$\sigma_0(x) = \sigma_0 \times \phi(x)$$
$$\sigma_0 = \frac{f_\alpha}{\sqrt{\pi}\Delta\nu_D}\frac{\pi e^2}{m_e c} = 5.88 \times 10^{-14}(T/10^4 K)^{-1/2}\text{cm}^2 \tag{2.6}$$

where f_α is the Lyman-α oscillator strength, σ_0 is the cross section at line center and x is the dimensionless variable previously defined.

This Voigt shape implies that photons near Lyman-α, in the 'core', will have a much higher cross section, so will be more likely to be absorbed and scattered, than photons in the 'wings', which are therefore less likely to scatter and more likely to escape the HI regions of the ISM and reach the observers. This transition between core and wings happens at $x \approx 3.2$ for a gas temperature of $T = 10^4$ K, (Dijkstra 2014) as can be seen from fig. 2.3, where we see the change from the Gaussian to the Lorentzian component happen around $x \approx 3.2$.

The scattering of Lyman-α is coherent in the frame of the atom (Laursen 2010), which means that the the energy at which the photon is absorbed is the same at which it is re-emitted, in the frame of reference of the atom doing the scattering. This is not necessarily the case for an external observer, in fact, due to the atom's thermal motion, the photon's energy will be Doppler boosted, making the frequency before and after scattering correlated but not identical (Dijkstra 2014). Depending on the velocity of the atom, this shift could be on either side of the core, moving the frequency of the photon slightly towards the wings of the Voigt profile. This Doppler shift helps the escape of the photon, especially when coupled with the fact that once a photon finds itself in the wings, so with $|x| > 3$, it will most likely remain in the wings after scattering (Dijkstra 2014). The redistribution functions for various
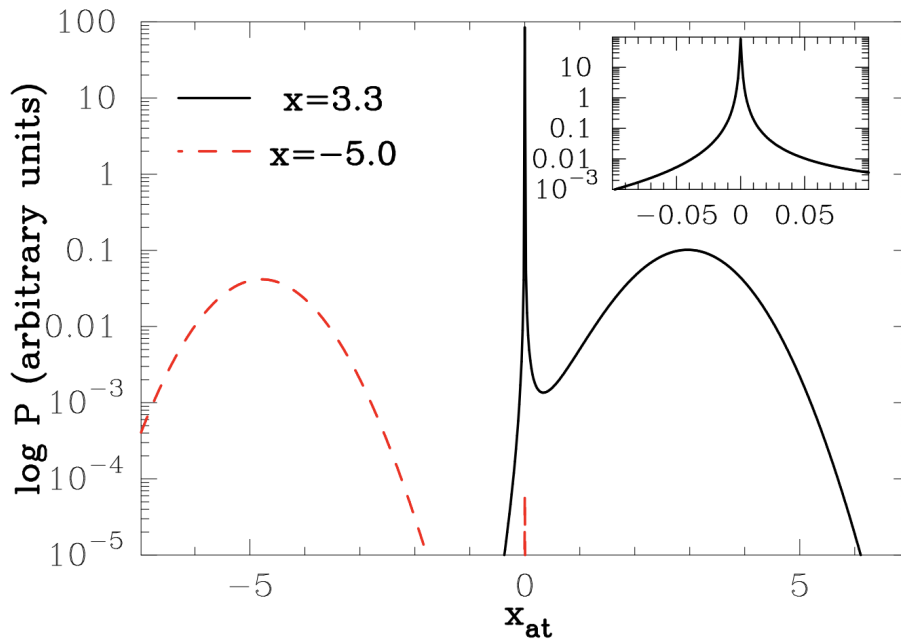
Figure 2.5: Probability that a photon is scattered by an atom which sees the photon at x_{at} in its frame of reference. The red dashed line is for photons of $x = -5$ and shows that it is unlikely these photons would be scattered resonantly but they are very likely scattered by atoms which see them in the wings. Photons at $x = 3.3$, the black line, are instead much more likely to be scattered by atoms which see them at resonance or at ~ 3. Credits: Dijkstra et al. 2008

incoming frequencies are shown in fig. 2.4. Here, for a selection of frequencies before the scattering, the possible frequencies after scattering are shown, and it shows that the two are clearly correlated but not identical, due to the partially coherent nature of the scattering. In this figure we can see that it is extremely likely that a photon incoming in the wings in the atom's frame of reference will stay in the wings after the collision, whereas a photon incoming at resonance frequency will have a small change in frequency and will stay close to resonance.

The reason why a photon which scatters in the wings stays in the wings is shown in fig. 2.5, where we see that for photons in the wings resonant scattering is very rare, as it is unlikely for an hydrogen atom to move at a velocity such that photons at this frequency will be seen as resonant, since the velocities of the atoms will be taken from a Maxwellian distribution. This is heightened the farther a photon is in the wing, as seen in fig. 2.5, where the probability of a photon at $x = -5$ to scatter resonantly is shown to be about six orders of magnitude less than for a photon at $x = 3.3$. The Doppler shift out of resonance, together with the fact that photons scattered in the wings tend to stay in the wings, gives Lyman-α profiles their typical double peaked shape, due to most of the photons scattering out of resonance on each side and into the wings.

This behavior of Lyman-α has strong consequences on its journey through space, since most of the interstellar medium is made of neutral hydrogen. This is especially true when the photon is coming from the densest parts of the galaxies, which are also those where star formation happens. Later we will indeed see that photons emitted from areas of diffuse HI around the galaxy itself are able to escape very easily, whereas photons created in dense, star forming areas are unlikely to escape the galaxy. Moreover, since the intergalactic medium still has a substantial neutral fraction in the Epoch of Reionization, this behavior of Lyman-α explains the IGM absorption mentioned earlier.
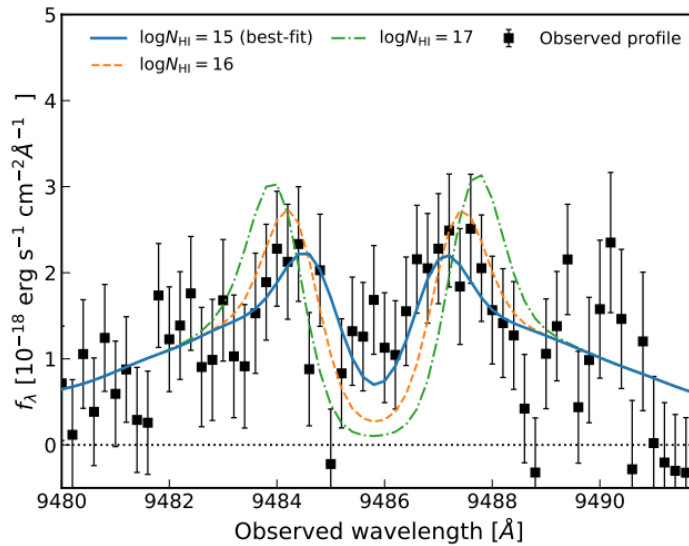
Figure 2.6: Double peaked Lyman-α profile observed from a galaxy at $z = 6.8$. In black are the data points and the colored lines are the comparison models, which assume Lyman-α transfer through non expanding shells of homogeneous gas. Credits: Meyer et al. 2020

All of these scatterings that a Lyman-α photons has to go through before being able to escape the galaxy and eventually reach the observers make the Lyman-α line an extremely complex probe of galaxy dynamics (Ouchi et al. 2020), as the location in the galaxy where Lyman-α is observed and where it is emitted can be quite different. However, this same behavior is what makes this line useful to investigate HI gas in and around high-z objects, which would be hard to probe with other observations (Ouchi et al. 2020).

Theory predicts that the ionizing UV radiation from a galaxy in the Epoch of Reionization could create an ionized bubble, which would allow the Lyman-α photons to escape, since at the edges of the bubble the neutral hydrogen will be redshifted out of resonance with the Lyman-α photons due to Hubble flow, aiding the escape of Lyman-α (Ouchi et al. 2020). This also means that it is possible to use Lyman-α to study the distribution of HI in the circum-galactic medium at the Epoch of Reionization (Ouchi et al. 2020), and possibly estimate the size of an ionized bubble around a galaxy, as it has been done by Matthee et al. 2018 and Meyer et al. 2020. Both works use the observation of a double peaked Lyman-α line into the Epoch of Reionization, respectively using galaxies at $z = 6.593$ and $z = 6.803$, and use the extension of the blue wing to determine the size of the bubble, as the blue part of a Lyman-α double peaked spectrum is expected to be completely absorbed by even a partially neutral IGM (Meyer et al. 2020). One of these double peaked profiles is shown in fig. 2.6. Moreover, whereas COLA-1, studied by Matthee et al. 2018, seems to only be able to maintain its ionized bubble with the help of some fainter neighbors, Meyer et al. 2020 suggest that A370p_z1 should be able to both create and maintain the ionized bubble on its own, making it possibly a representative of a population of luminous objects responsible for the end of cosmic reionization, which would be an extremely interesting category of galaxies to study. The results from these works highlight the importance of LAEs for the study of the Epoch of Reionization, as they directly show that galaxies contribute to the reionization of the Universe, by ionizing their surroundings.

2.2 Modelling LAEs

Because of the resonant nature of the line, creating a dependence of the observed spectrum on the complex geometry of the neutral gas and dust in the galaxy, interpreting Lyman-α

observations directly is difficult, but there are two possible approaches that can be taken to aid the interpretation of observations. These two approaches are the use of idealized geometries (eg Dijkstra et al. 2006, Verhamme et al. 2006), or the use of simulations, which are much more computationally expensive but are able to more closely describe the geometry.

The use of an idealized geometry to aid the interpretation of high redshift observations has been done by Meyer et al. 2020, and shown here in fig. 2.6. Here a simple model of static shells of homogeneous gas is used to estimate the column density of hydrogen and the Lyman Continuum escape fraction from the observation of a Lyman-α profile in a galaxy at $z = 6.8$.

The other approach that can be taken to study this class of galaxies and aid the interpretation of observations is through the use of simulations. Hydrodynamical simulations that extend to high redshift might be the key to link intrinsic properties of LAEs to their spectra, and learn more about this class of galaxies, when used together with radiative transfer codes which are able to accurately follow and describe the travel of a resonant photon through the galaxy.

This has been possible especially in the last few years, with early attempts already in 2012 which still used partially idealized models (Verhamme et al. 2012), now that large scale simulations exist that are also able to resolve the details of ISM physics, and add increasingly complex physics, such as the SPHINX simulation (Rosdahl et al. 2018). These simulations, when used with radiative transfer codes, offer the opportunity to create increasingly more accurate synthetic observations, as they can take into account various small scale processes but also cosmological processes, making these synthetic observations also very useful to interpret observations or test observational diagnostics (Michel-Dansac et al. 2020).

The simulations approach is indeed the one that was taken in this work. Starting from a sample of galaxies at $z = 6$ in the OBELISK simulation, a cosmological radiation-hydrodynamics simulation (Trebitsch et al. 2021), the radiative transfer was performed using RASCAS (**RA**diation **SC**attering in **A**strophysical **S**imulations), a 3D radiative transfer code developed to perform the propagation of resonant lines in simulations of astrophysical objects (Michel-Dansac et al. 2020). While performing the radiative transfer, the RASCAS code was also used to create synthetic observations of both images and spectra. The details of the method used to do this are presented in the next chapter.

Chapter 3

Radiative Transfer

3.1 Monte Carlo method

RASCAS uses the Monte Carlo method to perform the radiative transfer of both resonant lines such as Lyman-α and non resonant lines. This method propagates photons through a series of successive scattering events until they are able to escape, as schematically detailed in fig. 3.1. The Monte Carlo method is very useful to model the outcome of processes with too many random variables to be predicted, such as a resonant scattering. The method used in RASCAS and other Lyman-α modelling codes (eg. Cantalupo et al. 2005, Gronke et al. 2017) follows mostly the same workflow, which will be explained here following the description of the RASCAS code found in Michel-Dansac et al. 2020.

First, the sources are generated and photons, or "photon packets" are created from those sources. These Monte Carlo photons will represent a flux of photons, so an amount of energy per unit time. In RASCAS, the photon packets can be created from an ad hoc souce, from stars and from gas. When creating the photons from stars, different spectral shapes for the output photons can be implemented, which at the moment are a power-law to fit the stellar continuum, a monochromatic line, a gaussian emission line, or a tabulated version of the stellar continuum using the BPASS stellar library, which creates the most realistic spectra, but more could be added in the future. More relevant for Lyman-α emission is the ability to generate photons from gas. This code computes the Lyman-α emission directly from the simulation, when the ionization state of the gas is known, which it is in a simulation like OBELISK (Trebitsch et al. 2021), following the Lyman-α emission from both excitation mechanisms detailed in chapter 2. The two contributions to the Lyman-α emission, recombination and collision are treated separately and computed as follows. The number of Lyman-α photon emitted due to recombination per unit time from each gas cell is computed as

$$\dot{N}_{\gamma,rec} = n_e n_p \epsilon_{Ly\alpha}^B(T) \alpha_B(T) \times (\Delta x)^3 \tag{3.1}$$

where n_e and n_p are the electron and proton number densities, which can be read directly from the simulation, $(\Delta x)^3$ is the cell volume, the B stands for case B recombination (which is the only relevant case in this environment) as shown in chapter 2, α_B is the recombination coefficient given by

$$\alpha_B = 2.753 \times 10^{-14} \text{cm}^3\text{s}^{-1} \frac{\lambda_{HI}^{1500}}{(1 + (\lambda_{HI}/2.740)^{0.407})^{2.242}} \tag{3.2}$$

(Hui et al. 1997) and $\epsilon_{Ly\alpha}^B(T)$ is the fraction of recombination producing Lyman-α photons and it is given by the fit of Cantalupo et al. 2008

$$\epsilon_{Ly\alpha}^B(T) = 0.686 - 0.106\log(T_4) - 0.009 \times (T_4)^{-0.44} \tag{3.3}$$

The number of Lyman-α photons emitted from the gas per unit time in each cell due to collisions is given by

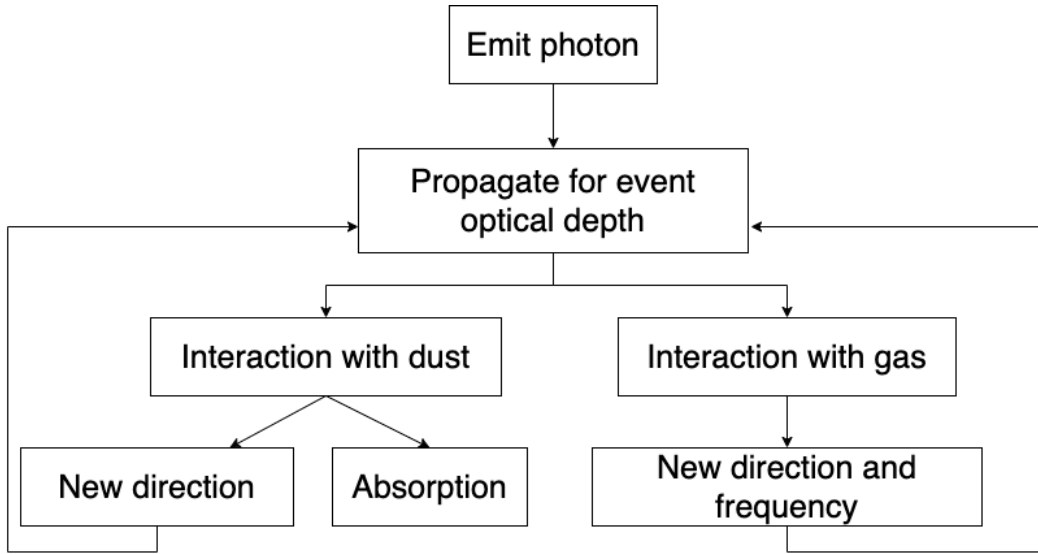$$\dot{N}_{\gamma,col} = n_e n_{HI} C_{Ly\alpha}(T) \times (\Delta x)^3 \tag{3.4}$$

Figure 3.1: Schematic of the Monte Carlo method used to perform the radiaitve transfer of Lyman-α photons.

where n_{HI} is the number density of neutral hydrogen atoms and $C_{Ly\alpha}$ is the rate of collisional excitation from level $1s$ to $2p$, and is given by

$$C_{Ly\alpha}(T) = \frac{2.41 \times 10^{-6}}{T^{0.5}} \left(\frac{T}{10^4}\right)^{0.22} \times \exp\left(-\frac{h\nu_{Ly\alpha}}{kT}\right) \mathrm{cm^3 s^{-1}} \tag{3.5}$$

(Goerdt et al. 2010).

Each photon packet is placed randomly in its emission cell, and given a random direction, assuming isotropic emission. Its wavelength is taken from a gaussian distribution centered around Lyman-α in the frame of the cell, with width of

$$\sigma_\nu = \nu_0 (2k_B T/m_p)^{1/2}/c \tag{3.6}$$

where k_B is Boltzmann's constant and m_H is the mass of an hydrogen atom. These values are stored in an initial condition file.

The optical depth to the next interaction is drawn from

$$\tau_{\mathrm{event}} = \ln(r) \tag{3.7}$$

where r is a uniformly distributed random number. The emitted photon will advance until the given optical depth is covered and there it will be scattered again.

To determine how far the photon will travel is necessary to determine the optical depth of the medium the photon will have to travel through. When travelling through a mixture of gas a dust, the total optical depth can be written as

$$\tau_{tot}(\nu) = \sum_X^{species} \sum_{lu}^{transitions} \tau_{X,lu}(\nu) + \tau_{dust}(\nu) \tag{3.8}$$

where ν is the photon frequency in the frame of the gas, X is the atomic or ionic species responsible for the scattering, only HI in the case of this work, and lu are the lower and upper levels for the transition, only $1s$ and $2p$ in this case. The two terms are calculated separately.

The optical depth contribution from the resonant scattering along a path of length ℓ through gas at a temperature T is defined as

$$\tau_{X,lu}(\nu) = \int_0^\ell n_{X,l} \sigma_{X,lu}(\nu, T) d\ell \tag{3.9}$$

where in the case of Lyman-α $n_{HI,1s}$ would be the number density of neutral hydrogen in the ground state and $\sigma_{HI,1s2p}(\nu, T)$ the cross section of the transition at frequency ν and temperature T. The cross section is given by a Voigt function, as seen in eq. (2.6).

The optical depth contribution from the dust is defined as

$$\tau_{dust}(\nu) = \int_0^\ell n_{dust}\sigma_{dust}(\nu)d\ell \tag{3.10}$$

where ℓ is the path through the dusty medium of length ℓ and n_{dust} and $\sigma_{dust}(\nu)$ are respectively the number density and cross section of the dust. These values are dependent on the model considered for the dust. Two different dust models have been considered for this analysis, one where the dust follows the metal and another one using the dust directly from the simulation. These two models are both relevant to the current studies of Lyman-α as most simulations lack a dust model, in which case the dust has to be approximated, which is where the dust model following the metals comes in useful. OBELISK, however, does have its own model for dust evolution, so this dust model can also be analyzed, and then the results from the two dust models can be compared. Here I would like to take a short intermezzo to go a bit more in depth on each model.

Dust from metals

The standard dust model used in RASCAS (which is the first model used in this analysis) follows the formulation of Laursen et al. 2009, which assumes a constant dust to metal ratio, since dust grains are built up from metals. In theory, it should be possible to calculate the result of a photon interacting with a dust grain of known properties, which are based on the respective metal abundances, by solving Maxwell's equations, but this is only possible for simple geometries. This method is commonly used since dust in hydrodynamical simulations is most often not included, as it is usually not necessary and creating a model for it can be difficult and time cosuming, so of course in those cases using the dust from the simulation is not possible.

The average extinction (and thus average cross section) of dust as a function of wavelength is known for the Large and Small Magellanic Clouds and the Milky Way, as well as their average metallicity, which is the basis that Laursen et al. 2009 use to scale their relation on, based on previous works by Pei 1992 and Gnedin et al. 2008.

For the Large Magellanic Cloud, which is the reference model used, Laursen et al. 2009 find that the extinction curve is slowly varying close to the Lyman-α and the effective cross section of dust per hydrogen atom can be approximated as

$$\sigma_d/10^{-21}\mathrm{cm}^2 = 0.723 + 4.46 \times 10^{-5}(T/10^4\mathrm{K})^{1/2}x \tag{3.11}$$

However, simulated galaxies will not necessarily have the same metallicity as the Magellanic Clouds, and within them each cell will have a different metallicity, which is why the dust density needs to be scaled by the metallicity with respect to the Large Magellanic Cloud metallicity, while also taking into account the ionization state of hydrogen, as dust destruction mechanisms become increasingly important at high temperatures. Since the cross section is expressed as a cross section per hydrogen atom, the relevant quantity is the hydrogen density, not the dust density, and assuming the extinction scales with metallicity, the pseudo number density of dust is given by the hydrogen density, a fraction of the ionized hydrogen, and the metallicity, as

$$n_d = (n_{HI} + f_{ion}n_{HII})\frac{\sum_i Z_i}{\sum_i Z_{i,0}} \tag{3.12}$$

where n_H is the hydrogen density, Z_i is the metallicity of element i in the galaxy of interest, $Z_{i,0}$ is the metallicity of element i in the Large Magellanic Cloud, and f_{ion} is a fraction of the ionized hydrogen, 0.01 in this case (Michel-Dansac et al. 2020). f_{ion} is needed in this analysis as using the entirety of the ionized hydrogen would mean ignoring the dust destruction mechanisms, which is not an assumption that can be taken.

The optical depth depth of gas and dust as seen by a propagating photon travelling a distance r will therefore be

$$\tau_{tot} = r(n_{HI}\sigma_x + n_d\sigma_d) \tag{3.13}$$

where the neutral hydrogen cross section is

$$\sigma_x = f_{12}\frac{\pi e^2}{m_e c \Delta\nu_D}\phi(x) \tag{3.14}$$

where f_{12} is the Lyman-α oscillator strength, and $\phi(x)$ is the line profile.

Dust from the simulation

OBELISK includes a subgrid dust model, which is treated separately from the metals. The main assumption used in this model is that all dust grains belong to a single population and are coupled to the gas, so they can be described by a single scalar describing the local dust mass fraction (Trebitsch et al. 2021).

The number density of dust in this description, follows the MRN distribution, which is characterised by

$$\frac{\mathrm{d}n}{\mathrm{d}a} \propto a^{-3.5} \tag{3.15}$$

where a is the grain size. Given that in a cell of volume Δx^3 the total mass of the dust is $M_d = \rho_d\Delta x^3$ and the total number of dust particles is $N_d = n_d\Delta x^3$, $n_d(a)$ for the MRN distribution will be

$$n_d(a) = \frac{\rho_d}{\frac{8}{3}\pi\mu_i(\sqrt{a_{max}} - \sqrt{a_{min}})}a^{-3.5} \tag{3.16}$$

where μ_i is the density of a dust grain and a_{max} and a_{min} are respectively the biggest and smallest dust grain sizes.

Using this we wish to calculate the dust optical depth over a path, and we will also need the dust extinction coefficient α^{ext} to do so, since $\tau^{ext} = \alpha^{ext}L = \rho_d\kappa_d L$. By definition α^{ext} is

$$\alpha^{ext}(\lambda) = \int_{a_{min}}^{a_{max}} \pi a^2 \sum_{i=s,c} n_d(a)Q_{ext}^i(a,\lambda)da \tag{3.17}$$

where s and c correspond respectively to carbonaceous grain and silicates grains, and Q_{ext} is the extinction efficiency factor evaluated by Weingartner et al. 2001 and Laor et al. 1993 respectively for the grain types. Given that L and ρ_d are known, this can be rewritten as

$$\begin{aligned}\kappa_d(\lambda) &= \int_{a_{min}}^{a_{max}} \sum_{i=s,c} \frac{a^{-3.5}\pi a^2 Q_{ext}^i(a,\lambda)}{\frac{8}{3}\mu_i(\sqrt{a_{max}} - \sqrt{a_{min}})}da \\ &= \sum_{i=s,c} \frac{3}{8\mu_i(\sqrt{a_{max}} - \sqrt{a_{min}})}\int_{a_{min}}^{a_{max}} a^{-1.5}Q_{ext}^i(a,\lambda)da\end{aligned} \tag{3.18}$$

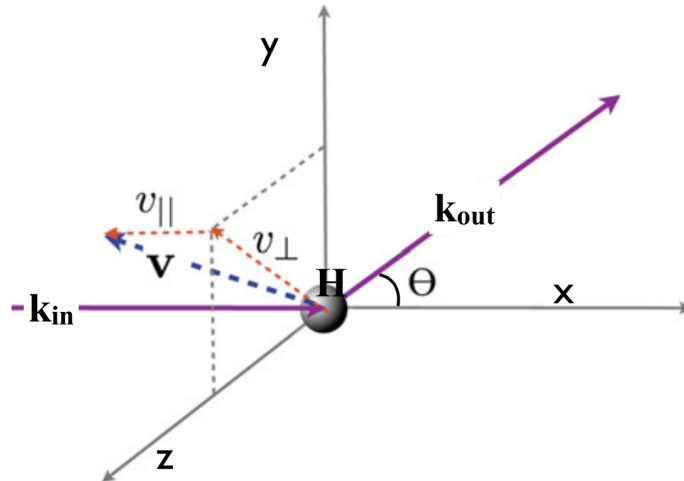to find the optical depth over a path due to the dust distribution.

Figure 3.2: Schematic representation of the coordinate system used when dealing with a resonant scattering. Credits Dijkstra et al. 2020

Once the photon has travelled through the determined τ_{event}, it will interact with something, which can be dust or an hydrogen atom. RASCAS can deal with three forms of interactions between photons and matter (Michel-Dansac et al. 2020), but only two of them are relevant for this work, which are resonant scattering and interaction with dust.

When a photon encounters a dust grain it will either be absorbed or scattered, based on the albedo of the dust grain, and there will be no frequency redistribution, unlike what happens in resonant scatterings. In the case of a scattering event, the direction of the outgoing photon will be calculated as

$$P_{HG}(\mu) = \frac{1}{2} \frac{1 - g^2}{(1 + g^2 - 2g\mu)^{3/2}} \tag{3.19}$$

(Henyey et al. 1941) where $\mu = \cos\theta$ and $g = \langle\mu\rangle$, which is the asymmetry parameter, which has been found to be close to $g = 0.73$ for Lyman-α (Li et al. 2001). This asymmetry parameter is needed because dust is observed to be forward scattering (eg. Schiminovich et al. 2001, Burgh et al. 2002).

Resonant scattering not only changes the direction of the photon following the scattering, but also its frequency, due to the velocity of the hydrogen atom it will scatter with. The frequency of the outgoing photon is related to that of the incoming photon by

$$\nu_{out} = \nu_{in} \frac{1 + (\mathbf{k}_{out} - \mathbf{k}_{in}) \cdot \mathbf{v}_X / c}{1 + (1 - \mu)(h\nu_{in}/m_X c^2)} \tag{3.20}$$

where $\mu = \mathbf{k}_{out} \cdot \mathbf{k}_{in}$. In this equation, the numerator is what determines the change of frame due to the coherent scattering in the frame of the hydrogen atom performing the scattering. A frame of reference is chosen such that only two velocity components are needed to describe the output velocity, as schematically represented in fig. 3.2, and each of these components is determined from a Gaussian distribution which depends on the incoming frequency of the photon. The directions are determined by phase functions, one for core scattering and one for wing scattering. Overall, this equation tells us the magnitude and the direction of the Doppler shift of the outgoing photon, depending on the incoming frequency of the photon, its incoming direction, its velocity toward the scatterer and the mass of the scatterer.

One more thing to note about RASCAS is its core skipping algorithm, which is incredibly useful to speed up the computations, which, on the galaxies used in this work, can take up to several hours on 32 CPU. This algorithm is needed since photons tend to be emitted in dense cells where they could scatter millions of times before being able to Doppler shift enough to
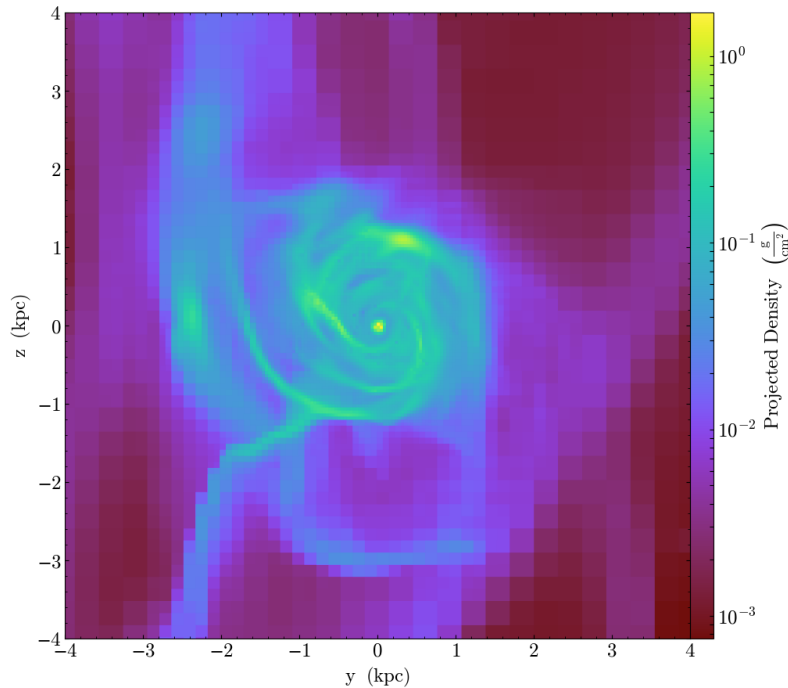
Figure 3.3: Gas density plot of the most massive galaxy in OBELISK at z = 6. This illustrates the resolution achieved in OBELISK.

be able to escape, and is therefore convenient to skip the scattering in the core of the line by placing the photon frequency on the wings. This algorithm biases the frequency shift and moves the frequency into the wing of the line directly, which is very useful in dense HI environments since it allows the photons to perform larger steps before the next interaction and therefore will lead to less interactions to compute.

3.2   Setup

To actually perform the radiative transfer of Lyman-α, the first step is retrieving the gas distribution of some galaxies of interest, which are extracted from the OBELISK simulation.

OBELISK is a high resolution ($\Delta x \simeq 35$ pc), radiation-hydrodynamics simulation of a subvolume of HORIZON-AGN (Trebitsch et al. 2021). OBELISK was run with RAMSES-RT (Rosdahl et al. 2013), which is a radiative transfer module of the adaptive mesh refinement code RAMSES (Teyssier 2002). RAMSES follows the evolution of dark matter, gas, stars and black holes, via gravity, hydrodynamics, radiative transfer and non-equilibrium thermo-chemistry, and the RT module deals with the propagation of radiation emitted by massive stars and accreting black holes through hydrogen and helium. OBELISK also includes a subgrid model for the evolution of dust, which is separate from the metals (Trebitsch et al. 2021). This feature will be used in the analysis later, where this model will also be compared to the other previously explained model, which ties the dust to the metal content of the gas.

The gas distribution in the most massive galaxy at redshift $z = 6$, which will be the redshift of interest in this work, is shown in fig. 3.3, to illustrate the resolution achieved in the simulation.

RAMSES-RT is not designed for resonant scattering, as in those cases only Monte Carlo schemes are feasible (Rosdahl et al. 2013), so the radiative transfer of Lyman-α is performed in post processing with RASCAS (Michel-Dansac et al. 2020).

Here I would like to detail the actual process of runnning RASCAS. The simulation box

is quite large, with sides of $L_{box} = 20h^{-1}$cMpc for the high resolution region, and performing the radiative transfer through all of it would be out of the scope of this work and extremely time consuming, so the first step to take is the creation of a domain where the radiative transfer will be performed. This is done with the pre-processing code `CreateDomDump`, which can manage the domain decomposition, adaptive mesh indexing and extract physical data from simulation outputs (Michel-Dansac et al. 2020). This is done through the use of three classes, `domain`, which defines the geometric properties of the domain, `gas_composition`, which converts simulation outputs into useful quantities for radiative transfer and `mesh` which handles cells and their indices (Michel-Dansac et al. 2020). Two types of domain are created with `CreateDomDump`, a computational domain, which delimits the volume in which the radiative transfer will happen, and data domains, which cover the computational domain and contain the physical information needed for the radiative transfer (Michel-Dansac et al. 2020). These domains can be defined for each object of interest through the `params_CDD.cfg` configuration file. In this file it is possible to input the simulation from which the domain will be selected, the shape of the domain, always a sphere in this work, the center and radius of the domain. The center was always chosen as the coordinates of the objects of interest and the radius always as the virial radius of that object, so the radius of its dark matter halo. Then, it is possible to give the gas composition, which can be taken from the simulation or be overwritten to be any preferred model, and it is also possible to select the atom species which will perform the scattering, in this case it will be HI. Once this file has all the information desired, it can be run with the pre-processing code `CreateDomDump` to perform the domain decomposition.

The steps after this one are those of the Monte Carlo method, so first it is necessary to create the initial conditions of the photons that will be transferred through this domain. Given that the main point of interest is the radiative transfer of Lyman-α photons, this was done using the `LymanPhotonsFromGas` code, which creates two initial condition files, one for photons emitted following collisional excitation, and one for those emitted following recombination. Once again, this code has to be run with a configuration file, `params_LPFG.cfg`, which includes the size and location of the domain where this photons will be created and how many photon packets will be created. In this work, 10^5 photon packets were used for both components for each galaxy.

This process was also repeated with the code `PhotonsFromStars` to get the continuum radiation close to Lyman-α and the UV continuum radiation, which are both needed for the analysis, as will be shown later. Those photons were created in a very similar way but in this case also a wavelength range was needed to create the initial conditions. These ranges were selected as 1150 Å to 1200 Å for the continuum close to Lyman-α and 1480 Å to 1520 Å for the UV continuum and the spectral shape was selected to be the tabulated version of stellar continuum which describes best the continuum. Once again 10^5 photon packets were created in each wavelength range.

The last step is to perform the radiative transfer of the created photons through the domain. Each initial condition file was ran separately with the `rascas` code, which is the code that actually performs the radiative transfer. Once again this code has to be ran with its parameter file `params_rascas.cfg`, which requires the domain decomposition and initial condition files location, the same gas composition parameters used in `params_CDD.cfg`, together with the scatterer type, which is HI, and the dust model with its parameters. Once the radiative transfer has been completed, RASCAS will output a result file, which can be analyzed. The various results achieved with this method will be presented in chapter 4.

3.3   RASCAS tests

Computing the transfer of a resonant line through a gas distribution is too complicated and dependent on too many random variables to be be done analytically, but there are very few exceptions to this, where a situation can be idealized to be simple enough to allow for an analytical solution. These cases are static, uniform, gaseous spheres, slabs and cubes
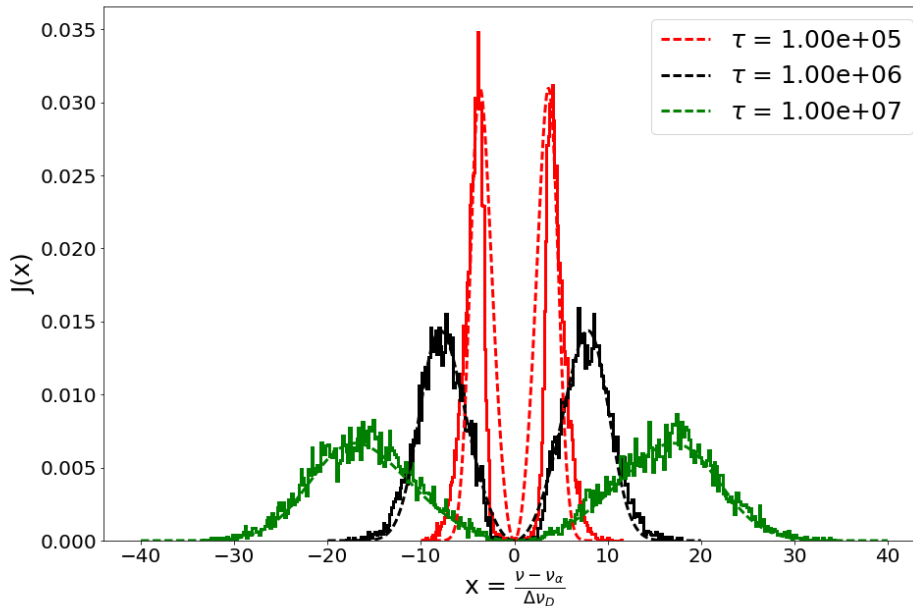
Figure 3.4: Comparison between the analytically derived spectra, the dashed lines, and the spectra modelled with RASCAS, the solid lines, for a static, homogeneous, gaseous sphere. The analytical spectra fits the modelled spectra well, especially at higher gas optical depths.

(Dijkstra et al. 2020). It is therefore possible to compare the results from RASCAS with one of these analytic solutions, to test and validate the radiative transfer code (Dijkstra et al. 2006, Orsi et al. 2012). Here, the static, homogeneous, gaseous sphere was chosen.

The analytical solution for a static, uniform gaseous sphere was derived by Dijkstra et al. 2006, following the previous derivations of Harrington 1974 and Neufeld 1990 and it is

$$J(x) = \frac{\sqrt{\pi}}{\sqrt{24}a\tau_0} \left\{ \frac{x^2}{1 + \cosh\left[\sqrt{2\pi^3/27}(|x^3|/a\tau_0)\right]} \right\} \tag{3.21}$$

for a gas temperature of $T = 10$ K. Here x is the dimensionless variable $x \equiv (\nu - \nu_\alpha)/\Delta\nu_D$, with ν_α being the frequency corresponding to Lyman-α and $\Delta\nu_D$ being the thermal broadening of the line, and τ_0 is the line center optical depth. This analytical solution is compared to the emergent spectra from RASCAS in fig. 3.4. Here, three different optical depths are tested, and in all cases the results from RASCAS fit the analytical solution well, although the deviation at $\tau = 10^5$ shows that the solution is only valid at $\tau > 10^6$.

It is also interesting to observe the shape that these profiles take and understand what affects them. The double peak shape was already explained in the previous chapter, and it is due to the the Doppler shift in frequency caused by the scattering, together with the higher optical depth at line center, due to the Voigt profile of the cross section with respect to frequency. The Doppler shift makes the photons drift towards the wings and the lower optical depth in the wings makes them stay there, as less collisions with neutral hydrogen will happen when a photon finds itself in the wings. Similarly, higher separations between the peaks at higher optical depths can be explained in the same way. The further in the wings a photon finds itself, the easier it will be to escape the gas, as it is increasingly unlikely to find an hydrogen atom with a velocity high enough to see the photon at resonance, which is an even more important effect when the optical depth of the gas is higher, due to the larger amount of atoms present in the volume. Lastly, the profile is completely symmetric,

which, once again is an expected results due to the nature of the test. Such a symmetric profile is only achievable with a static gas distribution, as if it was contracting of expanding, the profile would be expected top be shifted completely to one side of the Lyman-α line (Zheng et al. 2002) due to the consistent Doppler shift caused by the motion of the gas.

3.4   Creating synthetic observations

To be able to relate the results of the simulation to the real world it is useful to perform synthetic observations. Simulations allow for a study of the intrinsic properties of galaxies, but those are not what can observed, so it is necessary to find a way to get observable properties from simulations, which can be done by performing synthetic observations.
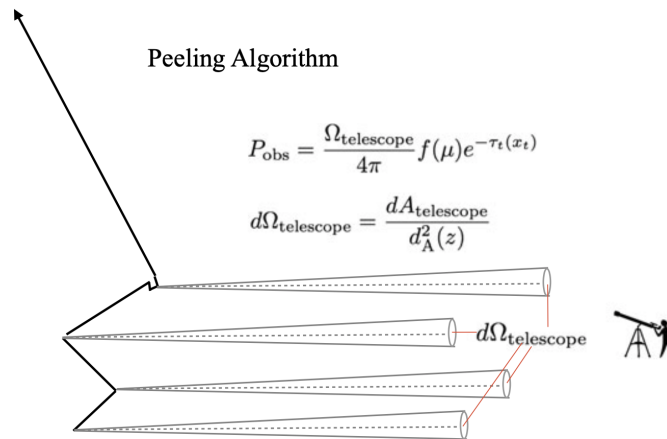

Figure 3.5: Schematic representation of the peeling algorithm, which is used to determine observables during a radiative transfer process. At each interaction the probability that a photon would go in the way of the observer is calculated. Credits: Dijkstra et al. 2020

In RASCAS, the synthetic observations of the Lyman-α emission are created using the so called "peeling-off" algorithm (eg. Yusef-Zadeh et al. 1984, Whitney 2011, Dijkstra et al. 2020). This is necessary because the probability that a Monte Carlo photon will escape and be observed by a synthetic telescope is negligible, since the telescope will only subtend a solid angle of

$$d\Omega_{\text{telescope}} = \frac{dA_{\text{telescope}}}{d_A^2(z)} \tag{3.22}$$

where $dA_{\text{telescope}}$ is the area of the mirror and $d_A(z)$ is the angular diameter at redshift z (Dijkstra et al. 2020). One way to go around this issue could be to increase the telescope area, effectively getting results which are averaged over multiple lines of sight, but Lyman-α observations are quite dependent on the viewing direction, as will be shown later, so this is not very accurate. Moreover, real galaxies are only observed from one line of sight, so if we want to be able to compare our results with observational results this method could not be used. Because of these reasons, the peeling-off algorithm is often used.

The peeling-off algorithm, which is schematically represented in fig. 3.5, calculates the probability that a photon would have gone in the direction of interest at each scattering, so each time a photon is emitted (Whitney 2011). This probability is the product of the fractions of photons reaching the point of scattering, the probability of scattering in the direction of the observer and the probability of escaping through dust toward the observer (Yusef-Zadeh et al. 1984). The probability of scattering toward the observer is given by using $\mu = \cos\alpha_{obs}$, where α_{obs} is the scattering angle toward the observer, in the phase function, represented by $f(\mu)$ in fig. 3.5 (Yusef-Zadeh et al. 1984), and the probability of the photon
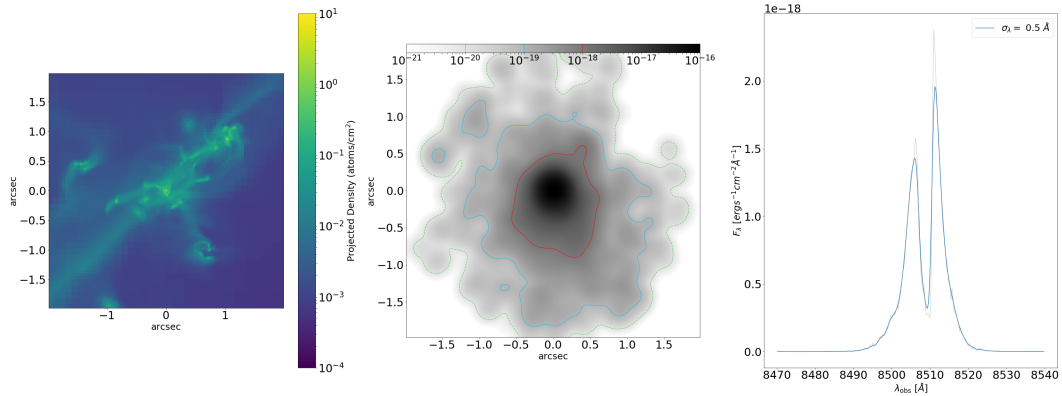
Figure 3.6: Surface brightness plot, gas density distribution and spectrum of the same line of sight of a galaxy. This is an example of the kind of synthetic observations that can be performed using the peeling-off algorithm together with RASCAS.

to be able to escape if $P_{esc} = e^{-\tau(x)}$ where x is the the frequency the photon would have had if it had last scattered in that direction (Dijkstra et al. 2020).

Each photon is then treated as a point source with luminosity L_α/N_{phot}, where L_α is the total luminosity of a source, and N_{phot} is the number of photons used in the Monte Carlo simulation to represent the source. The flux of each point source can be found as

$$S = \frac{L_\alpha}{4\pi d_L^2(z)N_{phot}} \times \frac{P(\mu)}{2} e^{-\tau(x)} \tag{3.23}$$

where $P(\mu)$ is the scattering phase function, and the factor 2 is a proportionality factor. The total intensity of photons reaching the observer from a given point in the sky is then calculated by summing the final weight of each photon reaching the observer over the total number of scatterings each photon has experienced and the total number of photons (Yusef-Zadeh et al. 1984).

Using this method it is possible to create surface brightness plots and spectra, resembling observations. For each galaxy, six lines of sight were used, to see how a difference in the angle of observation could affect the observable properties. One example of each output is shown for the same line of sight of a galaxy in fig. 3.6. Here I am also showing the gas distribution from the simulation, to show how the peeling-off algorithm converts a pure gas and dust distribution into a synthetic observation.

3.5   Analysis of synthetic observations

From the synthetic observation results and the radiative transfer results it is possible to calculate quantities like the intrinsic luminosity of the galaxy, its flux, the escape fraction of Lyman-α photons, the equivalent width and others.

Both the intrinsic luminosity of the galaxy, so the luminosity of the emitted photons and the "escaped" luminosity, so the luminosity of the escaped photons can be calculated. This is fairly easy to do as the necessary quantities are stored in RASCAS either in the initial condition or result files. For the intrinsic luminosity it is only necessary to know the frequency at which each photon packet is emitted, as the Monte Carlo photon actually represent a flux of photons, and the Planck constant in erg·s, which is 6.626196×10^{-27}erg·s, as together they give the energy of each photon. The number of real photons corresponding to a Monte Carlo photon is also needed, as it was already mentioned that Monte Carlo photons are really photon packets, as each of them represents a flux of many real life photons. This quantity is easily found as RASCAS stores the number of photon packets which were transferred and the total amount of "real" photons this would correspond to. Since RASCAS

deals with recombination and collision photons separately, this will just need to be done twice, with the respective "real" photon value. In short, the luminosity was found as

$$L_{tot} = L_{rec} + L_{col} = \sum_i \frac{N_{real,rec}}{N_{MC,rec}} h\nu_i + \sum_j \frac{N_{real,col}}{N_{MC,col}} h\nu_j \tag{3.24}$$

where N_{real} is the amount of real photons emitted from recombination (rec) and collisions (col), N_{MC} is the number of photons transferred with the Monte Carlo method and ν_i is the frequency of each photon.

The escaped luminosity is calculated in the same way, but only the photons that escape are taken into account. RASCAS stores photon status as 1 if they are escaped and 0 if they are absorbed, so to calculate the escaped luminosity I select the photons with status 1 and perform the same calculation as for the intrinsic luminosity. For this calculations I am not taking into account the direction of escape of the photons, as these are 3D quantities.

The flux per line of sight can be found by integrating the spectrum over all frequencies. I have chosen to calculate the flux at two different apertures, one encompassing everything up to the virial radius, which is the radius of the dark matter halo and the radius at which the synthetic observation was performed, and another one encompassing only 10% of the virial radius, which I defined as the galaxy radius and should be more in line with the kind of radii used in observations. From this line of sight dependent fluxes I also recalculated the line of sight dependent luminosity, as is done in observations, using

$$L = F \times (4\pi d_L^2) \tag{3.25}$$

We can also compute the escape fraction of Lyman-α photons, $f_{esc}(Ly\alpha)$, which can be done for the whole galaxy, so 3D averaged, or per line of sight. The 3D escape fraction can be easily calculated by dividing the escaped luminosity by the intrinsic luminosity. For the line of sight escape fraction I have used the flux calculated by integrating the spectra and the "intrinsic" flux, which is the intrinsic luminosity at that radius converted to flux. This quantity is not an observable quantity, but is useful to determine the escape fraction. Of course the opposite could have also been done, converting the flux calculated with the integration of the spectrum into a luminosity, but the result is unaffected. For the virial radius escape fraction, I used the intrinsic luminosity found previously, whereas for the galaxy radius escape fraction I had to calculate again the intrinsic luminosity, but this time only for the photons whose last scatter or absorption is located in a radius of 10% the virial radius from the center in the direction of observation, making the selected photons effectively reside in a cylinder. This was done by following eq. (3.24) but only with the photons whose last position (the position of absorption or last scattering) is in the chosen cylinder.

At this point, we can add the continuum from the stars in the wavelength range 1150 Å to 1200 Å, which is close enough to Lyman-α to be used as an approximation of the continuum around Lyman-α without worrying about the resonant scattering adding time to the radiative transfer, which makes the radiative trasfer of these photons very fast. Synthetic observations were performed also on the continuum as the continuum flux is necessary to calculate the Lyman-α equivalent width (EW) per line of sight.

Equivalent width is a very useful quantity to determine the strength of a line, in this case Lyman-α, with respect to the continuum and it is, in theory, found by equating the area of the curve to that of a rectangle of height of the continuum and width of the equivalent width. I have found both a 3D averaged EW and the line of sight dependent values. For the 3D averaged I started from the escaped luminosity previously calculated and divided that by the luminosity of the continuum per unit wavelength. Effectively, I just used

$$EW \equiv \frac{L_{Ly\alpha}}{L_{\lambda,\text{cont}}} \tag{3.26}$$

where $L_{\lambda,\text{cont}}$ is the flux density in erg/s/Å, which gives the rest frame equivalent width of Lyman-α (Dijkstra et al. 2010). For the line of sight equivalent width, both for the virial

and galaxy radius, I have instead divided the total flux by the mean value of the continuum, as shown here

$$EW = \frac{F}{\bar{F}_\lambda \times \frac{1}{z+1}} \tag{3.27}$$

where the $\frac{1}{z+1}$ factor is needed to account for the redshift.

Finally, I also computed the line of sight UV absolute magnitude. The 3D-integrated value for each galaxy can be taken directly from the OBELISK catalogue, but the line of sight value had to be calculated by once again performing the radiative transfer of photons in the selected range, which is this case is 1480 Å to 1520 Å. The absolute magnitude was calculated in the AB magnitude system as

$$m_{AB} = -2.5 \log_{10} f_\nu - 48.60 \tag{3.28}$$

with f_ν being the spectral flux density, which is the flux per unit wavelength, in $\mathrm{erg/s/cm^2/Hz}$. The absolute magnitude is then calculated with the distance modulus

$$M = m - 5 \log_{10}(d) + 5 \tag{3.29}$$

where d is the distance in parsec.

Another value will be used in the analysis, which is the ionizing radiation escape fraction $f_{esc}(LyC)$, which was calculated using the same method as the Lyman-α escape fraction, by Dr. Valentin Mauerhofer.

Chapter 4

Results

I now apply the code described in the previous chapter to the analysis of a sample of 16 galaxies taken from the OBELISK simulation. For all the galaxies, I performed 3D radiative transfer and extracted projected quantities over six lines of sight using the synthetic observation module described in section 3.4. The intrinsic properties of the galaxies were taken directly from the OBELISK simulation. I perform the radiative transfer twice for each galaxy, in order to compare the different dust models described in section 3.1. Here I will first present the most relevant results for only one model, the one from Laursen 2010, which ties the dust to the metals and later I will show how the models compare and the most significant differences between the two models.

RASCAS/Synthetic observations results

The sample of galaxies is composed of three different sub-samples for which different selection methods were used. The first galaxy selected, sample A, is a massive galaxy, with a mass of $3.9 \cdot 10^{10} M_\odot$ and a halo mass of $4 \cdot 10^{11} M_\odot$, which shares some properties with some of the brightest LAEs observed at $z > 6$, such as Himiko (Ouchi et al. 2013), with which it shares very high star formation rate, $105 M_\odot$/yr for this galaxy and about $100 M_\odot$/yr for Himiko. This galaxy is however much more dusty than Himiko. Afterwards, we looked at two galaxies, sample B, which have a high 3D averaged Lyman continuum escape fraction ($f_{esc}(LyC) = 19.8\%$ and 5.7%) and are relatively bright ($M_{UV} = -19.7$ and -19.6 after dust extinction), which would make them observable LyC leakers at $z = 6$. Finally, we selected all the galaxies in the simulation in a an observed UV absolute magnitude range of $-19 < M_{UV} < -19.5$, sample C, to get an analogue of an unbiased sample of relatively faint Lyman Break Galaxies with UV magnitudes typical of LAEs. In the figures of this chapter, the different galaxy samples are indicated with different marker shapes. Sample A will be represented by circles ($\bullet$), sample B will be represented by stars ($\bigstar$) and sample C will be represented by the three pointed shape ($\curlyvee$).

4.1 Results

Using RASCAS together with the peeling-off algorithm I have to calculated and studied many quantities, mostly observational quantities, but also other like the the escape fraction and the intrinsic luminosity which then also gives the possibility to compare observational quantities to intrinsic ones. In this section I will present the most relevant results from the standard dust model in RASCAS.

Sample	ID	M_* [$M_\odot$]	SFR [$M_\odot$/yr]	M_{UV}^{obs}	M_{UV}^{intr}	$f_{esc}(LyC)$	$M_{\rm dust}$ [$M_\odot$]
A ●	14505	$3.8 \cdot 10^{10}$	105.5	-21.0	-24.0	0.013	$1.8 \cdot 10^7$
B ★	65038	$1.1 \cdot 10^9$	7.4	-19.7	-20.8	0.198	$2.2 \cdot 10^6$
	64846	$1.0 \cdot 10^9$	7.8	-19.5	-21.6	0.057	$4.2 \cdot 10^6$
C ⅄	2899	$1.4 \cdot 10^{10}$	31.0	-19.4	-21.5	0.001	$1.1 \cdot 10^7$
	24688	$6.4 \cdot 10^9$	35.7	-19.4	-23.4	0.004	$8.7 \cdot 10^6$
	55468	$4.9 \cdot 10^9$	17.9	-19.0	-21.9	0.002	$9.8 \cdot 10^6$
	36112	$3.7 \cdot 10^9$	22.8	-19.4	-22.3	0.007	$1.4 \cdot 10^7$
	41663	$3.2 \cdot 10^9$	8.4	-19.0	-21.9	0.007	$5.5 \cdot 10^6$
	3639	$2.6 \cdot 10^9$	18.1	-19.1	-21.8	0.001	$5.9 \cdot 10^6$
	42665	$1.7 \cdot 10^9$	10.0	-19.2	-21.5	0.023	$5.8 \cdot 10^6$
	8776	$1.6 \cdot 10^9$	6.2	-19.0	-20.9	0.026	$8.3 \cdot 10^6$
	39021	$1.5 \cdot 10^9$	9.5	-19.0	-21.1	0.033	$8.0 \cdot 10^6$
	76168	$1.5 \cdot 10^9$	8.0	-19.2	-21.6	0.011	$3.1 \cdot 10^6$
	10345	$2.5 \cdot 10^8$	1.5	-19.1	-20.0	0.235	$1.5 \cdot 10^6$
	57172	$2.4 \cdot 10^8$	1.5	-19.3	-19.8	0.485	$1.2 \cdot 10^6$
	67244	$7.0 \cdot 10^7$	0.7	-19.0	-19.4	0.195	$2.1 \cdot 10^5$

Table 4.1: Characteristics of the galaxies of the sample. M_* represents the stellar mass, SFR stands for star formation rate, calculated over 10 Myr, M_{UV}^{obs} is the observed absolute magnitude, M_{UV}^{intr} is the intrinsic absolute magnitude, $f_{esc}(LyC)$ is the Lyman Continuum escape fraction and $M_{\rm dust}$ is the dust mass.

4.1.1 Photon Production and Escape

I first studied the gas and dust conditions in which the photons that escape are created and how those conditions differ from the those of absorbed photons. I compare these in fig. 4.1. The top figure shows the initial dust and gas conditions for the escaped photons, and the bottom figure shows these conditions for the absorbed photons. From these plots we can see that photons which are able to escape the galaxy are generally created in less dense environment, both in dust and in neutral hydrogen, whereas absorbed photons are never created in these conditions. Especially there are no photons created in the tail of very low dust density at constant gas density seen in the escaped photons distribution. This feature is quite telling, as it shows that most of the absorption seems to be done locally, right where photons are created.

In fig. 4.2 I am showing the 3D averaged luminosity profile, which is the luminosity profile that would be observed if averaged over all lines of sight, of the escaped photons (solid lines) compared from the luminosity profile of the photons at their initial conditions (dashed lines) from galaxy ID 64846. The figure clearly shows that most of the luminosity comes from the photons created by recombination, as their contribution to the total luminosity, at any distance from the center, up to virial radius, is about two orders of magnitude higher for the escaped photons and about one order of magnitude higher for the initial condition photons. It also shows that the center is the brightest part of the galaxy. Here I am only showing the profile of a single galaxy but this behaviour appears consistently in all the galaxies studied, even though sometimes the difference between the two components decreases to about one order of magnitude also for the escaped photons. This is completely expected, as the central part of the galaxy is the place where star formation happens, which means that there are HII regions where Lyman-α can be produced through recombination, and is generally the densest part, which means that there will be more gas, also neutral, to explain the high collisions emission. Out of the center there is a smooth decline to larger radii, as the gas starts to rarefy.

We can now compare the difference between the created photons, whose profile is shown dashed, and the escaped photons, which are represented by the solid lines. The distance from the center, for the escaped photons, was calculated based on the location of their last scattering, so this plot is telling us two main things. First of all, we can see that within
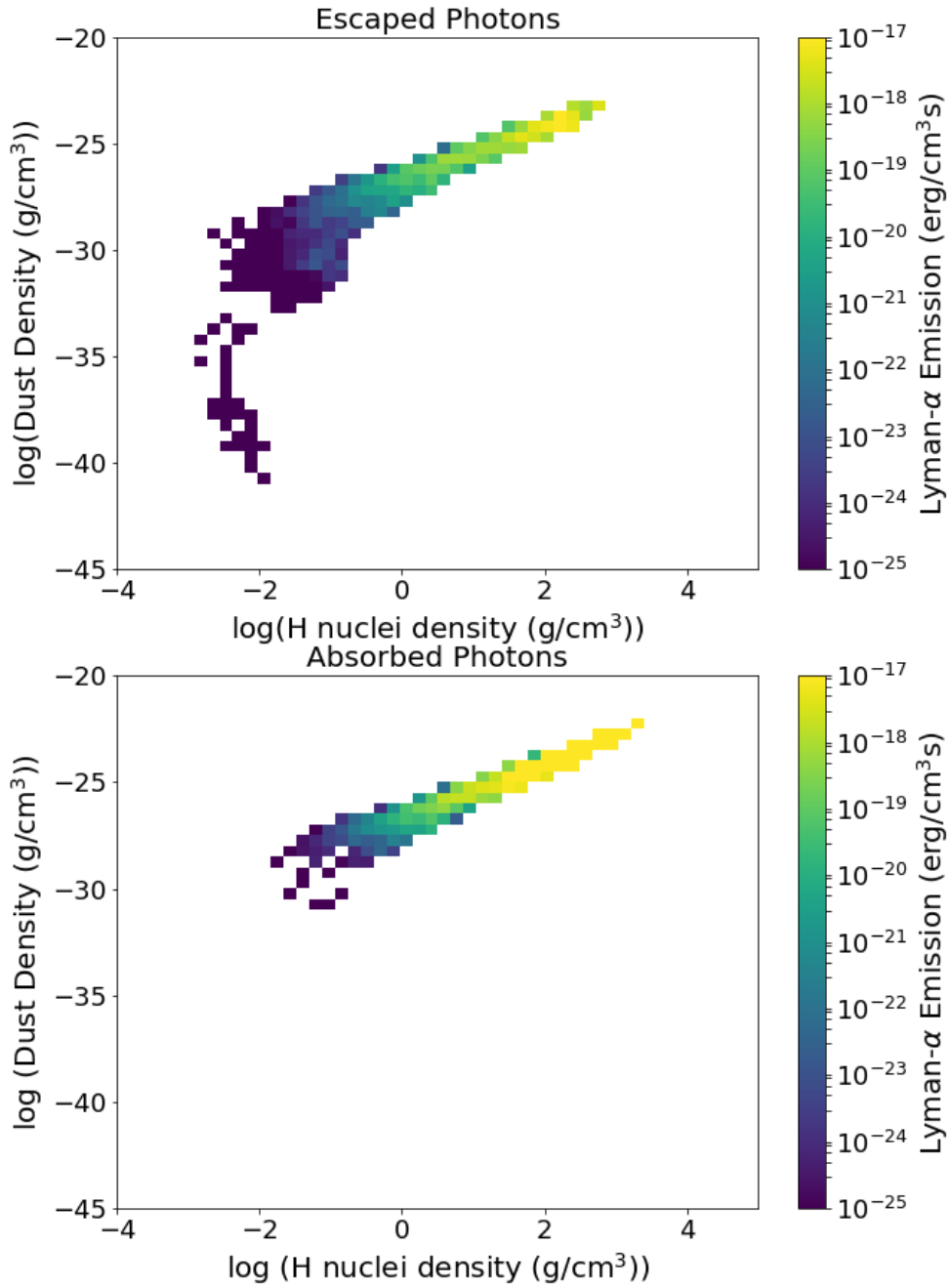
Figure 4.1: Comparison of gas conditions at the locations where photons that escape the galaxy and that are absorbed are created. In general, the absorbed photons are created in denser environments, hinting that absorption is mostly done locally.
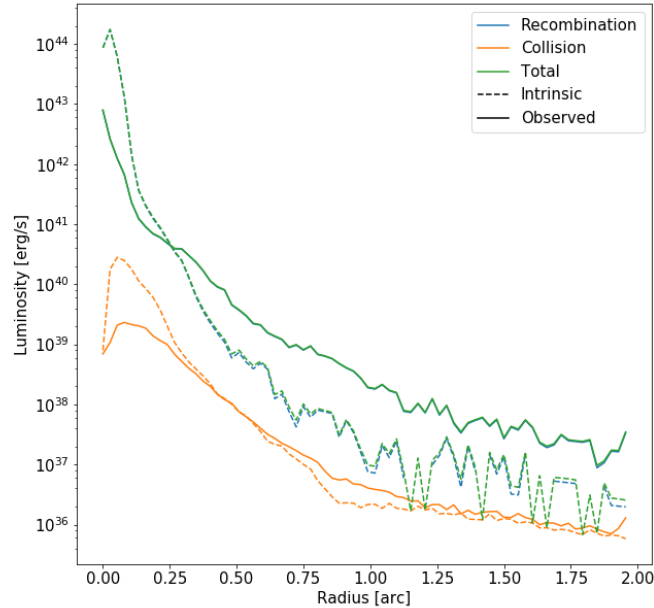
Figure 4.2: Observed (solid line) and intrinsic (dashed line) luminosity profile of a single galaxy (ID 64846). The center of the galaxy is at 0 and the radius increases until the virial radius. The center is the brightest, but with high absorption and recombination is always brighter than collisions, also on the outskirts of the galaxy.

the inner 10% of the virial radius the luminosity of the photons escaped is substantially lower than that of the initial condition photons for both components. This is likely due to two reasons, being the fact that the center of the halo is where the galaxy resides, so here there will be more dust to absorb the photons, and that the photons created here might have scattered and have been emitted somewhere else. The second main feature I would like to discuss in this figure is the fact that after this initial radius percentage, the emission of collision photons follows the creation of collisions photons almost perfectly, whereas it seems like there are more recombination being emitted than created. This peculiar behavior of the recombination photons is probably due to the fact that most recombination photons are created in the central part of the galaxy, where there is star formation, and then scatter around the galaxy, with their last scattering surface being farther away from the center than the location of their creation. It would seem like this is less the case for collision photons, even though we can spot an increased emission around 1 arcsec from the center. The behaviour we see here, of the last scattering location possibly being far away from the creation location, is due to the resonant nature of Lyman-α and it is one of the reasons why this line is so challenging to interpret.

In fig. 4.3 we can again see the difference between the photon creation locations and their escape location. In this figure I am showing, for both recombination and collisions, the photon luminosity at emission, overlapped by the three isophote curves taken from the synthetic observations of the same galaxy, as previously shown in fig. 3.6. First of all, we can see that the recombination is the brightest component to the overall luminosity of the galaxy. Then, another interesting characteristic of these figures is that we see that the recombination photons are mostly created in the center, but they can last scatter on the outskirts of the galaxy, leading to photons escaping the galaxy at radii where no photons are created. This does not happen for collision photons, which seem to escape close to where
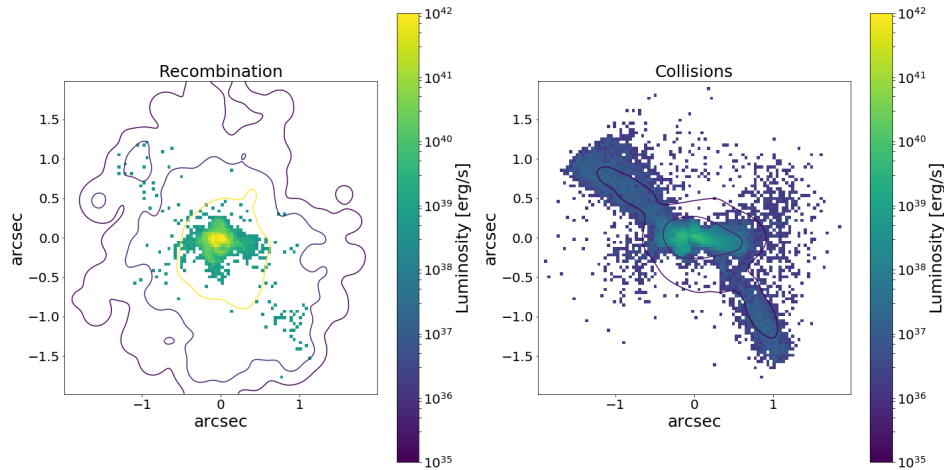
Figure 4.3: Equal surface brightness contours on intrinsic luminosity distribution for galaxy ID 64846. Recombination photons appear to scatter further before being able to escape, leading to a much more spread out surface brightness distribution than intrinsic luminosity distribution than in the case of collisions photons.

they are created.

Lastly, in fig. 4.4 I am showing a comparison of the escape fraction and surface brightness for the same galaxy (ID 64846). The escape fraction was calculated as the fraction of photons created at a given location that are able to escape the galaxy, so this panel tells us that most of the photons created in the center are unable to escape, whereas those created in the outskirts have an (almost) 100% chance to escape the galaxy. Of course this is due to the center being much dustier than the outskirts. The surface brightness plot instead is made taking into account only the last scattering position of the photons, but without their direction. This figure shows that the center of the galaxy is the brightest part of the galaxy, which is not surprising, as this is the place where most star formation and therefore recombination happens. What is slightly surprising is that when taking these plots together, we seen an almost exact overlap between the region of almost, but not quite, null escape fraction and the brightest region. This must mean that even though many photons created in the center are absorbed by dust, this part of the galaxy is so intrinsically bright in Lyman-α that more photons escape this part than the outskirts. This was partially already seen in fig. 4.2, where we can see the center of the galaxy being intrinsically an order of magnitude brighter than it looks like at escape, due to both the absorption of the photons and the scattering to higher radii.

4.1.2 Lyman-α Spectrum

Using the peeling off algorithm, synthetic observations of spectra were done, for each galaxy in six lines of sight per galaxy, as the peeling-off method results in a spectral datacube with coordinates (x, y, λ) in each direction.

It is interesting to see how the spectra of a single galaxy varies along the various lines of sight, due to the resonant nature of Lyman-α, which is what I am showing in fig. 4.5. In this figure I am showing the profile found with the synthetic observation, in blue, which includes all the photons emitted up to virial radius, and the profile including only the inner 10% of the virial radius, which is used to approximate the galaxy, and would be more similar to observations, in orange. Given the fact that the galaxy is observed at $z = 6$, the actual observed profile would have a reduced blue peak (Laursen et al. 2011), but not quite 0, due to only part of the IGM still being neutral, as $z = 6$ is still in the Epoch of Reionization, but at the end. Indeed, in fig. 4.5 we see that the Lyman-α profile varies strongly with the
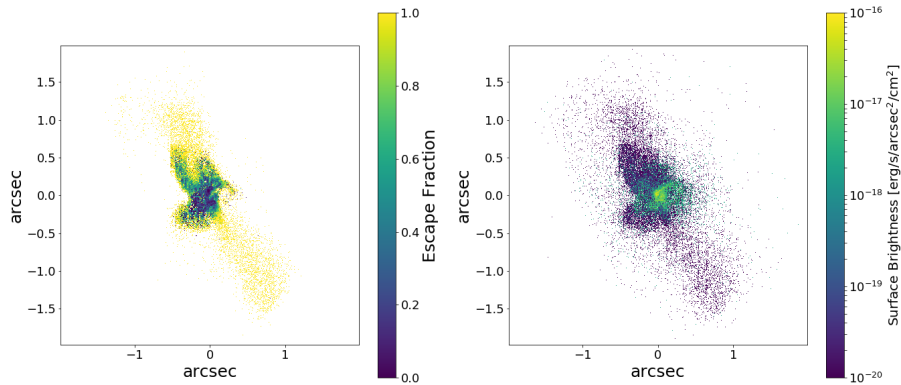
Figure 4.4: Escape fraction distribution compared to surface brightness distribution of galaxy ID 64846. The center of the galaxy is the brightest and the but also the place with the least escape fraction.

direction of observation, which is an important factor to take into account when interpreting the individual Lyman-α spectra, as here we see that the same gas distribution can lead to vastly different profiles, so it would very challenging to determine the gas distribution from the profiles alone.

One very surprising feature of these spectra, and of many of the other spectra analysed is the strong blue peak, as even at lower redshifts, where the IGM does not absorb any of the blue peak, observations show that the red peak is much stronger than the blue peak (eg. Verhamme et al. 2016, Leclercq et al. 2017, Izotov et al. 2018, Orlitová et al. 2018). The strength of the blue peak compared to the red peak here indicates much stronger inflow than outflow. This could have a physical reason and be a sign of cold inflows, which are thought to be important at high redshifts, $z > 2$, for the growth of galaxies (eg. Dekel et al. 2006, Ocvirk et al. 2008, Kereš et al. 2009), or could be a numerical artifact due to too weak outflows (Mitchell et al. 2021). I have not investigated in detail the origin of this inflowing kinematic, as the main focus of the project was the connection Lyman-α properties with intrinsic galaxy properties and with the Lyman continuum, and not a detailed study of the circum galactic medium.

From the spectra I found the separation between the peaks, as it is a common quantity in Lyman-α studies and it can be used to estimate the ionizing radiation escape fraction (eg. Verhamme et al. 2015) which can also be compared to the values from the simulation. This is easily done using the `find_peaks` function of `scipy.signal`. Using the same function it is also possible to determine the minima of the spectra. The same spectra seen in fig. 4.5 with the results from the `find_peaks` routine are shown in fig. 4.6. The peak separation is then given by the distance in km/s between the two identified peaks.

In some cases more than two peaks or only one peak is identified, which makes the analysis more challenging. An example of a single identified peak is on the bottom right of fig. 4.6, which is quite a rare case, as it only happened in 3% of cases. In this case I set the peak separation to 0, as there is no clear second peak. The case where more than two peaks were identified is more complex to deal with. An example is the spectra on the bottom left, where two peaks next to each other are identified, on the blue side of Lyman-α, but this is still an easy case to deal with, since the difference between choosing one peak or the other in terms of peak separation is minimal. Other cases are much more chaotic, and determining the actual peaks from the output of `find_peaks` is a lot less robust, and therefore I chose not to include these data points in my analysis. An example of this is fig. 4.7, where in the spectrum at virial radius we can see four peaks being identified by the
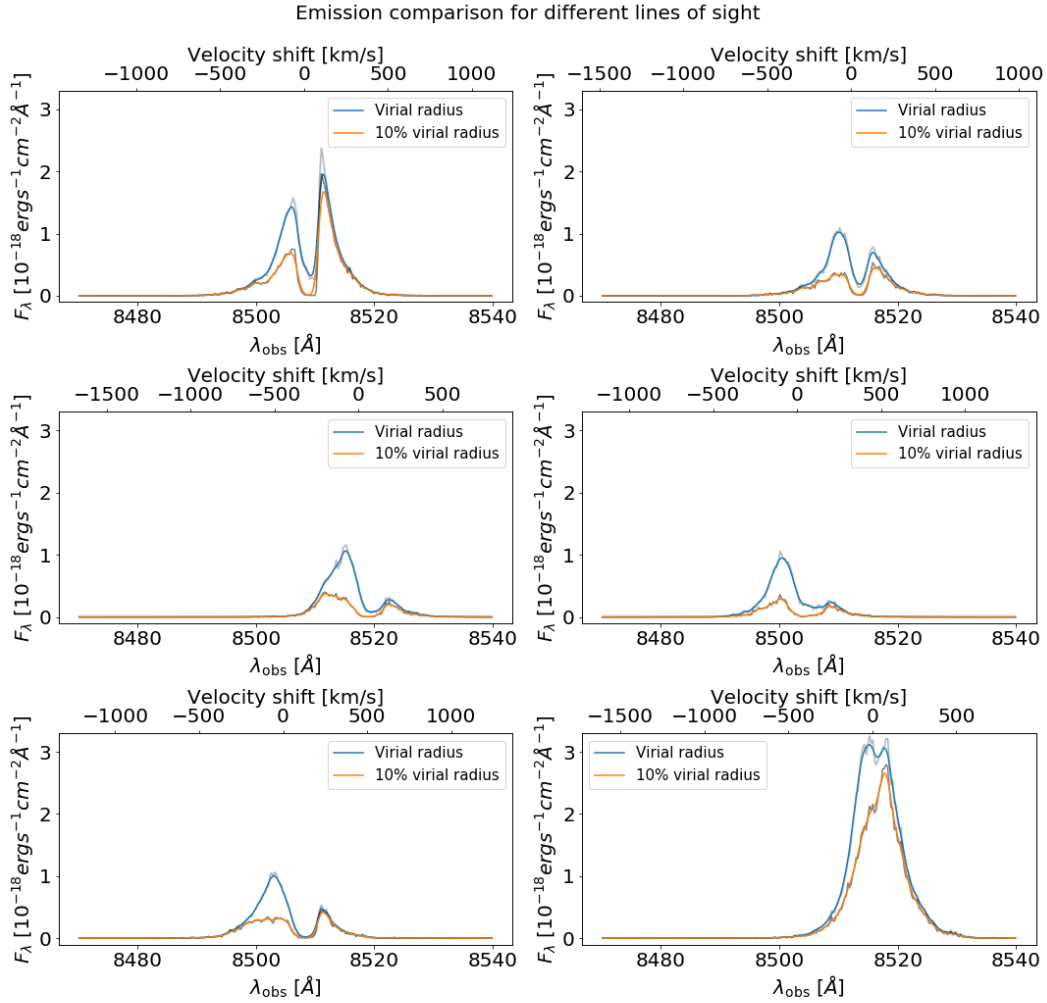
Figure 4.5: Spectra for six lines of sight of the same galaxy. For each plot in blue is the spectrum obtained when taking a domain as large as the virial radius and in orange is the profile obtained when only using the inner 10% of that profile, which is used to approximate the galaxy itself. A wide variety of spectral shapes can be seen, even though these are observations of the same galaxy, from different viewing angles.
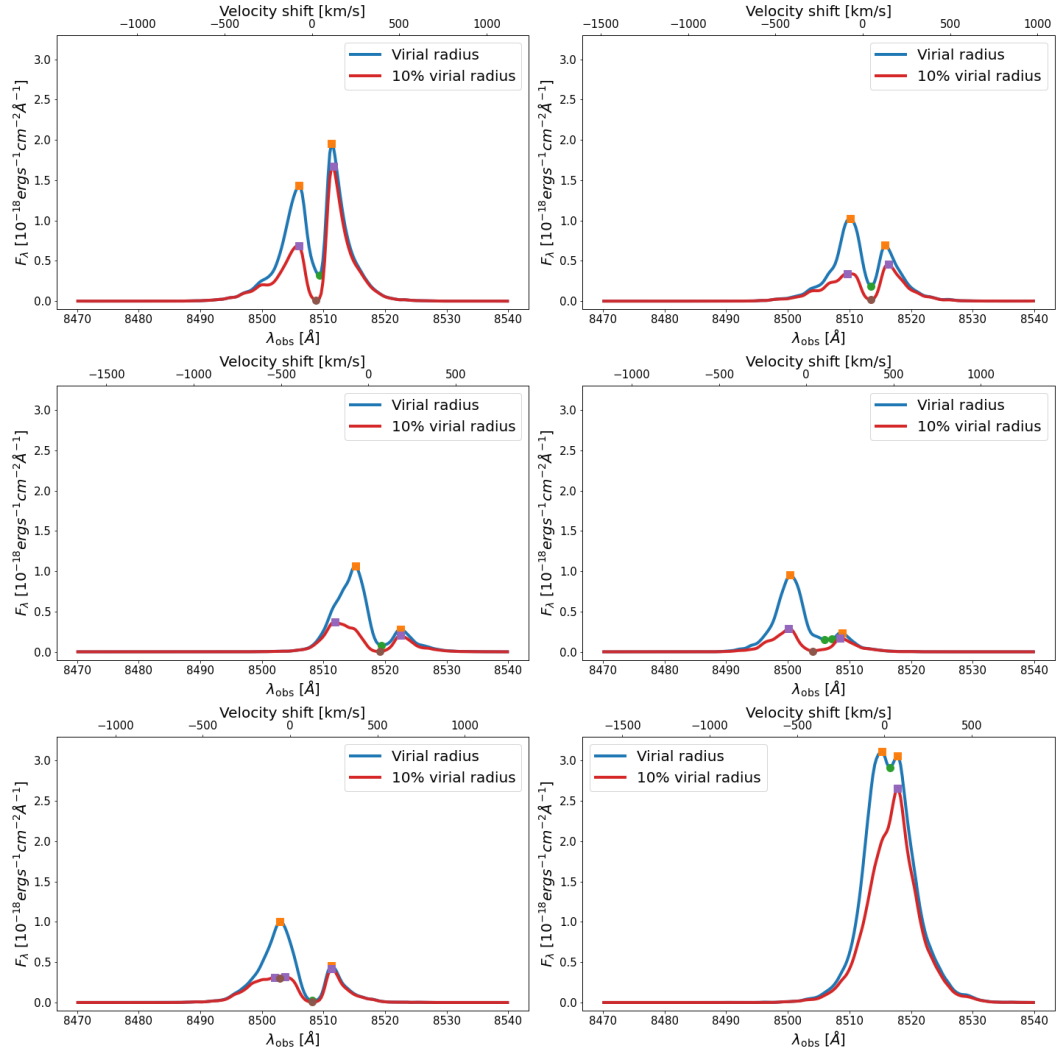
Figure 4.6: Spectra from the same galaxy together with the identified peaks and minima. The peaks are shown with the square points and the minima with the circle points. Once again the inner 10% of the virial radius is used to approximate the emission from the galaxy itself.
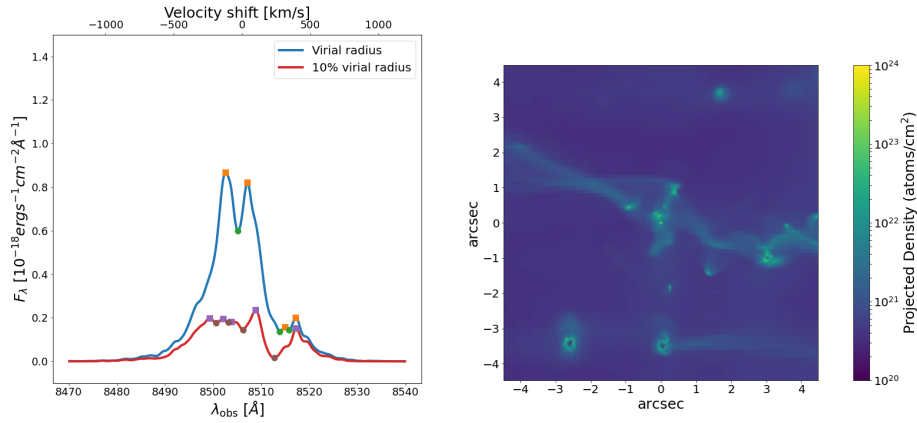
Figure 4.7: Spectra of galaxy ID 2899, together with the gas distribution of the same galaxy. From this spectrum is impossible to identify two clear peaks, possibly due to the peculiar gas distribution of the galaxy, which looks like it could have satellites or it might be undergoing a merger.

`find_peaks` routine, and even more at the galaxy radius. Here there is no clear solution for the peaks, so in this and similar cases I chose not to select any and remove these points when peak separation is included in the analysis. A possibility to test the robustness of the peak finding and possibly include the spectra that I have decided to exclude could be to repeat the peak finding on an increasingly smoothed spectra but I chose not to perform this step, as it was not the focus of the project. In some cases the multiple identified peaks are probably artifacts of `find_peaks`, as I think is the case on the bottom left spectrum of fig. 4.6 I mentioned earlier, where the two peaks are almost in the same location. However, in most cases I would think they are due to a peculiar gas distribution in the galaxy being observed, which is likely the case for the spectrum shown in fig. 4.7, where it seems that there are actually three main peaks instead of two, and this behavior is present in almost all lines of sights of this galaxy. This is a peculiar characteristic of this galaxy, so it is interesting to observe is in the simulation to attempt to determine if there is a visible origin to this. The gas distribution of this galaxy is shown in fig. 4.7 and from this I would say that the possible source of this third peak could be the blobs which look like satellites, or possibly a merger, and the large amount of diffuse gas running horizontally through the figure. It is possible that the emission from the diffuse gas will not be scattered much, leading to a third, more central peak.

Starting from the spectra I have also tried to determine the kinematics of the galaxy, but I was unable to, confirming again that the Lyman-α line is a poor tracer of the overall kinematic due to the added complexity of the resonant scatterings. An example of a velocity map is fig. 4.8. This kind of plot was created starting from the data cube and taking small sections of 4x4 pixels in the image and determining the spectra of those sections, smoothed to the same resolution as the other spectra. From each segmented spectrum I then determine the maximum and the velocity shift between that maxima and Lyman-α, which is what is shown in fig. 4.8. These sections are often single peaked, as in such a small section of the galaxy, Lyman-α radiation will likely encounter gas moving prevalently in one direction.

4.1.3   Properties of Lyman-α line

From the spectrum I explored the dependency of the quantities calculated in chapter 3 with other galaxy properties.

In fig. 4.9 I am showing the Lyman-α equivalent width against the Lyman-α escape fraction for all the lines of sight for all the galaxies, but only for the values at virial radius. This aperture was chosen for this and all the subsequent plots for consistency and because it
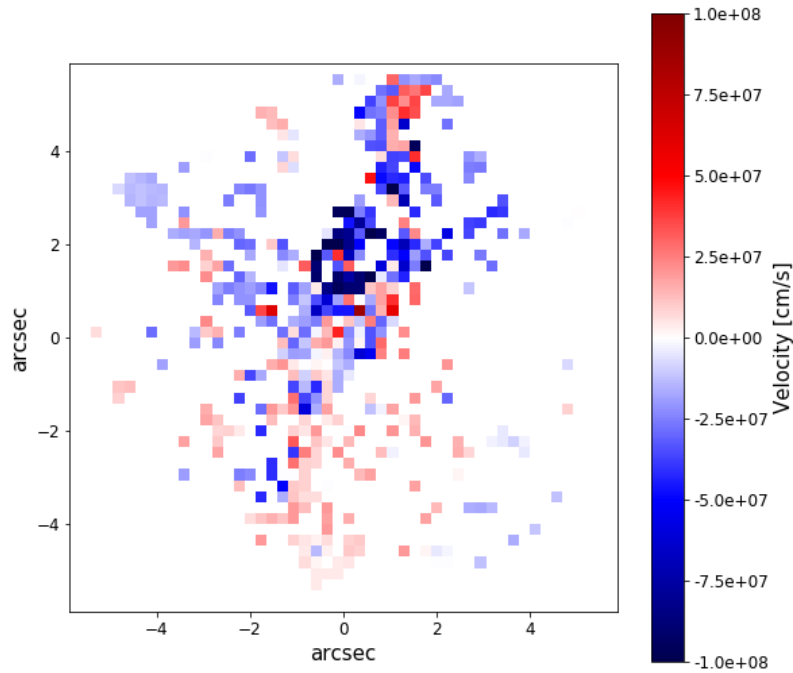
Figure 4.8: Velocity plot of massive galaxy. It is impossible to determine and real kinematics from this plot, due to the resonant nature of Lyman-α.

is the aperture at which the synthetic observations were performed, and it encompasses all of the gas belonging to the galaxy, which should give more complete results. Leclercq et al. 2017 have shown that high redshift galaxies are surrounded by Lyman-α halos, and therefore including all the gas up to the virial radius seems beneficial. One thing to be aware of, is that the inclusion of all of the gas in the halo will trace larger scale kinematics, which is not necessarily a point of interest of the project. However, this is also the case when observing a completely unresolved source, which is always the case for LAEs at high redshift, as the PSF of the MUSE instrument without adaptive optics is about 0.6" to 1", depending on seeing, which would encompass at least part of the halo for all of my galaxies.

In all of the figures presented in this section, the different marker shapes represent different methods of galaxy selection. Sample A will be represented by circles (●), sample B will be represented by stars (★) and sample C will be represented by the three pointed shape (⅄). The data in the figure is color coded using a variety of properties. These properties are the Lyman-α luminosity, the intrinsic Lyman-α luminosity, the ionizing radiation escape fraction, the instantaneous star formation rate, the specific star formation rate, the intrinsic UV magnitude, the observed absolute UV magnitude and the mass.

A few weak trends between the galaxy properties can be identified in fig. 4.9. First we see that at all values of escape fraction there is a variety of possible equivalent width value, which means that the intensity of the Lyman-α line with respect to the continuum seems to not be tightly correlated to the amount of Lyman-α photons that escape the galaxy. This is because the Lyman-α photons and the continuum photons are produced in different places, respectively gas and stars, and because a Lyman-α photon will encounter different amounts of dust than a continuum photon from the same line of sight, due to scattering. This is unlike the results of Sobral et al. 2019 who have found a linear relation between $f_{esc}(Ly\alpha)$ and the equivalent width, although the study was done at low redshift, and their target was selected differently, as the CALYMHA survey targets H-α emitters. My data seems
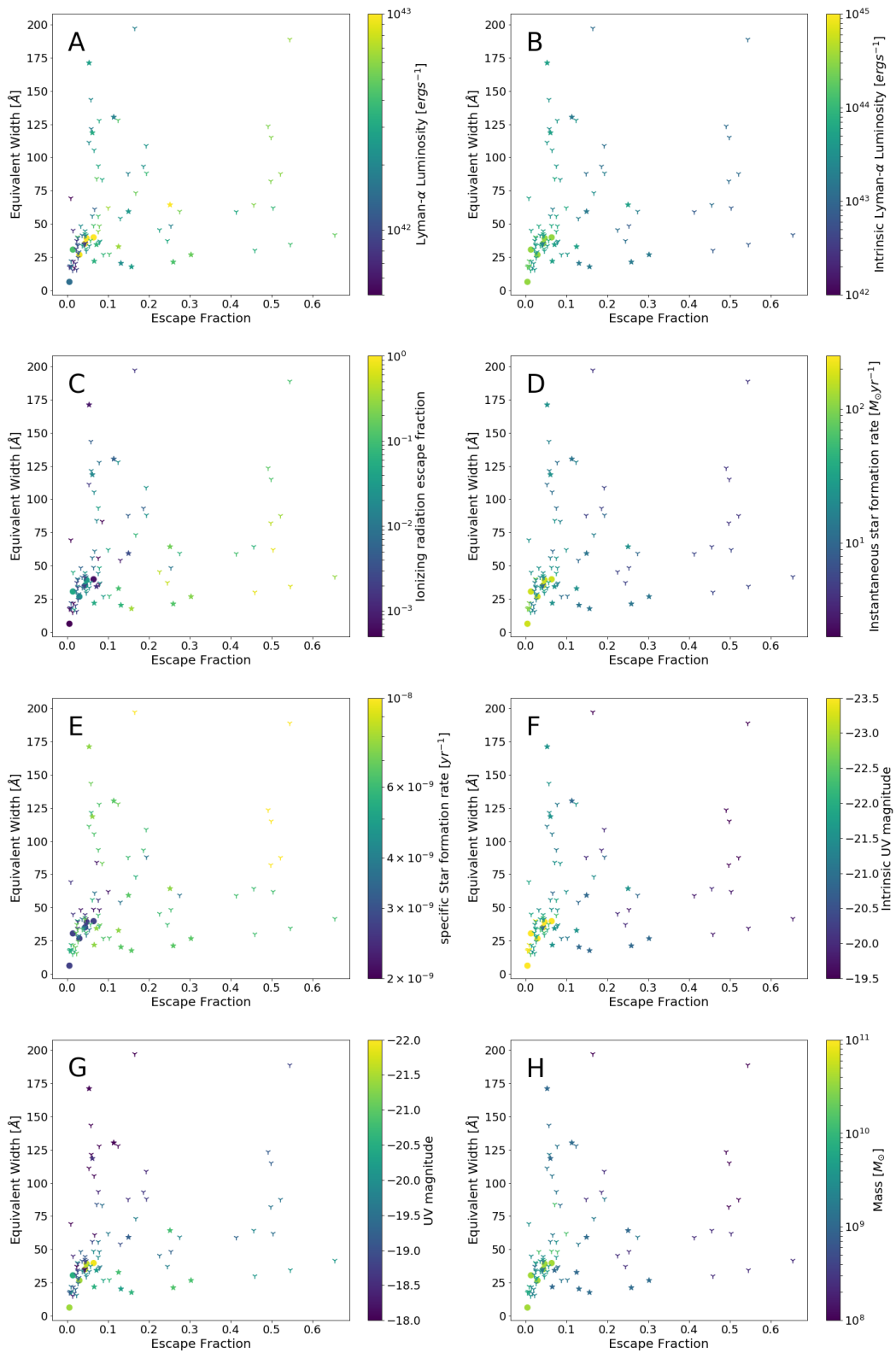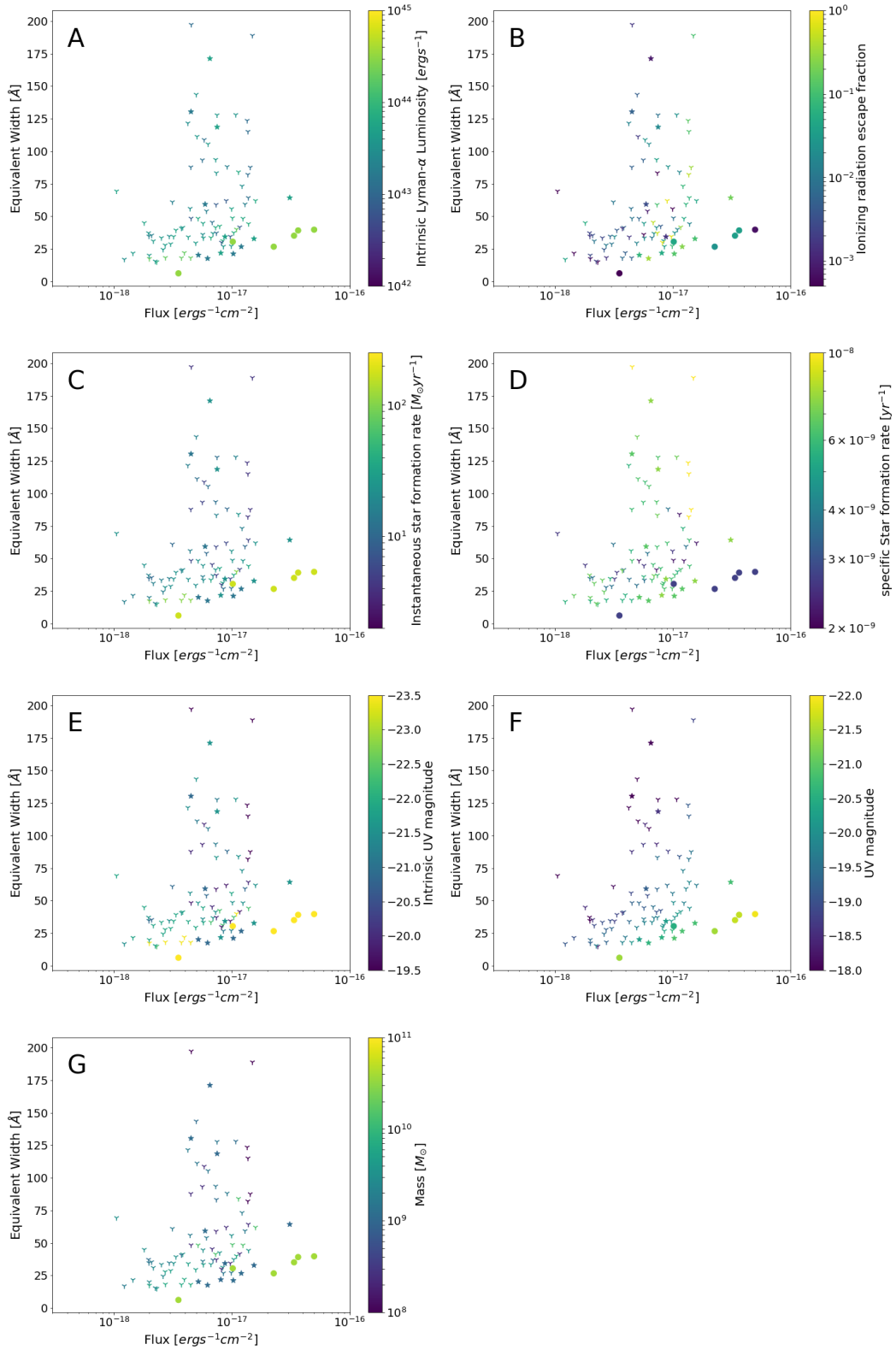
Figure 4.9: Lyman-α equivalent width against Lyman-α escape fraction, each plot color coded by a different quantity. The different markers represent the different galaxy selection methods, with the circles being the lines of sight of the massive galaxy, the stars being the Lyman continuum leaker candidates and the three pointed shape being the rest.

to agree with theirs only at low escape fraction and low equivalent width, but at higher escape fraction or equivalent width I see a much higher spread in the data. In panel A of fig. 4.9 we can see a weak trend of higher Lyman-α escape fraction at higher Lyman-α luminosity, with fixed equivalent width. This behavior can be understood as a higher escape fraction is linked to less dust, and therefore more continuum emission, so while the Lyman-α luminosity increases, so does the continuum luminosity, leading the equivalent width to not change significantly. Just below, in panel C, another trend can be seen with the ionizing radiation escape fraction. Here it seems that the higher Lyman-α escape fractions generally also have higher ionizing radiation escape fraction. This result is expected, as it is due to less dust in those lines of sight, but it requires a bit of a more in depth analysis, as they both also depend on the HI content along each line of sight, and is the reason why Lyman-α has been proposed to be used to determine the ionizing radiation escape fraction (Verhamme et al. 2015). Ionizing radiation, unlike Lyman-α radiation, is absorbed by neutral gas, and ionizes it, which means that for ionizing radiation to escape, sufficiently large HII regions need to have been formed in the galaxy, which are also the regions where Lyman-α is created. Another possibility for ionizing radiation escape is the presence of holes in the neutral gas distribution, created by feedback processes (Trebitsch et al. 2017), which would also be channels of Lyman-α escape. Overall, not only does low dust column density promote the escape of both Lyman-α and ionizing radiation, but so does low HI column density along the line of sight (Dijkstra et al. 2016). Here we can also see that the galaxies which have been chosen based on their high 3D ionizing radiation escape fraction also follow the trend and actually do not always show high ionizing radiation escape fraction in all lines of sight, and are instead on trend with the sample C of galaxies, which was selected purely on their UV magnitude. This is because ionizing radiation is thought to escape the halo through channels created by feedback (Trebitsch et al. 2017), so it escapes in patches, which might not be observed with only six lines of sight.

In panel E we see the specific star formation rate, which seems to increase with both escape fraction but more strongly with equivalent width. The increase with escape fraction is not very strong, due to a temporal offset between the creation and escape of Lyman-α radiation (Trebitsch et al. 2017), with the peak production being at the same time as the peak SFR, as the two are linked by ionizing photons. This offset is due to the time it takes for supernovae to explode and create holes in the neutral gas distribution. This can partially also be noticed in panel D where we see that the very high escape fraction lines of sight also have the lowest instantaneous star formation rate. The increase with an increased equivalent width is due to the fact that these two properties are not exactly independent. The specific star formation rate is defined as the amount of stars formed in a given time (10 Myr) per stellar mass. The equivalent width is the amount of Lyman-α flux compared to the UV continuum flux. The UV continuum is created by young stars, and most the Lyman-α emission is created by the recombination of gas which had been previously ionized by UV photons. We can thus see that both these quantities are related to the amount of young stars in the galaxy and are therefore not independent.

It is also possible to see an increase in intrinsic UV magnitudes for lower escape fractions in panel F. This means that the intrinsically brighter UV galaxies have more dust, but this might be purely a selection bias effect, as the last 13 galaxies were chosen to have similar 3D averaged escaped UV magnitudes and it is therefore obvious that out of those the intrinsically brighter galaxies will have more dust which can absorb both UV radiation and Lyman-α. Intrinsically brighter galaxies of sample C indeed tend to have a higher mass, as seen in table 4.1, where the intrinsically brightest galaxy is also the most dusty. Lastly, from panel H, it seems that lines of sight with higher escape fractions tend to be from galaxies of lower mass. This is probably due to the smaller amount of dust that is usually present in low mass galaxies (Popping et al. 2017). Panels B and G have not been mentioned as no trend can be discussed.

In fig. 4.10 I am showing the Lyman-α equivalent width as a function of the observed Lyman-α flux. The markers are the same shapes as in fig. 4.9 and the color coding is also the same, except for the luminosity per line of sight which isn't shown in fig. 4.10, as it

Figure 4.10: Lyman-α equivalent width versus Lyman-α flux per line of sight.
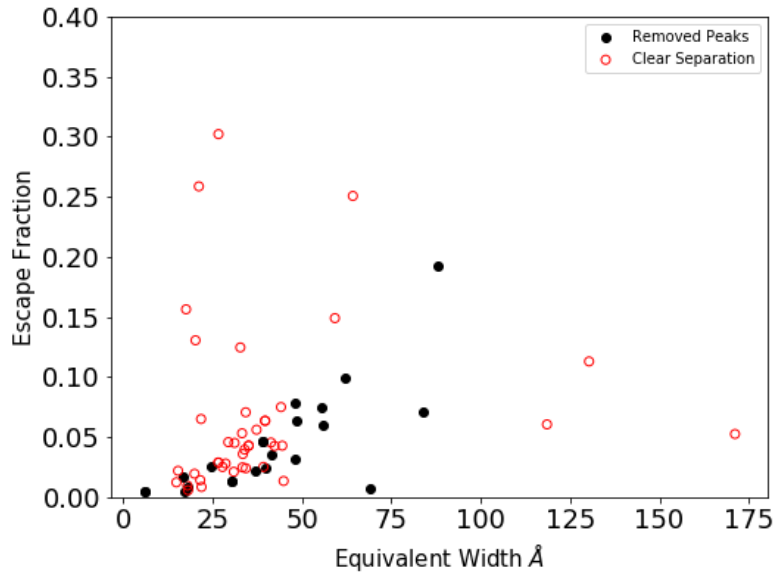
Figure 4.11: Distribution of $f_{esc}(Ly\alpha)$ against EW($Ly\alpha$) for lines of sight with clearly identified peaks (red) and removed lines of sight (black). Overall, the sources with unclear peak separation occupy the same region as the other sources.

is calculated directly from and is proportional to the flux, making it redundant. Here a clear trend can be seen in panel F, where we see that for the same Lyman-α flux value the UV magnitude decreases with increasing equivalent width. This is understandable as for the same Lyman-α flux value the equivalent width can only increase due to a decrease of continuum. The continuum used to calculate the equivalent width is just on the red side of Lyman-α, but is created from the same objects as the UV continuum, so it expected that a lower continuum, so a higher equivalent width at the same flux value would lead to a lower UV magnitude. Another weak trend can be seen in panel B, between the flux and the Lyman continuum escape fraction, as the Lyman continuum escape fraction increases with an increased flux at the same equivalent width. The reason for such a relation would be the same one as for the previous one, as a higher flux at the same equivalent width means a stronger continuum emission, which could probably be due to less dust in those lines of sight, which for a constant gas-to-dust ratio would also mean less neutral gas, explaining the higher ionizing radiation escape fraction. The other panels, A, C, D, E, G have not been discussed as no trend can be noticed.

Next, we repeat the previous analysis for the correlation between the $f_{esc}(Ly\alpha)$ and the Lyman-α peak separation, but we first need to identify the peaks that have been removed from the analysis and try to determine if this removal would have a strong effect on the results. The excluded data points are shown in fig. 4.11, in black, together with the rest of the data points, in red. The escape fraction of those lines of sight is shown against their equivalent width, as these quantities will be shown again in fig. 4.12 and fig. 4.13 respectively. Here we can see that the excluded points are not concentrated in one particular part of the plot, as it seems like they are just located where most of the data points are located. This suggests that is not problematic to the inferred results to remove these points from the overall analysis, especially as their peak separation cannot be found in a robust way.

First, in fig. 4.12 is shown the Lyman-α peak separation versus the equivalent width. In panel C is the plot color coded by the ionizing radiation escape fraction. Here we can see the ionizing radiation escape fraction increase at a given peak separation for a higher Lyman-α escape fraction. This is probably due to the fact that ionizing radiation and Lyman-α
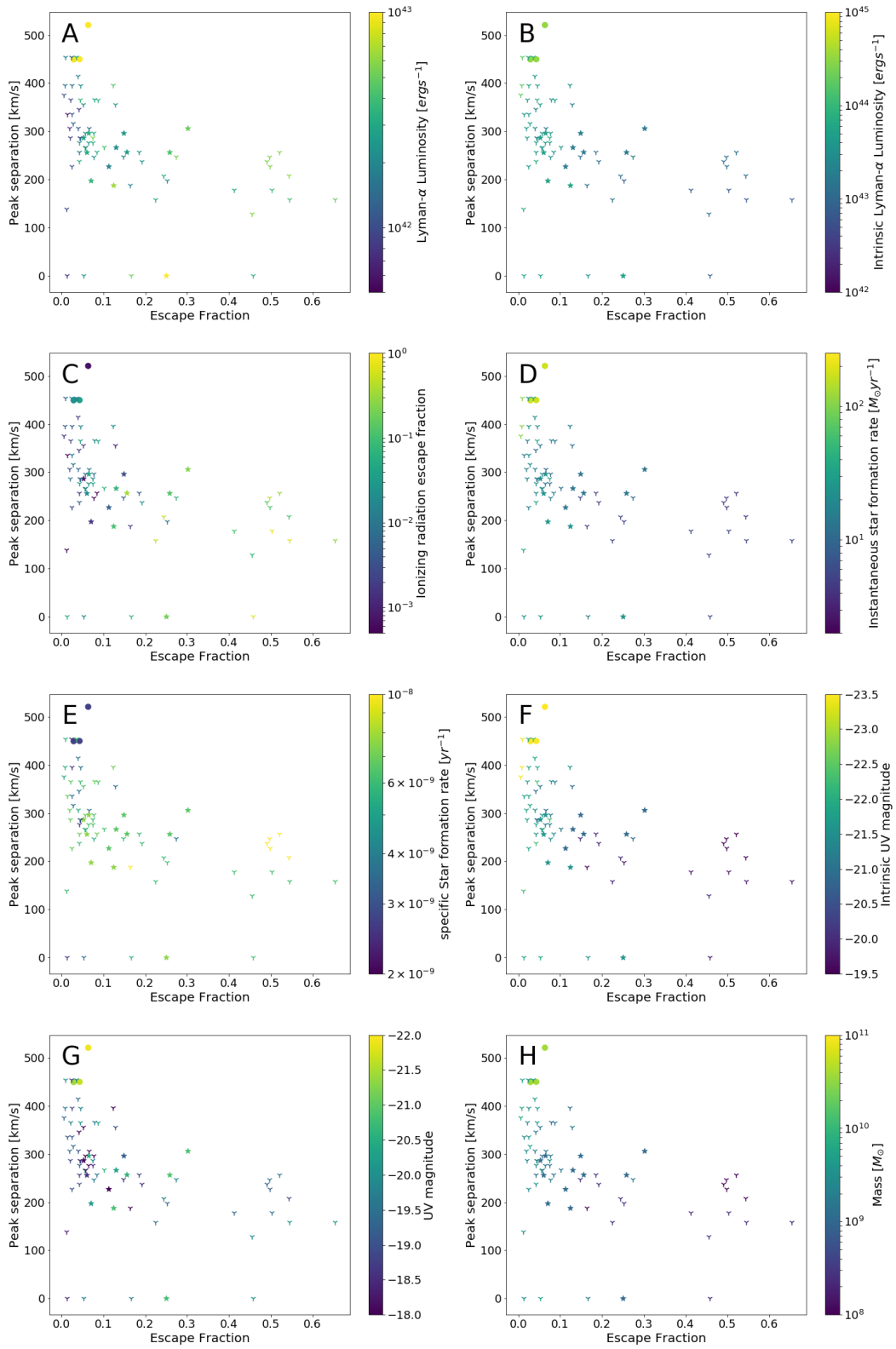
Figure 4.12: Lyman-α peak separation versus Lyman-α escape fraction
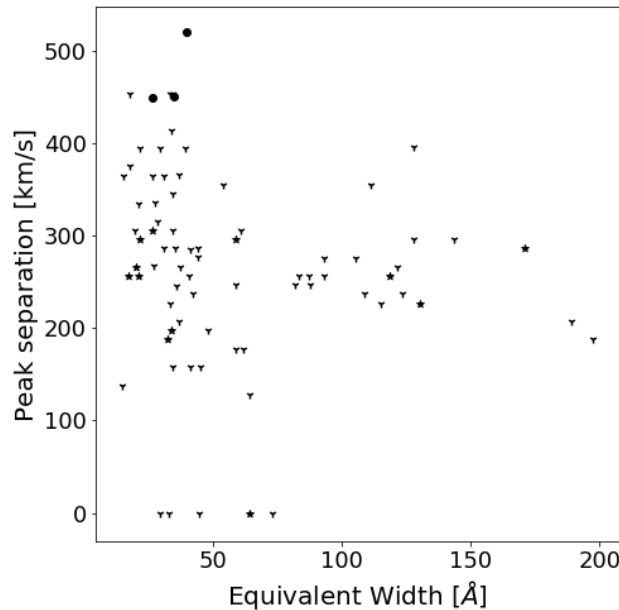
Figure 4.13: Lyman-α peak separation against Lyman-α equivalent width. A variety of $V_{sep}(Ly\alpha)$ can be achieved with the same low $EW(Ly\alpha)$, whereas high EW values have similar peak separations.

radiation escape from the same routes and to the dust distribution. As both Lyman-α and Lyman Continuum photons tend to escape from the same low channels of low gas optical depth, their escape fractions are expected to be similar for a given line of sight. Moreover, as seen in fig. 3.4, the peaks get more separated with a higher gas optical depth, so it is clear why the highest escape fractions for both kinds of radiation are at low peak separation, as a higher gas optical depth will also affect Lyman-α radiation, as it will lead to more scattering and to lower $f_{esc}(Ly\alpha)$ at a given dust density. However, Lyman-α photons are only absorbed by dust, so I expect the lines of sight of similar peak separation and higher Lyman-α escape fraction to also be those with less dust. A clearer trend can be seen in figure F, where it seems that the intrinsic UV magnitude is lower for higher escape fractions at the same peak separation. Once again this could be due to the dust content, as those galaxies probably have a similar gas optical depth along those lines of sight, hence the same peak separation, but less dust, hence the higher escape fraction. I would like to point out that the relation between the peak separation and the gas column density has some scatter, as seen in Verhamme et al. 2015, but I think that the trend is enough to explain what we see here, as it is not a very tight relation. In figure H we can see another weak trend similar to that in figure F, where it looks like for the same peak separations the mass increases as the escape fraction decreases, which is likely due to the smaller amount of dust usually present in low mass galaxies. Once again, here I have chosen not to discuss panels A, B, D, E, G as I could not see any trend.

Since I have found no clear trends between the peak separation and equivalent width and other galaxy properties, I have chosen to show these quantities without color coding, for simplicity and clarity. Here we see that at low equivalent width there is a large range of possible peak separations, whereas high equivalent widths are mostly concentrated around similar peak separations, about 200-300 km/s.

Here I would like to mention some last general details about this analysis. First of all, I have chosen not to discuss the panels which show no clear trends in fig. 4.9, fig. 4.10 and fig. 4.12, but I thought that the results from those panels would still be interesting to show as they indeed show a lack of trend. With this I wanted to show that due to

the challenging interpretation of Lyman-α, many observationally available properties are unable to conclusively determine intrinsic properties, and even the trends that I was able to determine are not very strict, which adds complexity to the study of galaxies in this line. However, from this study we can start to understand the physical reason to the scatter in observed properties. Lastly I would like to comment on the behavior of the different samples in the figures of this section. It seems like the most massive galaxy is often an outlier, and does not follow the trends very well, but what is somewhat surprising it that the other two samples have a very similar behavior. Their similar properties are probably a result of the B sample also having an UV magnitude close to -19.5, as well as star formation rates, stellar and dust masses similar to those of the galaxies in sample C.

4.1.4   Estimate of ionizing radiation escape fraction

It has been found by Izotov et al. 2018 that the peak separation correlates well with the escape fraction of ionizing photons, as both the peak separation and the escape fraction are correlated to the gas content of the galaxy (Verhamme et al. 2015). In this section I will determine if it is present in the simulated galaxies.

The ionizing radiation escape fraction is a particularly useful quantity in the study of the Epoch of Reionization, as it shows how many ionizing photons are able to escape the galaxy and therefore ionize the surrounding gas. It is very difficult to determine observationally, since it is only possible to measure the radiation that was escaped, and not the intrinsic one, although both are needed to determine the escape fraction. The intrinsic luminosity could be inferred from the Balmer emissions lines, assuming we can correct for dust, but that is not easy. Moreover, at high redshifts, $z \gtrsim 4$ the Lyman continuum is completely absorbed by the residual HI in the IGM, so even measuring the escaped Lyman continuum radiation is challenging.

A relation between the Lyman-α peak separation and the ionizing radiation escape fraction was calibrated by Izotov et al. 2018, using a set of nearby Lyman continuum leaking galaxies known as 'green peas' (Cardamone et al. 2009), due to their SDSS images, where they are round, because they are not spatially resolved, and green, due to their large amount of emission in the [OIII] line. This particular set of galaxy is useful for the study of $f_{esc}(LyC)$ as they are confirmed LyC leakers, at a redshift which is not too low that the Milky Way neutral gas would absorb the LyC radiation, but not too high that the LyC radiation would be absorbed by the neutral gas in the IGM. This relation is

$$f_{esc}(\text{LyC}) = \frac{3.23 \times 10^4}{V_{sep}^2} - \frac{1.05 \times 10^2}{V_{sep}} + 0.095 \tag{4.1}$$

This relation is empirically derived and breaks down at $V_{sep} < 140\text{km/s}$, where the relation gives unphysical values of $f_{esc}(LyC) > 1$. It can be nonetheless used to infer the escape fraction of ionizing relation, or a lower limit, in the case of low peak separations, from an observational quantity and has been also applied at high redshifts (eg Meyer et al. 2020). From the simulation and the Monte Carlo radiative transfer code I can directly compare the real $f_{esc}(LyC)$ to the one inferred from eq. (4.1), for galaxies where the peaks can be clearly identified.

In fig. 4.14, I am showing the $f_{esc}(LyC)$ measured from the simulation against the peak separation, color coded by various galaxy properties. The solid line indicates the best fit relation from Izotov et al. 2018. From this figure, the first thing to notice is that there is an overall reasonable agreement between the simulation and the observational fit, but with a large scatter, and a significant number of points that fall far from it. I would therefore say that this relation does not apply completely to the simulated sample. I have also color coded this figure, like in the previous figures, to look for a good descriptor of the outlier population, however a clear trend distinguishing the populations does not seem to be there, with the exception of a weak trend in UV magnitude. In fact, dimmer galaxies in the UV seem to be generally out of the fit, whereas galaxies on the fit seem to be brighter. The
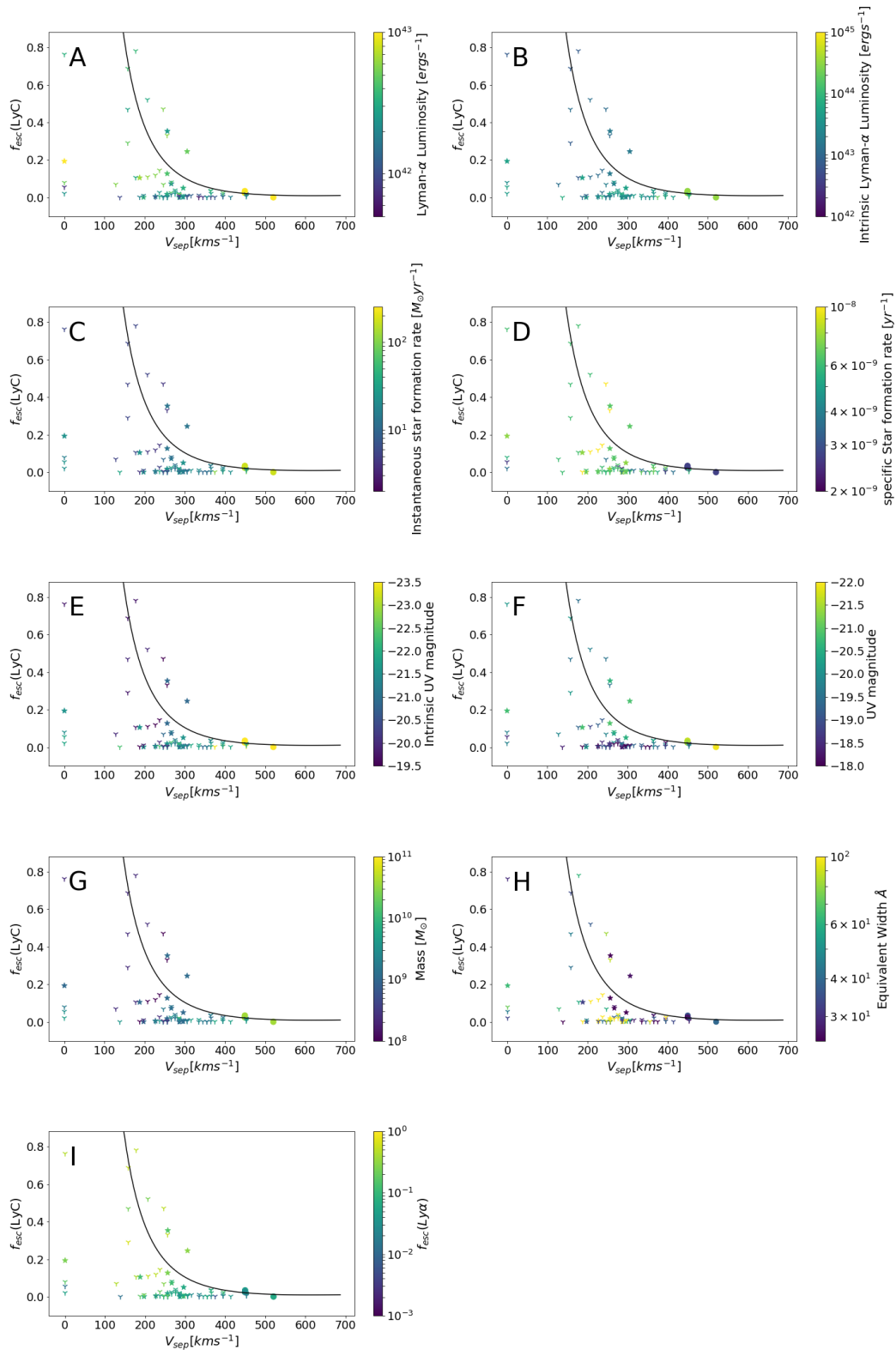
Figure 4.14: Lyman continuum escape fraction against the peak separation of the Lyman-α profile, only including the profiles with clear peak separations. In black is the relation of eq. (4.1), derived by Izotov et al. 2018. The colors are the same as in previous figures, with the addition of Lyman-α equivalent width and Lyman-α escape fraction. Overall, the relation seems to fit the data, except for points with both low $f_{esc}(LyC)$ and low V_{sep}.
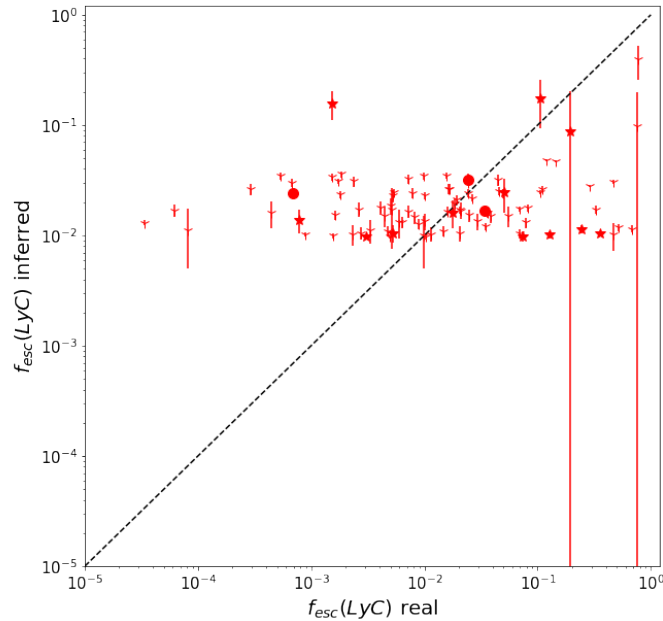
Figure 4.15: Comparison of real ionizing radiation escape fraction, as taken from the simulation, and inferred ionizing radiation escape fraction, calculated with eq. (4.1). eq. (4.1) seems to overestimate $f_{esc}(LyC)$ for the lines of sight with the lowest escape fraction.

M_{UV} used in this simulated sample and in the Izotov et al. 2018 sample is similar, with their sample being $-18 < M_{UV} < -20$, so this shouldn't be an observational bias. Instead another possibility that could explain the outliers is that the galaxies in the Izotov et al. 2018 sample were selected to have very high O32, but Katz et al. 2020 showed that it is not always the case that high O32 correlates with high $f_{esc}(LyC)$. Moreover, Green Peas are usually found in low density environments, but OBELISK is a simulation of a high density environment, as that is where most high redshift LAEs are found. Overall, the Green Peas sample is quite peculiar and their result might not necessarily apply to all galaxies.

Seeing that there are quite some data points which do not fit on the relation, I was interested to see what value of Lyman continuum escape fraction I would get from each spectra and how that compares to the correct one taken from the simulation. Since a few spectra have a peak separation $V_{sep} < 140$km/s, which leads to nonphysical $f_{esc} > 100\%$, I followed the procedure of Meyer et al. 2020, which encounters this same problem. Each spectrum was resampled by finding the Poisson noise at each point of the spectrum and varying those points using a gaussian centred on the initial value, with the Poisson noise as the standard deviation. The resampling was done 1000 times for each spectrum and the median of the escape fraction of all the resampled spectra was used as the value for the inferred ionizing radiation escape fraction. The inferred escape fraction compared to the real escape fraction is shown in fig. 4.15, where the error bars were calculated as one standard deviation around the median, so 34% on each side of the median. These errorbars are only statistical errorbars and do not include any systematics which would probably increase their size. In fig. 4.15, the dashed line indicates the one to one relation. There are only a few points that are on or close to the line, whereas most of them have either an overestimated or underestimated escape fraction. The population of overstimated escape fraction should correspond to that of both low peak separation and Lyman continuum escape fraction previously identified in fig. 4.14, as discussed earlier. It should be noted that fig. 4.15
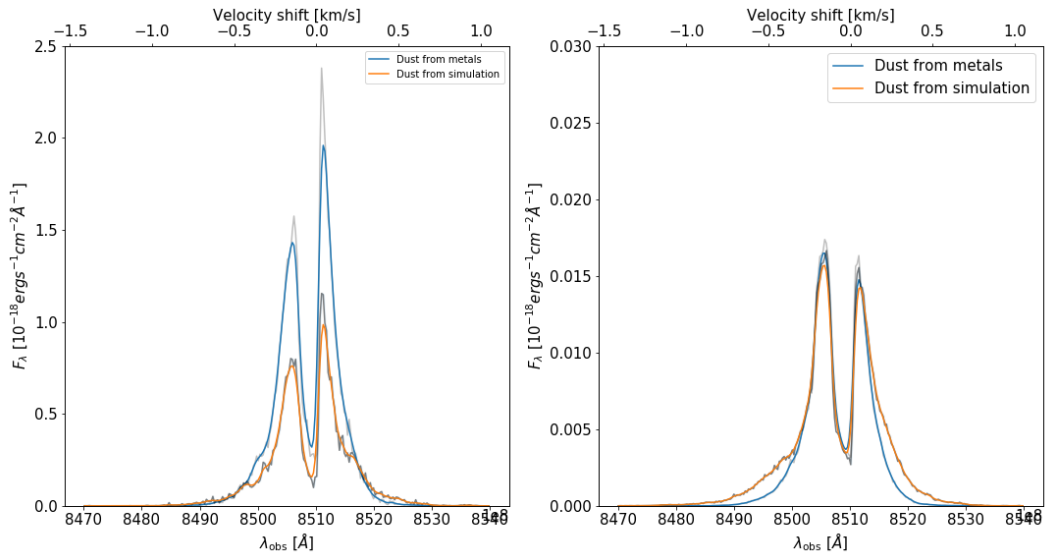
Figure 4.16: Comparison of a sample spectrum from the two dust models, both for the recombination on the left and the collision photons, on the right. The spectra have the same shape, but the recombination flux is lower for the dust from the simulation, whereas the collisions flux is almost identical.

is in logarithmic scale, so the distance between the points and the line looks amplified, and is only up to 2 dex.

Overall it seems like the relation from Izotov et al. 2018 does not fit the simulated data very well, at least at high redshift, but here it is impossible to tell if the issue is in the simulation or in the fit.

4.2   Comparison of dust models

As previously mentioned, two dust models are used, one where the dust follows the metal and another one using the dust directly from the simulation, where the dust is decoupled from the metal distribution. As of now I have only shown the results of the first model, where dust follows the metals, for consistency, but the same analysis was also performed on the other dust model. Here I will show in what ways the two models differ from each other and what kind of results they both lead to.

In fig. 4.16, I first show a comparison between the same line of sight spectra for galaxy ID 64846 for the two dust models. On the left is the comparison of the spectra from recombination photons and on the right is that of collision photons. It should be noted that the flux is not on the same scale in the two plots as the flux from the collision photons is about two orders of magnitude lower. Here we can see that the flux of the recombination photons is much more affected by the change in dust model than the flux of collision photons. When using the dust from the simulation the spectral shape of the recombination spectrum stays about the same, but the spectral flux decreases by about half. This is probably due to a more concentrated dust distribution around star forming regions, as those are the ones where Lyman-α photons from recombination are created, as already shown at the beginning of this chapter.

The idea that in the simulation dust is more concentrated around star forming regions can be checked by looking at a map of the dust, or more directly relevant to the discussion, a map of the UV attenuation, as UV light and Lyman-α photons from recombination have the same origin, and are both similarly attenuated by dust. Figure 4.17 shows the comparison between the attenuation maps for the two dust models (dust from metals on the left, dust

Figure 4.17: Map of the UV attenuation due to dust of the same galaxy, together with the relative difference between the two. The dust from the metals model seems to be more diffuse.

from simulation in the center and difference between the two models on the right) for galaxy ID 64846. In this figure the darker areas are the more attenuated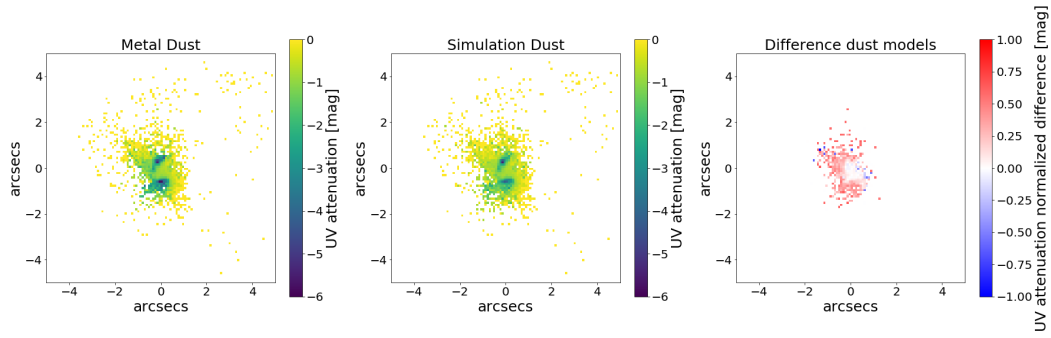, so it can be seen that the areas of high attenuation when using the dust from the simulation are smaller and restricted to the star forming regions, especially in the difference plot, where the redder areas indicate more attenuation in the metal dust model. This can explain the difference in recombination spectra seen in fig. 4.16.

Finally, fig. 4.18 shows the comparison between the two dust models. In each of these plots, the black dashed line represents a 1:1 relation, which is where the points should fall if the values were the same for both models. Panel A shows that the intrinsic luminosity is the same in both models, which is clear since it does not depend in any way on the dust distribution. Then, in panel B, the escaped Lyman-α luminosity is compared, and here it can be noted that when using the dust from the simulation, there is more absorption, as these values are consistently lower than those of the other dust model. This stronger absorption noticed in panel B would also affect other quantities, such as the Lyman-α equivalent width, both 3D, in panel C, and per line of sight, in panel E, the Lyman-α escape fraction, both 3D, in panel D, and per line of sight, in panel F, and the flux, in panel G. Indeed, in all of these cases, the dust model used in the simulation produces lower values, consistent with more absorption than in the case of the metal dust model. This behavior could be due to the difference in dust distribution shown in fig. 4.17. A surprising feature in these panels is that the equivalent widths per line of sight are much lower in the case of the simulation dust, and especially at high EW they look to be much further from the dashed lines than other values in other panels. This can be explained by the fact that the UV is less absorbed than Lyman-α using the dust from the simulation. In panel H I am showing a comparison of the absolute UV magnitudes. Here we can see that the magnitudes measured using the simulation dust model are consistently higher than in the metals model case. This is likely to be due to the difference in dust distribution, since a more diffuse dust distribution as in the case of the metals model would attenuate much of the radiation coming from outside of star forming regions, leading to an overall lower UV magnitude. Another possibility could be an underestimation of the extinction curve in the UV in the simulation. Lastly, panel I is the peak separation comparison. Once again here I have chosen to omit the unclear peaks. It is interesting to note that the peak separation between the models is quite consistent, which seems to tells us that the dust model might not matter strongly for the shape of the spectrum, which is a very encouraging result. It does seem like the scatter increases at high peak separations, which makes sense, as these points will be the most massive galaxies, which will typically have more dust. This hints that the the differences in the models might start to become important with high dust contents.
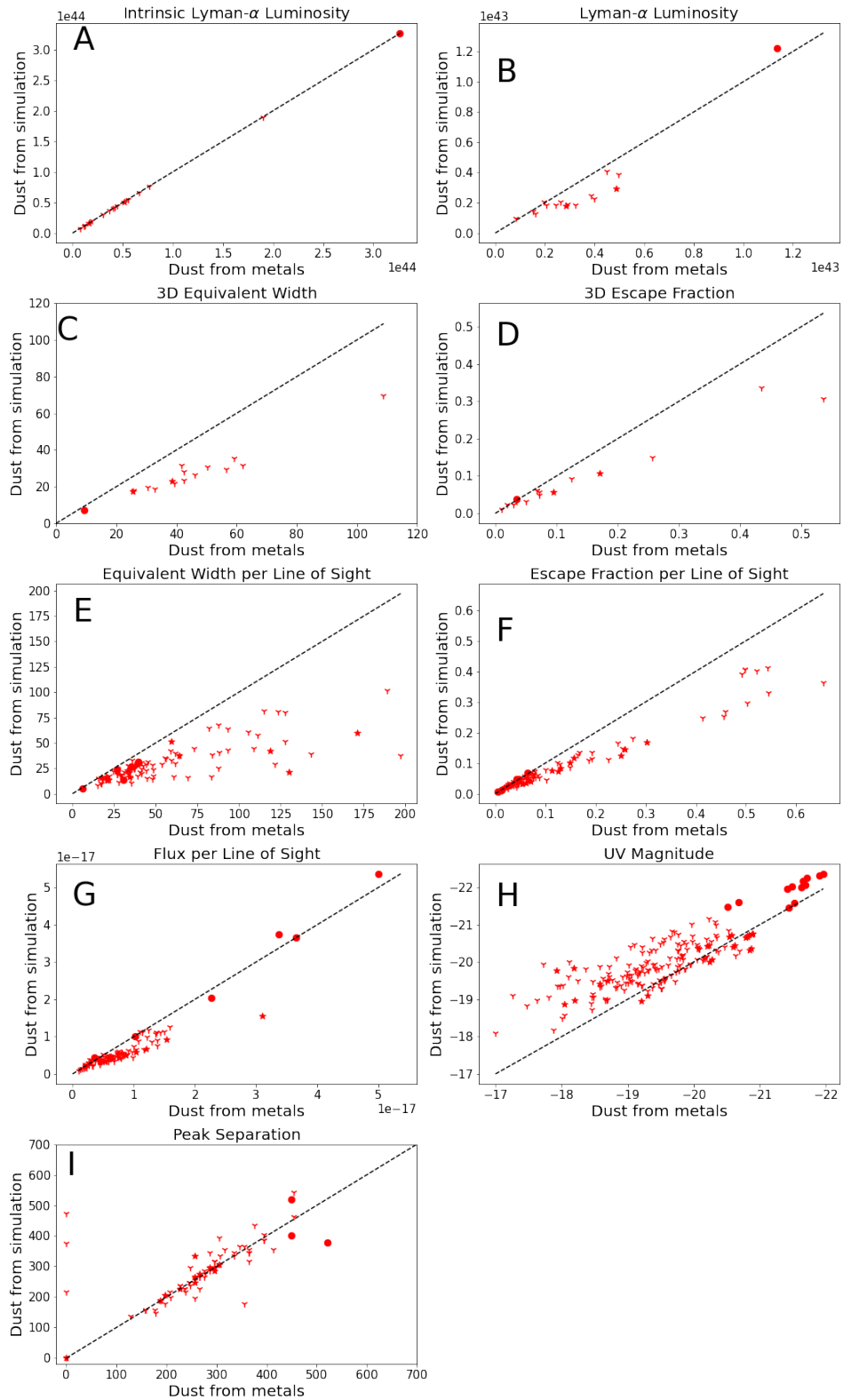
Figure 4.18: Comparison of results from the two dust models. Most values are consistently lower for the simulation dust, except for the absolute UV magnitude, which is higher, and the peak separation, which is very consistent between the two models.

Chapter 5

Conclusions

In this thesis I have studied Lyman-α Emitters at high redshift ($z = 6$) by performing radiative transfer and synthetic observations on a set of galaxies taken from the cosmological radiation-hydrodynamics simulation OBELISK. With these I measured various properties, such as the luminosity, the equivalent width and the peak separation, which I correlated with intrinsic galaxy properties such as the intrinsic Lyman-α luminosity, the absolute UV magnitude, and the star formation rate, and the escape fraction of Lyman-α and ionizing photons. I also studied the ionizing radiation escape fraction and compared it to that derived from the Lyman-α spectrum, following an empirical relation. Lastly, I assessed the importance of dust physics on these properties by comparing two dust models and have found a small albeit systematic effect.

Due to the resonant nature of Lyman-α, which can lead to extremely different observations of the same galaxy when changing the angle of observation, relations between the observational and intrinsic properties of galaxies are weak and include high amounts of scatter. In the previous sections some trends have been identified, but nothing that could be reliably used in observation of real life LAEs to determine some intrinsic properties. From this part of the analysis I can only conclude that while LAEs are very useful for studies of the Epoch of Reionization, it is extremely complicated to study them using only the Lyman-α line. The addition of non resonant lines stemming from similar processes, like Hα could however aid in the understanding of the gas distribution and on the kinetic structures of these galaxies. This has not been done yet at high redshift, as no telescope had been able to observe Hα emission from such distant galaxies yet, but JWST will be able to, hopefully opening up the road to more in depth studies of this class of galaxies.

I have used the synthetic observation results to study the relation found by Izotov et al. 2018, which is an empirical relation calibrated at low redshift linking the Lyman-α peak separation, an observable quantity, to the ionizing radiation escape fraction. This quantity is particularly interesting at high redshift, as an understanding of which kind of galaxies have a high escape fraction of ionizing radiation should lead to a better understanding of the process of Reionization. I have found that this relation is in reasonable agreement with my galaxy selection but it seems to not completely apply as it excludes very low ionizing radiation escape fraction with very low peak separation galaxies. The escape fraction of this outlier population of galaxies is generally overestimated by this relation. There is however no other intrinsic characteristic that would distinguish the population of galaxies not on the relation from those for which the relation works well. A possibility that could not be studied here is that the sample of simulated galaxies could have low O32. The sample used by Izotov et al. 2018 was chosen to have very high O32, but Katz et al. 2020 have shown that high O32 not always correlated with high $f_{esc}(LyC)$. More studies are therefore needed to better understand the relation between Lyman-α peak separation and ionizing radiation escape fraction, as the Green Peas galaxies are a very peculiar set of galaxies so relations derived from their study might not be valid for all galaxies, and because quantifying the escape of ionizing photons is very important to the study of reionization.

Lastly, I have found that the spectral properties of Lyman-α seem relatively robust to the dust model, as the two models produce similar results, with a small systematic effect. This is extremely encouraging, as adding the dust in post processing, by following the metals is much easier. Moreover, most studies involving dust in simulations have been performed using this or similar dust models, where the dust is added later, and my results would point to the fact that using a dust model where dust is simulated together with the gas would not change the results significantly. There is however some spatial variation between the two models, and a hint that the differences in dust models might become increasingly important with increasing dust contents. Both of these effects should be studied more in depth, to fully understand the effect that dust physics has on Lyman-α emission, and would be interesting follow ups to this work.

5.1   Improvements

Overall these results could be improved by using a larger sample of galaxies a maybe a wider variety of lines of sight per galaxy. Many characteristics of Lyman-α are extremely line of sight dependent so a more in depth study of this relation seems needed. Unfortunately, due to how long it takes to run RASCAS with the peeling off algorithm, especially for a high number of photons, I was unable to analyze more galaxies. As the time to complete this work was somewhat limited, I decided to focus on a smaller sample of galaxies to achieve a more in depth analysis. A variety of selection methods would also be interesting to study and compare.

Other possibilities could be spatially resolved studies, where it could be possible to study the escape paths of Lyman-α and ionizing photons, to determine if they indeed are the same or not, or to study the dust distribution in detail. CGM studies would also be valuable, to study traces of inflows and outflows.

Another possible improvement to this study could be sampling galaxies of similar properties but in a varied selection of redshifts. Due again to the length of time it takes to perform the radiative transfer, I was only able to study a limited sample of galaxies, and decided to focus on a single redshift, but I would find it interesting to analyze how the properties of LAEs vary with time.

Bibliography

Barkana, Rennan and Abraham Loeb (July 2001). "In the beginning: the first sources of light and the reionization of the universe". In: *Physics Reports* 349.2, pp. 125–238. DOI: 10.1016/s0370-1573(01)00019-9. URL: https://doi.org/10.1016%2Fs0370-1573%2801%2900019-9.

Becker, George D., James S. Bolton, and Adam Lidz (2015). "Reionisation and High-Redshift Galaxies: The View from Quasar Absorption Lines". In: *Publications of the Astronomical Society of Australia* 32. DOI: 10.1017/pasa.2015.45. URL: https://doi.org/10.1017%2Fpasa.2015.45.

Burgh, Eric B., Stephan R. McCandliss, and Paul D. Feldman (Aug. 2002). "Rocket Observations of Far-Ultraviolet Dust Scattering in NGC 2023". In: *The Astrophysical Journal* 575.1, pp. 240–249. DOI: 10.1086/341194. URL: https://doi.org/10.1086%2F341194.

Cantalupo, Sebastiano, Cristiano Porciani, and Simon J. Lilly (Jan. 2008). "Mapping Neutral Hydrogen during Reionization with the Ly Emission from Quasar Ionization Fronts". In: *The Astrophysical Journal* 672.1, pp. 48–58. DOI: 10.1086/523298. URL: https://doi.org/10.1086%2F523298.

Cantalupo, Sebastiano et al. (July 2005). "Fluorescent Lyα Emission from the High-Redshift Intergalactic Medium". In: *ApJ* 628.1, pp. 61–75. DOI: 10.1086/430758. arXiv: astro-ph/0504015 [astro-ph].

Cardamone, Carolin et al. (Nov. 2009). "Galaxy Zoo Green Peas: discovery of a class of compact extremely star-forming galaxies". In: *Monthly Notices of the Royal Astronomical Society* 399.3, pp. 1191–1205. DOI: 10.1111/j.1365-2966.2009.15383.x. URL: https://doi.org/10.1111%2Fj.1365-2966.2009.15383.x.

Dayal, Pratika and Andrea Ferrara (Dec. 2018). "Early galaxy formation and its large-scale effects". In: 780, pp. 1–64. DOI: 10.1016/j.physrep.2018.10.002. arXiv: 1809.09136 [astro-ph.GA].

Dekel, Avishai and Yuval Birnboim (May 2006). "Galaxy bimodality due to cold flows and shock heating". In: *MNRAS* 368.1, pp. 2–20. DOI: 10.1111/j.1365-2966.2006.10145.x. arXiv: astro-ph/0412300 [astro-ph].

Dijkstra, Mark (2014). "Lyα Emitting Galaxies as a Probe of Reionisation". In: *Publications of the Astronomical Society of Australia* 31. DOI: 10.1017/pasa.2014.33. URL: https://doi.org/10.1017%2Fpasa.2014.33.

Dijkstra, Mark, Max Gronke, and Aparna Venkatesan (Sept. 2016). "THE Ly<i</i–LyC CONNECTION: EVIDENCE FOR AN ENHANCED CONTRIBUTION OF UV-FAINT GALAXIES TO COSMIC REIONIZATION". In: *The Astrophysical Journal* 828.2, p. 71. DOI: 10.3847/0004-637x/828/2/71. URL: https://doi.org/10.3847%2F0004-637x%2F828%2F2%2F71.

Dijkstra, Mark, Zoltan Haiman, and Marco Spaans (Sept. 2006). "Ly Radiation from Collapsing Protogalaxies. I. Characteristics of the Emergent Spectrum". In: *The Astrophysical Journal* 649.1, pp. 14–36. DOI: 10.1086/506243. URL: https://doi.org/10.1086%2F506243.

Dijkstra, Mark and Abraham Loeb (May 2008). "The polarization of scattered LyÎ ± radiation around high-redshift galaxies". In: *Monthly Notices of the Royal Astronomical Society* 386.1, pp. 492–504. DOI: 10.1111/j.1365-2966.2008.13066.x. URL: https://doi.org/10.1111%2Fj.1365-2966.2008.13066.x.

Dijkstra, Mark and Eduard Westra (Feb. 2010). "Star formation indicators and line equivalent width in Ly galaxies". In: *Monthly Notices of the Royal Astronomical Society* 401.4, pp. 2343–2348. DOI: 10.1111/j.1365-2966.2009.15859.x. URL: https://doi.org/10.1111%2Fj.1365-2966.2009.15859.x.

Dijkstra, Mark et al. (2020). *Lyman-alpha as an astrophysical and cosmological tool SAAS-Fee Advanced Course 46*. Springer.

Fan, Xiaohui, C. L. Carilli, and B. Keating (Sept. 2006). "Observational Constraints on Cosmic Reionization". In: 44.1, pp. 415–462. DOI: 10.1146/annurev.astro.44.051905.092514. arXiv: astro-ph/0602375 [astro-ph].

Gazagnes, S. et al. (July 2020). "The origin of the escape of Lyman α and ionizing photons in Lyman continuum emitters". In: 639, A85, A85. DOI: 10.1051/0004-6361/202038096. arXiv: 2005.07215 [astro-ph.GA].

Gnedin, Nickolay Y., Andrey V. Kravtsov, and Hsiao-Wen Chen (Jan. 2008). "Escape of Ionizing Radiation from High-Redshift Galaxies". In: *The Astrophysical Journal* 672.2, pp. 765–775. DOI: 10.1086/524007. URL: https://doi.org/10.1086/524007.

Goerdt, Tobias et al. (June 2010). "Gravity-driven Ly blobs from cold streams into galaxies". In: *Monthly Notices of the Royal Astronomical Society* 407.1, pp. 613–631. DOI: 10.1111/j.1365-2966.2010.16941.x. URL: https://doi.org/10.1111%2Fj.1365-2966.2010.16941.x.

Griffiths, David Jeffery and Darrell F. Schroeter (2018). *Introduction to quantum mechanics*. Cambridge University Press.

Gronke, Max and Simeon Bird (Feb. 2017). "Giant Lyman-alpha Nebulae in the Illustris Simulation". In: *ApJ* 835.2, 207, p. 207. DOI: 10.3847/1538-4357/835/2/207. arXiv: 1605.03598 [astro-ph.GA].

Gunn, James E. and Bruce A. Peterson (Nov. 1965). "On the Density of Neutral Hydrogen in Intergalactic Space." In: *ApJ* 142, pp. 1633–1636. DOI: 10.1086/148444.

Harrington, J. Patrick (Feb. 1974). "The scattering of resonance-line radiation in the limit of large optical depth-11. Reflection and transmission of radiation incident upon a slab". In: *MNRAS* 166, pp. 373–382. DOI: 10.1093/mnras/166.2.373.

Hayes, Matthew (2015). "Lyman Alpha Emitting Galaxies in the Nearby Universe". In: *Publications of the Astronomical Society of Australia* 32. DOI: 10.1017/pasa.2015.25. URL: https://doi.org/10.1017%2Fpasa.2015.25.

Henyey, L. G. and J. L. Greenstein (Jan. 1941). "Diffuse radiation in the Galaxy." In: *ApJ* 93, pp. 70–83. DOI: 10.1086/144246.

Hui, L. and N. Y. Gnedin (Nov. 1997). "Equation of state of the photoionized intergalactic medium". In: *Monthly Notices of the Royal Astronomical Society* 292.1, pp. 27–42. DOI: 10.1093/mnras/292.1.27. URL: https://doi.org/10.1093%2Fmnras%2F292.1.27.

Izotov, Y I et al. (May 2018). "Low-redshift Lyman continuum leaking galaxies with high [O iii]/[O ii] ratios". In: *Monthly Notices of the Royal Astronomical Society* 478.4, pp. 4851–4865. DOI: 10.1093/mnras/sty1378. URL: https://doi.org/10.1093%2Fmnras%2Fsty1378.

Kashikawa, Nobunari et al. (Sept. 2006). "The End of the Reionization Epoch Probed by Ly Emitters at<iz</i= 6.5 in the Subaru Deep Field". In: *The Astrophysical Journal* 648.1, pp. 7–22. DOI: 10.1086/504966. URL: https://doi.org/10.1086%2F504966.

Katz, Harley et al. (Aug. 2020). "New methods for identifying Lyman continuum leakers and reionization-epoch analogues". In: *Monthly Notices of the Royal Astronomical Society* 498.1, pp. 164–180. DOI: 10.1093/mnras/staa2355. URL: https://doi.org/10.1093%2Fmnras%2Fstaa2355.

Kereš, Dušan et al. (May 2009). "Galaxies in a simulated ΛCDM Universe - I. Cold mode and hot cores". In: *Monthly Notices of the Royal Astronomical Society* 395.1, pp. 160–179. DOI: 10.1111/j.1365-2966.2009.14541.x. URL: https://doi.org/10.1111%2Fj.1365-2966.2009.14541.x.

Laor, Ari and Bruce T. Draine (Jan. 1993). "Spectroscopic Constraints on the Properties of Dust in Active Galactic Nuclei". In: *ApJ* 402, p. 441. DOI: 10.1086/172149.

Laursen, Peter (2010). "Interpreting Lyman radiation from young, dusty galaxies". In: DOI: 10.48550/ARXIV.1012.3175. URL: https://arxiv.org/abs/1012.3175.

Laursen, Peter, Jesper Sommer-Larsen, and Anja C. Andersen (Oct. 2009). "Ly RADIATIVE TRANSFER WITH DUST: ESCAPE FRACTIONS FROM SIMULATED HIGH-REDSHIFT GALAXIES". In: *The Astrophysical Journal* 704.2, pp. 1640–1656. DOI: 10.1088/0004-637x/704/2/1640. URL: https://doi.org/10.1088%2F0004-637x%2F704%2F2%2F1640.

Laursen, Peter, Jesper Sommer-Larsen, and Alexei O. Razoumov (Jan. 2011). "INTERGALACTIC TRANSMISSION AND ITS IMPACT ON THE Ly LINE". In: *The Astrophysical Journal* 728.1, p. 52. DOI: 10.1088/0004-637x/728/1/52. URL: https://doi.org/10.1088%2F0004-637x%2F728%2F1%2F52.

Leclercq, Floriane et al. (Dec. 2017). "The MUSE Hubble Ultra Deep Field Survey. VIII. Extended Lyman-α haloes around high-z star-forming galaxies". In: 608, A8, A8. DOI: 10.1051/0004-6361/201731480. arXiv: 1710.10271 [astro-ph.GA].

Li, Aigen and B. T. Draine (June 2001). "Infrared Emission from Interstellar Dust. II. The Diffuse Interstellar Medium". In: *The Astrophysical Journal* 554.2, pp. 778–802. DOI: 10.1086/323147. URL: https://doi.org/10.1086%2F323147.

Mason, Charlotte A et al. (Mar. 2019). "Inferences on the timeline of reionization at z ~ 8 from the KMOS Lens-Amplified Spectroscopic Survey". In: *Monthly Notices of the Royal Astronomical Society* 485.3, pp. 3947–3969. DOI: 10.1093/mnras/stz632. URL: https://doi.org/10.1093%2Fmnras%2Fstz632.

Matthee, Jorryt et al. (Nov. 2018). "Confirmation of double peaked Ly<i></i> emission at <iz</i = 6.593". In: *Astronomy &amp Astrophysics* 619, A136. DOI: 10.1051/0004-6361/201833528. URL: https://doi.org/10.1051%2F0004-6361%2F201833528.

McQuinn, Matthew et al. (June 2008). "Probing the neutral fraction of the IGM with GRBs during the epoch of reionization". In: *Monthly Notices of the Royal Astronomical Society*, ???–??? DOI: 10.1111/j.1365-2966.2008.13271.x. URL: https://doi.org/10.1111%2Fj.1365-2966.2008.13271.x.

Meyer, Romain A et al. (Oct. 2020). "Double-peaked Lyman emission at <iz</i = 6.803: a reionization-era galaxy self-ionizing its local H <scpii</scp bubble". In: *Monthly Notices of the Royal Astronomical Society* 500.1, pp. 558–564. DOI: 10.1093/mnras/staa3216. URL: https://doi.org/10.1093%2Fmnras%2Fstaa3216.

Michel-Dansac, L. et al. (Mar. 2020). "RASCAS: RAdiation SCattering in Astrophysical Simulations". In: *Astronomy &amp Astrophysics* 635, A154. DOI: 10.1051/0004-6361/201834961. URL: https://doi.org/10.1051%2F0004-6361%2F201834961.

Mitchell, Peter D et al. (Jan. 2021). "Tracing the simulated high-redshift circum-galactic medium with Lyman emission". In: *Monthly Notices of the Royal Astronomical Society*. DOI: 10.1093/mnras/stab035. URL: https://doi.org/10.1093%2Fmnras%2Fstab035.

Morrison, John (2015). *Modern physics - for scientists and Engineers*. Elsevier Science Publishing Co.

Neufeld, David A. (Feb. 1990). "The Transfer of Resonance-Line Radiation in Static Astrophysical Media". In: *ApJ* 350, p. 216. DOI: 10.1086/168375.

Ocvirk, P., C. Pichon, and R. Teyssier (Oct. 2008). "Bimodal gas accretion in the Horizon-MareNostrum galaxy formation simulation". In: *Monthly Notices of the Royal Astronomical Society*. DOI: 10.1111/j.1365-2966.2008.13763.x. URL: https://doi.org/10.1111%2Fj.1365-2966.2008.13763.x.

Orlitová, I. et al. (Aug. 2018). "Puzzling Lyman-alpha line profiles in green pea galaxies". In: 616, A60, A60. DOI: 10.1051/0004-6361/201732478. arXiv: 1806.01027 [astro-ph.GA].

Orsi, Alvaro, Cedric G. Lacey, and Carlton M. Baugh (July 2012). "Can galactic outflows explain the properties of Ly emitters?" In: *Monthly Notices of the Royal Astronomical Society* 425.1, pp. 87–115. DOI: 10.1111/j.1365-2966.2012.21396.x. URL: https://doi.org/10.1111%2Fj.1365-2966.2012.21396.x.

Ouchi, Masami, Yoshiaki Ono, and Takatoshi Shibuya (Aug. 2020). "Observations of the Lyman- Universe". In: *Annual Review of Astronomy and Astrophysics* 58.1, pp. 617–659.

DOI: 10.1146/annurev-astro-032620-021859. URL: https://doi.org/10.1146%2Fannurev-astro-032620-021859.

Ouchi, Masami et al. (Nov. 2013). "AN INTENSELY STAR-FORMING GALAXY AT<iz</i~ 7 WITH LOW DUST AND METAL CONTENT REVEALED BY DEEP ALMA AND<iHST</iOBSERVATION In: *The Astrophysical Journal* 778.2, p. 102. DOI: 10.1088/0004-637x/778/2/102. URL: https://doi.org/10.1088%2F0004-637x%2F778%2F2%2F102.

Partridge, R. B. and P. J. E. Peebles (Mar. 1967). "Are Young Galaxies Visible?" In: *ApJ* 147, p. 868. DOI: 10.1086/149079.

Pei, Yichuan C. (Aug. 1992). "Interstellar Dust from the Milky Way to the Magellanic Clouds". In: *ApJ* 395, p. 130. DOI: 10.1086/171637.

Planck Collaboration et al. (Dec. 2016). "Planck intermediate results. XLVII. Planck constraints on reionization history". In: 596, A108, A108. DOI: 10.1051/0004-6361/201628897. arXiv: 1605.03507 [astro-ph.CO].

Popping, Gergö, Rachel S. Somerville, and Maud Galametz (June 2017). "The dust content of galaxies from z = 0 to z = 9". In: *Monthly Notices of the Royal Astronomical Society* 471.3, pp. 3152–3185. DOI: 10.1093/mnras/stx1545. URL: https://doi.org/10.1093%2Fmnras%2Fstx1545.

Raskutti, Sudhir et al. (Apr. 2012). "Thermal constraints on the reionization of hydrogen by Population II stellar sources". In: *Monthly Notices of the Royal Astronomical Society* 421.3, pp. 1969–1981. ISSN: 0035-8711. DOI: 10.1111/j.1365-2966.2011.20401.x. eprint: https://academic.oup.com/mnras/article-pdf/421/3/1969/5835775/mnras0421-1969.pdf. URL: https://doi.org/10.1111/j.1365-2966.2011.20401.x.

Rosdahl, J. and J. Blaizot (June 2012). "Extended Lyα emission from cold accretion streams". In: *MNRAS* 423.1, pp. 344–366. DOI: 10.1111/j.1365-2966.2012.20883.x. arXiv: 1112.4408 [astro-ph.CO].

Rosdahl, J. et al. (Oct. 2013). "ramses-rt: radiation hydrodynamics in the cosmological context". In: *Monthly Notices of the Royal Astronomical Society* 436.3, pp. 2188–2231. DOI: 10.1093/mnras/stt1722. URL: https://doi.org/10.1093%2Fmnras%2Fstt1722.

Rosdahl, J. et al. (June 2018). "The SPHINX Cosmological Simulations of the First Billion Years: the Impact of Binary Stars on Reionization72". In: *Monthly Notices of the Royal Astronomical Society*. DOI: 10.1093/mnras/sty1655. URL: https://doi.org/10.1093%2Fmnras%2Fsty1655.

Saintonge, Amelie and Barbara Catinella (2022). *The cold interstellar medium of galaxies in the Local Universe*. DOI: 10.48550/ARXIV.2202.00690. URL: https://arxiv.org/abs/2202.00690.

Schiminovich, D. et al. (Dec. 2001). "The Narrowband Ultraviolet Imaging Experiment for Wide-Field Surveys. I. Dust-scattered Continuum". In: *The Astrophysical Journal* 563.2, pp. L161–L164. DOI: 10.1086/338656. URL: https://doi.org/10.1086%2F338656.

Schroeder, Joshua, Andrei Mesinger, and Zoltá n Haiman (Nov. 2012). "Evidence of Gunn–Peterson damping wings in high-z quasar spectra: strengthening the case for incomplete reionization at z ~ 6–7". In: *Monthly Notices of the Royal Astronomical Society* 428.4, pp. 3058–3071. DOI: 10.1093/mnras/sts253. URL: https://doi.org/10.1093%2Fmnras%2Fsts253.

Sobral, David and Jorryt Matthee (Mar. 2019). "Predicting Ly<i</i escape fractions with a simple observable". In: *Astronomy &amp Astrophysics* 623, A157. DOI: 10.1051/0004-6361/201833075. URL: https://doi.org/10.1051%2F0004-6361%2F201833075.

Sokasian, A., T. Abel, and L. Hernquist (May 2002). "The epoch of helium reionization". In: *Monthly Notices of the Royal Astronomical Society* 332.3, pp. 601–616. DOI: 10.1046/j.1365-8711.2002.05291.x. URL: https://doi.org/10.1046%2Fj.1365-8711.2002.05291.x.

Teyssier, R. (Apr. 2002). "Cosmological hydrodynamics with adaptive mesh refinement". In: *Astronomy &amp Astrophysics* 385.1, pp. 337–364. DOI: 10.1051/0004-6361:20011817. URL: https://doi.org/10.1051%2F0004-6361%3A20011817.

Trebitsch, Maxime et al. (May 2017). "Fluctuating feedback-regulated escape fraction of ionizing radiation in low-mass, high-redshift galaxies". In: *Monthly Notices of the Royal*

Astronomical Society 470.1, pp. 224–239. DOI: `10.1093/mnras/stx1060`. URL: `https://doi.org/10.1093%2Fmnras%2Fstx1060`.

Trebitsch, Maxime et al. (Sept. 2021). "The OBELISK simulation: Galaxies contribute more than AGN to H I reionization of protoclusters". In: 653, A154, A154. DOI: `10.1051/0004-6361/202037698`. arXiv: `2002.04045 [astro-ph.GA]`.

Verhamme, A., D. Schaerer, and A. Maselli (Sept. 2006). "3D Lyα radiation transfer". In: *Astronomy &amp Astrophysics* 460.2, pp. 397–413. DOI: `10.1051/0004-6361:20065554`. URL: `https://doi.org/10.1051%2F0004-6361%3A20065554`.

Verhamme, A. et al. (Oct. 2012). "Lyman-<i</iemission properties of simulated galaxies: interstellar medium structure and inclination effects". In: *Astronomy &amp Astrophysics* 546, A111. DOI: `10.1051/0004-6361/201218783`. URL: `https://doi.org/10.1051%2F0004-6361%2F201218783`.

Verhamme, A. et al. (May 2015). "Using Lyman-<i</ito detect galaxies that leak Lyman continuum". In: *Astronomy &amp Astrophysics* 578, A7. DOI: `10.1051/0004-6361/201423978`. URL: `https://doi.org/10.1051%2F0004-6361%2F201423978`.

Verhamme, A. et al. (Dec. 2016). "Lyman-<i</ispectral properties of five newly discovered Lyman continuum emitters". In: *Astronomy &amp Astrophysics* 597, A13. DOI: `10.1051/0004-6361/201629264`. URL: `https://doi.org/10.1051%2F0004-6361%2F201629264`.

Weingartner, Joseph C. and B. T. Draine (Feb. 2001). "Dust Grain–Size Distributions and Extinction in the Milky Way, Large Magellanic Cloud, and Small Magellanic Cloud". In: *The Astrophysical Journal* 548.1, pp. 296–309. DOI: `10.1086/318651`. URL: `https://doi.org/10.1086%2F318651`.

Whitney, B. A. (Mar. 2011). "Monte Carlo radiative transfer". In: *Bulletin of the Astronomical Society of India* 39, pp. 101–127. arXiv: `1104.4990 [astro-ph.SR]`.

Wyithe, J. Stuart B., Abraham Loeb, and Chris Carilli (Aug. 2005). "Improved Constraints on the Neutral Intergalactic Hydrogen Surrounding Quasars at Redshifts z > 6". In: *The Astrophysical Journal* 628.2, pp. 575–582. DOI: `10.1086/430874`. URL: `https://doi.org/10.1086%2F430874`.

Yusef-Zadeh, F., M. Morris, and R. L. White (Mar. 1984). "Bipolar reflection nebulae : Monte Carlo simulations." In: *ApJ* 278, pp. 186–194. DOI: `10.1086/161780`.

Zaroubi, Saleem (Sept. 2012). "The Epoch of Reionization". In: *The First Galaxies*. Springer Berlin Heidelberg, pp. 45–101. DOI: `10.1007/978-3-642-32362-1_2`. URL: `https://doi.org/10.1007%2F978-3-642-32362-1_2`.

Zheng, Zheng and Jordi Miralda-Escude (Oct. 2002). "Monte Carlo Simulation of Lyα Scattering and Application to Damped Lyα Systems". In: *The Astrophysical Journal* 578.1, pp. 33–42. DOI: `10.1086/342400`. URL: `https://doi.org/10.1086%2F342400`.

Appendix

Appendix A - Example of RASCAS parameter file

The following is an example of one of the parameter files used to run RASCAS together with the peeling algorithm

```
!————————————————————————————————————————
[RASCAS]
  DomDumpDir    = directory_where_domain_and_mesh_files_are
  PhotonICFile  = path_to_the_photonsIC_file
  fileout       = path_to_the_photons_results_file
  nbundle       = 10
  verbose       = T
!————————————————————————————————————————


!————————————————————————————————————————
[worker]
  verbose = T
!————————————————————————————————————————


!————————————————————————————————————————
[master]
  verbose = T
  restart       = F
  PhotonBakFile = path_to_the_photons_backup_file
  dt_backup     = time_in_seconds_between_2_backups
!————————————————————————————————————————


!————————————————————————————————————————
[gas_composition]
# mixture parameters
  deut2H_nb_ratio      = 3.000E-05
  f_ion                = 0.01
  Zref                 = 0.005    ! OK for LMC dust model.
# overwrite parameters
  gas_overwrite        = F
!————————————————————————————————————————


!————————————————————————————————————————
[HI]
  recoil     = T
  isotropic = F
  HI_core_skip = F
```

```
  xcritmax       = 1000.
!
```
```
!
[ Deuterium ]
  recoil     = T
  isotropic = F
!
```
```
!
[ dust ]
  albedo          = 0.32
  g_dust          = 0.73
  dust_model     = SMC
!
```
```
!
[ uparallel ]
  method          = RASCAS
  xForGaussian   = 8.
!
```
```
!
[ voigt ]
  approximation = COLT
!
[ mock ]
  nDirections = 6
  mock_parameter_file = ./mockparams.cfg
  mock_outputfilename = Obelisk_test_ID
!
```

Appendix B - Galaxies characteristics

In the following tables I will present all of the values calculated for the galaxy sample, which
are the values that were used in the various color coded plots, first for the dust following
the metals and then for the simulation dust.

Sample	ID	L.O.S	Intrinsic $L_{Ly\alpha}$ [erg s^{-1}]	$L_{Ly\alpha}$ [erg s^{-1}]	Flux [erg s^{-1}cm^{-2}]	EW [Å]	$f_{esc}(Ly\alpha)$	$f_{esc}(LyC)$	V_{sep} [km s^{-1}]
A	14505		3.2×10^{44}	1.1×10^{43}	2.7×10^{-17}	9.3	0.03	0.013	
		1		1.4×10^{43}	3.4×10^{-17}	35.1	0.04	0.034	449.6
		2		2.1×10^{43}	5.0×10^{-17}	39.7	0.06	0.001	520.6
		3		4.2×10^{42}	1.0×10^{-17}	30.4	0.01	0.046	-
		4		9.4×10^{42}	2.3×10^{-17}	26.6	0.03	0.025	449.2
		5		1.5×10^{42}	3.5×10^{-18}	6.1	0.01	0.000	-
		6		1.5×10^{43}	3.6×10^{-17}	39.1	0.05	0.035	-
B	65038		1.7×10^{43}	2.8×10^{42}	6.8×10^{-18}	25.4	0.17	0.198	
		1		5.0×10^{42}	1.2×10^{-17}	26.6	0.30	0.245	305.8
		2		2.6×10^{42}	6.2×10^{-18}	17.6	0.16	0.353	256.6
		3		4.2×10^{42}	1.0×10^{-17}	21.1	0.26	0.127	256.2
		4		2.5×10^{42}	5.9×10^{-18}	59.2	0.15	0.003	295.9
		5		2.2×10^{42}	5.2×10^{-18}	20.2	0.13	0.073	266.3
		6		1.9×10^{42}	4.5×10^{-18}	130.3	0.11	0.005	226.8
	64846		5.2×10^{43}	4.9×10^{42}	1.2×10^{-17}	38.6	0.09	0.057	
		1		6.4×10^{42}	1.5×10^{-17}	32.7	0.12	0.105	187.5
		2		3.6×10^{42}	8.7×10^{-18}	34.2	0.07	0.001	197.1
		3		3.1×10^{42}	7.5×10^{-18}	118.5	0.06	0.017	255.9
		4		2.7×10^{42}	6.5×10^{-18}	171.1	0.05	0.001	286.4
		5		3.4×10^{42}	8.0×10^{-18}	21.8	0.06	0.050	296.1
		6		1.3×10^{43}	3.1×10^{-17}	64.2	0.25	0.193	0.0
C	2899		6.6×10^{43}	4.5×10^{42}	1.1×10^{-17}	62.0	0.07	0.001	
		1		5.2×10^{42}	1.2×10^{-17}	48.2	0.08	0.049	-
		2		3.0×10^{42}	7.2×10^{-18}	41.3	0.05	0.021	285.6
		3		4.7×10^{42}	1.1×10^{-17}	83.9	0.07	0.017	-
		4		2.1×10^{42}	5.2×10^{-18}	48.2	0.03	0.006	-
		5		6.6×10^{42}	1.6×10^{-17}	61.9	0.10	0.045	-
		6		4.2×10^{42}	1.0×10^{-17}	48.6	0.06	0.008	-
	24688		2.0×10^{44}	1.9×10^{42}	4.7×10^{-18}	25.8	0.01	0.004	
		1		1.6×10^{42}	3.9×10^{-18}	21.9	0.01	0.005	394.8
		2		1.6×10^{42}	3.7×10^{-18}	17.9	0.01	0.007	-

	3		$1.9{\times}10^{42}$	$4.5{\times}10^{-18}$	17.9	0.01	0.005	453.2
	4		$1.1{\times}10^{42}$	$2.7{\times}10^{-18}$	18.1	0.01	0.001	374.9
	5		$4.6{\times}10^{42}$	$1.1{\times}10^{-17}$	39.9	0.02	0.016	-
	6		$8.3{\times}10^{41}$	$2.0{\times}10^{-18}$	17.3	0.01	0.007	-
55468		$4.5{\times}10^{43}$	$1.5{\times}10^{42}$	$3.7{\times}10^{-18}$	32.9	0.03	0.002	
	1		$1.6{\times}10^{42}$	$3.8{\times}10^{-18}$	41.2	0.03	0.007	-
	2		$1.8{\times}10^{42}$	$4.3{\times}10^{-18}$	33.9	0.04	0.002	413.9
	3		$1.1{\times}10^{42}$	$2.7{\times}10^{-18}$	27.8	0.02	0.011	335.2
	4		$1.3{\times}10^{42}$	$3.0{\times}10^{-18}$	28.6	0.03	0.010	315.7
	5		$2.4{\times}10^{42}$	$5.7{\times}10^{-18}$	33.2	0.05	0.021	0.0
	6		$2.1{\times}10^{42}$	$4.9{\times}10^{-18}$	29.4	0.05	0.014	394.4
36112		$7.7{\times}10^{43}$	$3.8{\times}10^{42}$	$9.3{\times}10^{-18}$	42.4	0.05	0.007	
	1		$9.6{\times}10^{41}$	$2.3{\times}10^{-18}$	14.8	0.01	0.000	138.1
	2		$3.5{\times}10^{42}$	$8.4{\times}10^{-18}$	31.1	0.04	0.036	364.7
	3		$4.3{\times}10^{42}$	$1.0{\times}10^{-17}$	37.3	0.06	0.025	265.7
	4		$3.3{\times}10^{42}$	$7.9{\times}10^{-18}$	42.3	0.04	0.005	237.2
	5		$2.8{\times}10^{42}$	$6.7{\times}10^{-18}$	33.4	0.04	0.010	453.5
	6		$5.8{\times}10^{42}$	$1.4{\times}10^{-17}$	44.1	0.07	0.016	286.1
41163		$5.5{\times}10^{43}$	$1.6{\times}10^{42}$	$3.9{\times}10^{-18}$	46.0	0.03	0.007	
	1		$4.4{\times}10^{41}$	$1.0{\times}10^{-18}$	69.2	0.01	0.000	-
	2		$7.5{\times}10^{41}$	$1.8{\times}10^{-18}$	44.8	0.01	0.055	0.0
	3		$4.1{\times}10^{42}$	$9.9{\times}10^{-18}$	55.6	0.07	0.000	-
	4		$1.4{\times}10^{42}$	$3.4{\times}10^{-18}$	39.2	0.03	0.004	394.7
	5		$1.3{\times}10^{42}$	$3.2{\times}10^{-18}$	34.3	0.02	0.018	453.4
	6		$2.4{\times}10^{42}$	$5.7{\times}10^{-18}$	44.5	0.04	0.029	276.2
3639		$4.2{\times}10^{43}$	$8.4{\times}10^{41}$	$2.0{\times}10^{-18}$	30.3	0.02	0.001	
	1		$9.0{\times}10^{41}$	$2.2{\times}10^{-18}$	31.0	0.02	0.010	286.1
	2		$1.0{\times}10^{42}$	$2.5{\times}10^{-18}$	33.3	0.02	0.003	226.6
	3		$9.3{\times}10^{41}$	$2.2{\times}10^{-18}$	15.3	0.02	0.002	364.9
	4		$1.1{\times}10^{42}$	$2.6{\times}10^{-18}$	24.4	0.02	0.004	-
	5		$8.3{\times}10^{41}$	$2.0{\times}10^{-18}$	19.9	0.02	0.003	305.9
	6		$6.0{\times}10^{41}$	$1.4{\times}10^{-18}$	21.5	0.01	0.001	334.8
42655		$3.0{\times}10^{43}$	$2.1{\times}10^{42}$	$4.9{\times}10^{-18}$	50.3	0.07	0.024	

	1		5.0×10^{42}	1.2×10^{-17}	73.1	0.17	0.079	0.0
	2		5.1×10^{41}	1.2×10^{-18}	16.8	0.02	0.044	-
	3		2.4×10^{42}	5.7×10^{-18}	35.9	0.08	0.000	246.1
	4		1.2×10^{42}	2.9×10^{-18}	34.5	0.04	0.006	306.0
	5		1.8×10^{42}	4.3×10^{-18}	55.8	0.06	0.008	-
	6		1.8×10^{42}	4.2×10^{-18}	121.4	0.06	00115	266.1
8776		2.0×10^{43}	2.5×10^{42}	5.9×10^{-18}	39.3	0.12	0.026	
	1		3.8×10^{42}	9.1×10^{-18}	88.0	0.19	0.024	-
	2		1.3×10^{42}	3.1×10^{-18}	60.9	0.07	0.010	305.4
	3		2.5×10^{42}	6.1×10^{-18}	53.9	0.13	0.001	355.0
	4		8.7×10^{41}	2.1×10^{-18}	35.3	0.04	0.003	286.0
	5		5.4×10^{42}	1.3×10^{-17}	59.1	0.27	0.069	246.6
	6		8.2×10^{41}	2.0×10^{-18}	34.6	0.04	0.002	345.3
39021		4.0×10^{43}	2.9×10^{42}	7.0×10^{-18}	41.6	0.07	0.033	
	1		3.1×10^{42}	7.5×10^{-18}	127.7	0.08	0.008	295.8
	2		3.0×10^{42}	7.3×10^{-18}	93.4	0.07	0.039	275.9
	3		3.5×10^{42}	8.5×10^{-18}	26.7	0.09	0.034	364.3
	4		4.1×10^{42}	9.9×10^{-18}	27.0	0.10	0.081	266.6
	5		2.6×10^{42}	6.3×10^{-18}	105.4	0.06	0.019	275.8
	6		2.1×10^{42}	5.1×10^{-18}	111.1	0.05	0.002	355.2
76168		3.6×10^{43}	2.6×10^{42}	6.3×10^{-18}	56.6	0.07	0.011	
	1		3.1×10^{42}	7.4×10^{-18}	83.2	0.08	0.000	256.2
	2		2.1×10^{42}	5.0×10^{-18}	143.4	0.06	0.005	295.6
	3		1.6×10^{42}	3.7×10^{-18}	40.7	0.04	0.001	256.1
	4		2.9×10^{42}	6.9×10^{-18}	36.7	0.08	0.020	365.3
	5		4.5×10^{42}	1.1×10^{-17}	127.9	0.12	0.024	395.2
	6		8.1×10^{41}	2.0×10^{-18}	37.1	0.02	0.002	-
10345		1.3×10^{43}	3.2×10^{42}	7.8×10^{-18}	59.1	0.26	0.236	
	1		2.3×10^{42}	5.6×10^{-18}	93.2	0.19	0.005	256.4
	2		2.8×10^{42}	6.8×10^{-18}	45.3	0.22	0.468	157.8
	3		5.7×10^{42}	1.4×10^{-17}	64.2	0.45	0.070	128.1
	4		1.9×10^{42}	4.5×10^{-18}	87.7	0.14	0.005	246.7
	5		3.1×10^{42}	7.4×10^{-18}	37.1	0.24	0.521	207.0

	6		2.4×10^{42}	5.8×10^{-18}	108.7	0.19	0.027	236.8
57172		7.4×10^{42}	3.9×10^{42}	9.5×10^{-18}	42.4	0.53	0.485	
	1		3.1×10^{42}	7.3×10^{-18}	58.8	0.41	0.106	177.5
	2		4.9×10^{42}	1.2×10^{-17}	41.5	0.65	0.290	157.8
	3		3.7×10^{42}	9.0×10^{-18}	61.8	0.50	0.781	177.6
	4		1.9×10^{42}	4.5×10^{-18}	48.3	0.25	0.010	197.2
	5		4.0×10^{42}	9.7×10^{-18}	34.3	0.54	0.687	157.9
	6		3.4×10^{42}	8.2×10^{-18}	29.8	0.45	0.762	0.0
67244		1.1×10^{43}	5.0×10^{42}	1.2×10^{-17}	108.8	0.43	0.196	
	1		1.9×10^{42}	4.5×10^{-18}	197.2	0.16	0.002	187.5
	2		5.7×10^{42}	1.4×10^{-17}	115.0	0.50	0.119	226.7
	3		6.0×10^{42}	1.4×10^{-17}	87.5	0.52	0.330	256.1
	4		6.2×10^{42}	1.5×10^{-17}	188.8	0.54	0.109	207.4
	5		5.7×10^{42}	1.4×10^{-17}	81.9	0.49	0.471	246.2
	6		5.6×10^{42}	1.3×10^{-17}	123.4	0.49	0.145	236.9

Table 5.1: Values used in this work, for each galaxy and per line of sight (L.O.S). The peak separations marked with - are those that have been removed from the analysis due to being unclear.

Sample	ID	L.O.S	Intrinsic $L_{Ly\alpha}$ [erg s^{-1}]	$L_{Ly\alpha}$ [erg s^{-1}]	Flux [erg s^{-1}cm^{-2}]	EW [Å]	$f_{esc}(Ly\alpha)$	$f_{esc}(LyC)$	V_{sep} [km s^{-1}]
A	14505		3.2×10^{44}	1.2×10^{43}	2.9×10^{-17}	7.1	0.04	0.013	
		1		1.6×10^{43}	3.7×10^{-17}	26.5	0.05	0.034	402.3
		2		2.2×10^{43}	5.3×10^{-17}	31.5	0.07	0.001	378.4
		3		4.2×10^{42}	1.0×10^{-17}	13.5	0.01	0.046	-
		4		8.5×10^{42}	2.0×10^{-17}	23.5	0.03	0.025	520.2
		5		1.8×10^{42}	4.3×10^{-18}	5.0	0.01	0.000	-
		6		1.5×10^{43}	3.6×10^{-17}	29.5	0.05	0.035	-
B	65038		1.7×10^{43}	1.8×10^{42}	4.3×10^{-18}	17.7	0.11	0.198	
		1		2.8×10^{42}	6.7×10^{-18}	25.2	0.17	0.245	305.8
		2		1.9×10^{42}	4.6×10^{-18}	16.0	0.11	0.353	335.6
		3		2.4×10^{42}	5.8×10^{-18}	13.6	0.14	0.127	266.0
		4		1.7×10^{42}	4.0×10^{-18}	51.7	0.10	0.003	286.1
		5		1.4×10^{42}	3.3×10^{-18}	16.9	0.08	0.073	276.1
		6		1.3×10^{42}	3.0×10^{-18}	21.2	0.08	0.005	226.8
	64846		5.2×10^{43}	2.9×10^{42}	7.1×10^{-18}	22.9	0.06	0.057	
		1		3.8×10^{42}	9.1×10^{-18}	22.9	0.07	0.105	187.5
		2		2.1×10^{42}	5.0×10^{-18}	16.5	0.04	0.001	207.0
		3		1.8×10^{42}	4.4×10^{-18}	42.4	0.03	0.017	246.1
		4		1.7×10^{42}	4.0×10^{-18}	60.1	0.03	0.001	296.3
		5		2.3×10^{42}	5.6×10^{-18}	13.9	0.04	0.050	296.1
		6		6.5×10^{42}	1.5×10^{-17}	37.5	0.13	0.193	0.0
C	2899		6.6×10^{43}	4.0×10^{42}	9.8×10^{-18}	31.6	0.06	0.001	
		1		4.9×10^{42}	1.2×10^{-17}	28.6	0.07	0.049	-
		2		2.3×10^{42}	5.5×10^{-18}	20.0	0.03	0.021	-
		3		4.7×10^{42}	1.1×10^{-17}	38.4	0.07	0.017	-
		4		1.9×10^{42}	4.5×10^{-18}	14.6	0.03	0.006	-
		5		5.2×10^{42}	1.2×10^{-17}	29.8	0.08	0.045	522.1
		6		4.2×10^{42}	1.0×10^{-17}	23.7	0.06	0.008	830.2
	24688		2.0×10^{44}	2.0×10^{42}	4.9×10^{-18}	18.1	0.01	0.004	
		1		1.9×10^{42}	4.5×10^{-18}	17.5	0.01	0.005	-
		2		1.7×10^{42}	4.0×10^{-18}	15.4	0.01	0.007	462.8

	3		1.8×10^{42}	4.3×10^{-18}	13.4	0.01	0.005	542.0
	4		1.6×10^{42}	3.9×10^{-18}	16.1	0.01	0.001	434.2
	5		4.7×10^{42}	1.1×10^{-17}	30.1	0.02	0.016	394.7
	6		1.0×10^{42}	2.5×10^{-18}	9.4	0.01	0.007	-
55468		4.5×10^{43}	1.4×10^{42}	3.5×10^{-18}	19.0	0.03	0.002	
	1		1.7×10^{42}	4.2×10^{-18}	30.4	0.04	0.007	-
	2		1.4×10^{42}	3.3×10^{-18}	27.7	0.03	0.002	354.7
	3		9.6×10^{41}	2.3×10^{-18}	10.9	0.02	0.011	345.0
	4		1.6×10^{42}	3.8×10^{-18}	17.6	0.03	0.010	355.2
	5		2.1×10^{42}	5.1×10^{-18}	18.9	0.05	0.021	473.7
	6		2.2×10^{42}	5.1×10^{-18}	18.5	0.05	0.014	384.6
36112		7.7×10^{43}	2.4×10^{42}	5.9×10^{-18}	23.6	0.03	0.007	
	1		7.3×10^{41}	1.8×10^{-18}	8.2	0.01	0.000	-
	2		2.2×10^{42}	5.4×10^{-18}	16.3	0.03	0.036	345.0
	3		2.7×10^{42}	6.4×10^{-18}	25.0	0.03	0.025	0.0
	4		1.8×10^{42}	4.2×10^{-18}	27.1	0.02	0.005	217.4
	5		2.0×10^{42}	4.9×10^{-18}	19.5	0.03	0.010	-
	6		3.8×10^{42}	9.0×10^{-18}	23.1	0.05	0.016	345.2
41163		5.5×10^{43}	1.3×10^{42}	3.1×10^{-18}	26.4	0.02	0.007	
	1		3.3×10^{41}	7.9×10^{-18}	16.5	0.01	0.000	374.7
	2		6.1×10^{41}	1.5×10^{-18}	15.4	0.01	0.055	217.0
	3		3.1×10^{42}	7.3×10^{-18}	35.3	0.06	0.000	-
	4		9.0×10^{41}	2.1×10^{-18}	17.5	0.02	0.004	384.9
	5		1.3×10^{42}	3.0×10^{-18}	23.1	0.02	0.018	463.2
	6		1.8×10^{42}	4.2×10^{-18}	29.2	0.03	0.029	276.2
3639		4.2×10^{43}	9.5×10^{41}	2.3×10^{-18}	19.7	0.02	0.001	
	1		9.8×10^{41}	2.3×10^{-18}	21.2	0.02	0.010	286.1
	2		1.2×10^{42}	3.0×10^{-18}	27.6	0.03	0.003	236.4
	3		1.0×10^{42}	2.4×10^{-18}	15.4	0.02	0.002	355.0
	4		1.2×10^{42}	3.0×10^{-18}	21.9	0.03	0.004	-
	5		8.2×10^{41}	2.0×10^{-18}	13.5	0.02	0.003	394.7
	6		6.5×10^{41}	1.6×10^{-18}	13.2	0.01	0.001	334.8
42655		3.0×10^{43}	1.9×10^{42}	4.5×10^{-18}	30.6	0.06	0.024	

	1		4.1×10^{42}	9.8×10^{-18}	44.6	0.13	0.079	375.2
	2		5.6×10^{41}	1.3×10^{-18}	10.5	0.02	0.044	345.1
	3		2.0×10^{42}	4.7×10^{-18}	32.9	0.06	0.000	246.1
	4		1.3×10^{42}	3.1×10^{-18}	20.2	0.04	0.006	355.6
	5		1.5×10^{42}	3.7×10^{-18}	34.4	0.05	0.008	-
	6		1.8×10^{42}	4.2×10^{-18}	28.9	0.06	00115	266.1
8776		2.0×10^{43}	1.8×10^{42}	4.4×10^{-18}	21.9	0.09	0.026	
	1		2.7×10^{42}	6.4×10^{-18}	40.8	0.13	0.024	-
	2		9.8×10^{41}	2.4×10^{-18}	16.8	0.05	0.010	305.4
	3		1.9×10^{42}	4.6×10^{-18}	28.7	0.10	0.001	364.8
	4		7.4×10^{41}	1.8×10^{-18}	10.5	0.04	0.003	295.8
	5		3.6×10^{42}	8.5×10^{-17}	32.6	0.18	0.069	296.0
	6		8.1×10^{41}	2.0×10^{-18}	15.4	0.04	0.002	365.0
39021		4.0×10^{43}	1.9×10^{42}	4.6×10^{-18}	31.6	0.05	0.033	
	1		2.5×10^{42}	6.1×10^{-18}	80.2	0.06	0.008	315.6
	2		2.5×10^{42}	6.0×10^{-18}	63.4	0.06	0.039	286.3
	3		2.1×10^{42}	5.1×10^{-18}	19.3	0.05	0.034	344.6
	4		1.8×10^{42}	4.3×10^{-18}	19.0	0.04	0.081	227.1
	5		2.0×10^{42}	4.8×10^{-18}	60.7	0.05	0.019	265.9
	6		1.4×10^{42}	3.3×10^{-18}	57.7	0.03	0.002	177.6
76168		3.6×10^{43}	2.1×10^{42}	5.0×10^{-18}	29.3	0.06	0.011	
	1		2.2×10^{42}	5.4×10^{-18}	16.7	0.06	0.000	256.5
	2		1.7×10^{42}	4.1×10^{-18}	39.3	0.05	0.005	315.3
	3		1.5×10^{42}	3.5×10^{-18}	21.0	0.04	0.001	197.0
	4		1.9×10^{42}	4.5×10^{-18}	26.2	0.05	0.020	315.9
	5		3.7×10^{42}	8.8×10^{-18}	51.4	0.10	0.024	405.1
	6		9.0×10^{41}	2.2×10^{-18}	24.6	0.02	0.002	-
10345		1.3×10^{43}	1.9×10^{42}	4.5×10^{-18}	35.5	0.15	0.236	
	1		1.4×10^{42}	3.3×10^{-18}	42.9	0.11	0.005	266.2
	2		1.4×10^{42}	3.4×10^{-18}	31.6	0.11	0.468	157.7
	3		3.2×10^{42}	7.6×10^{-18}	37.9	0.25	0.070	137.9
	4		1.1×10^{42}	2.6×10^{-18}	25.3	0.08	0.005	236.9
	5		2.1×10^{42}	5.0×10^{-18}	25.3	0.16	0.521	216.8

	6		1.4×10^{42}	3.4×10^{-18}	44.4	0.11	0.027	227.0
57172		7.4×10^{42}	2.3×10^{42}	5.5×10^{-18}	28.4	0.31	0.485	
	1		1.8×10^{42}	7.3×10^{-18}	42.4	0.24	0.106	157.8
	2		2.7×10^{42}	4.4×10^{-18}	24.5	0.36	0.290	157.8
	3		2.2×10^{42}	5.2×10^{-18}	39.9	0.29	0.781	148.0
	4		1.1×10^{42}	2.6×10^{-18}	17.4	0.15	0.010	177.5
	5		2.4×10^{42}	5.9×10^{-18}	21.8	0.33	0.687	157.9
	6		2.0×10^{42}	4.8×10^{-18}	18.7	0.27	0.762	0.0
67244		1.1×10^{43}	3.8×10^{42}	9.2×10^{-18}	69.5	0.34	0.196	
	1		1.4×10^{42}	3.5×10^{-18}	37.9	0.13	0.002	187.5
	2		4.7×10^{42}	1.1×10^{-17}	81.5	0.41	0.119	236.6
	3		4.6×10^{42}	1.1×10^{-17}	68.0	0.40	0.330	256.0
	4		4.7×10^{42}	1.1×10^{-17}	101.5	0.41	0.109	197.6
	5		4.6×10^{42}	1.1×10^{-17}	64.3	0.41	0.471	246.2
	6		4.5×10^{42}	1.1×10^{-17}	80.8	0.39	0.145	227.1

Table 5.2: Values used in this work, for each galaxy and per line of sight (L.O.S). The peak separations marked with - are those that have been removed from the analysis due to being unclear.

Appendix C - Spectra

The following figures are showing all of the total spectra, so recombination plus collisions, of the galaxies of the sample, both for the metal dust model and the simulation dust model, respectively represented in blue and orange.
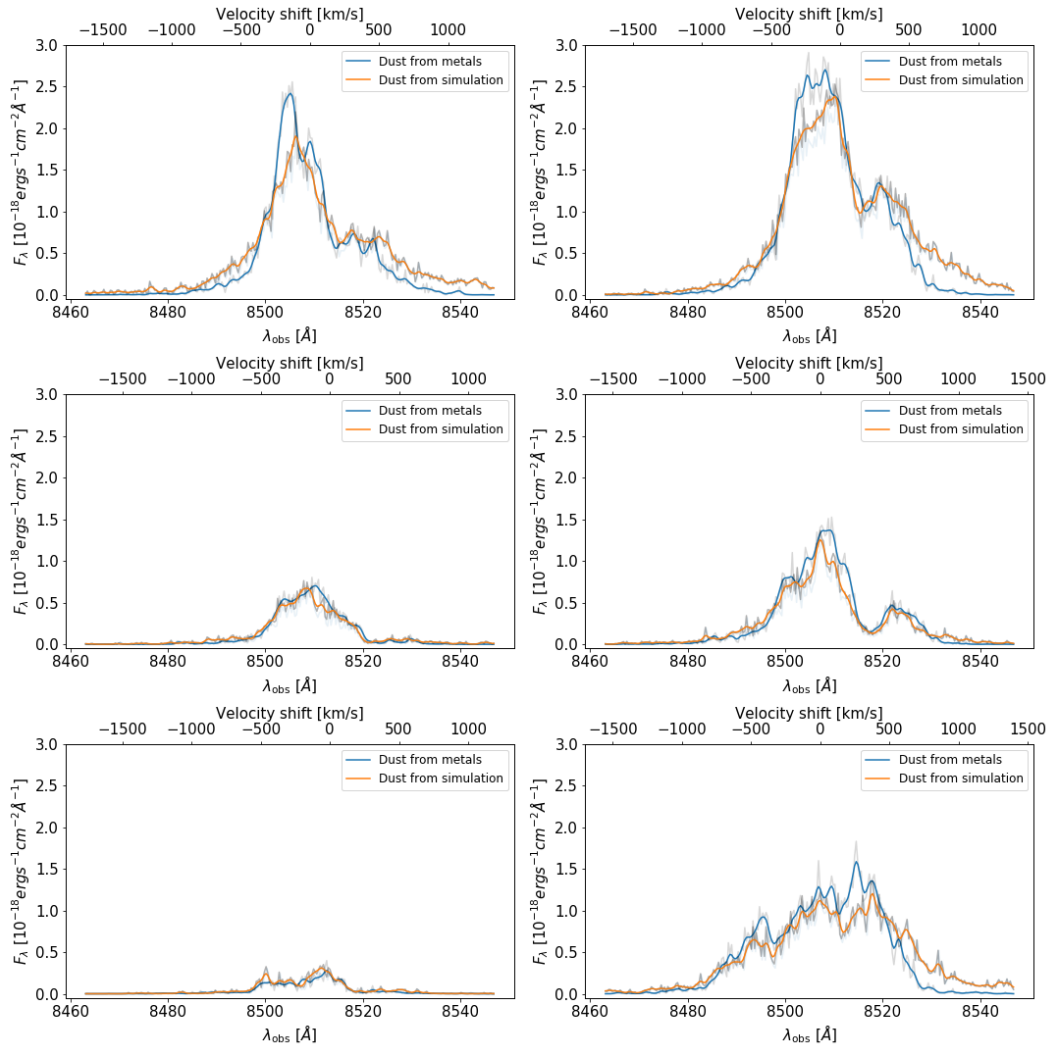
Figure 5.1: Galaxy ID 14505 (sample A)
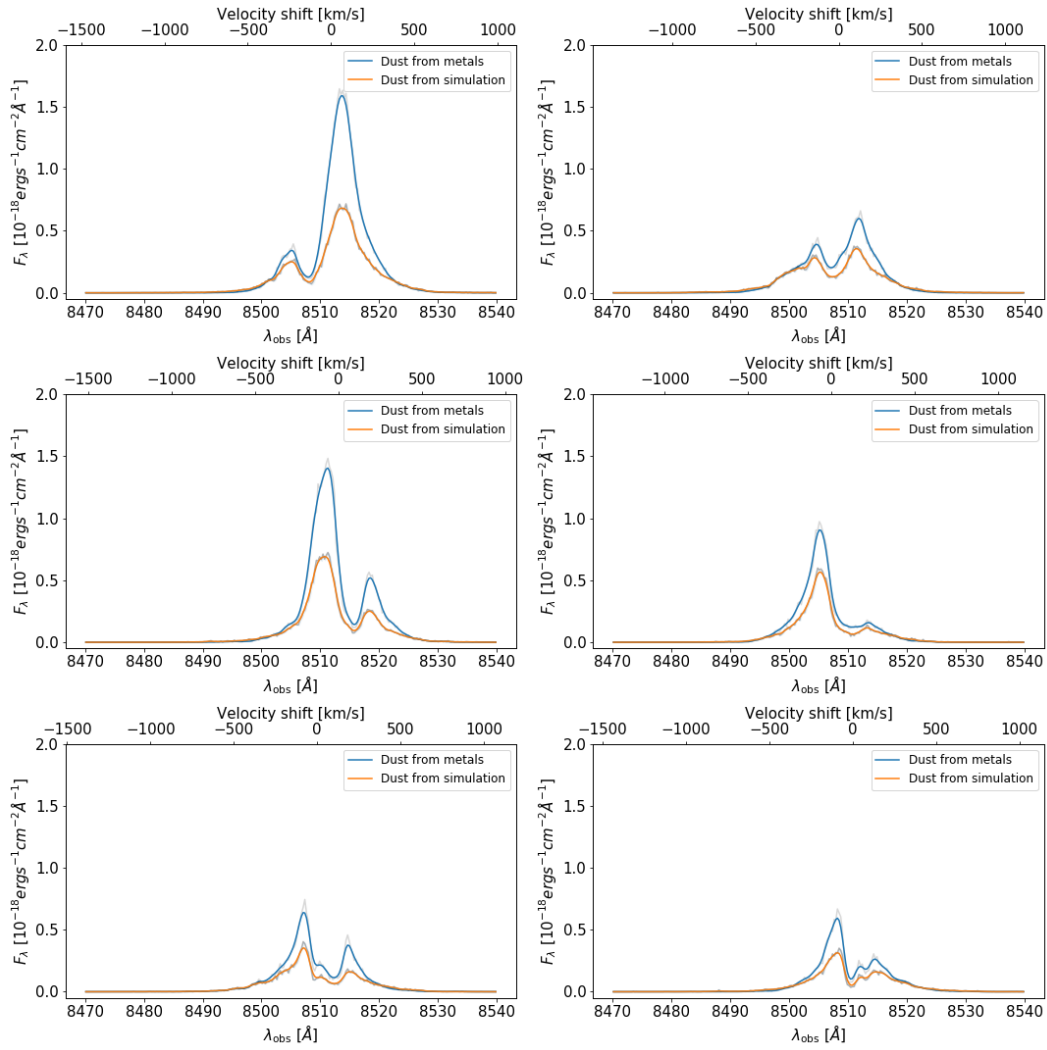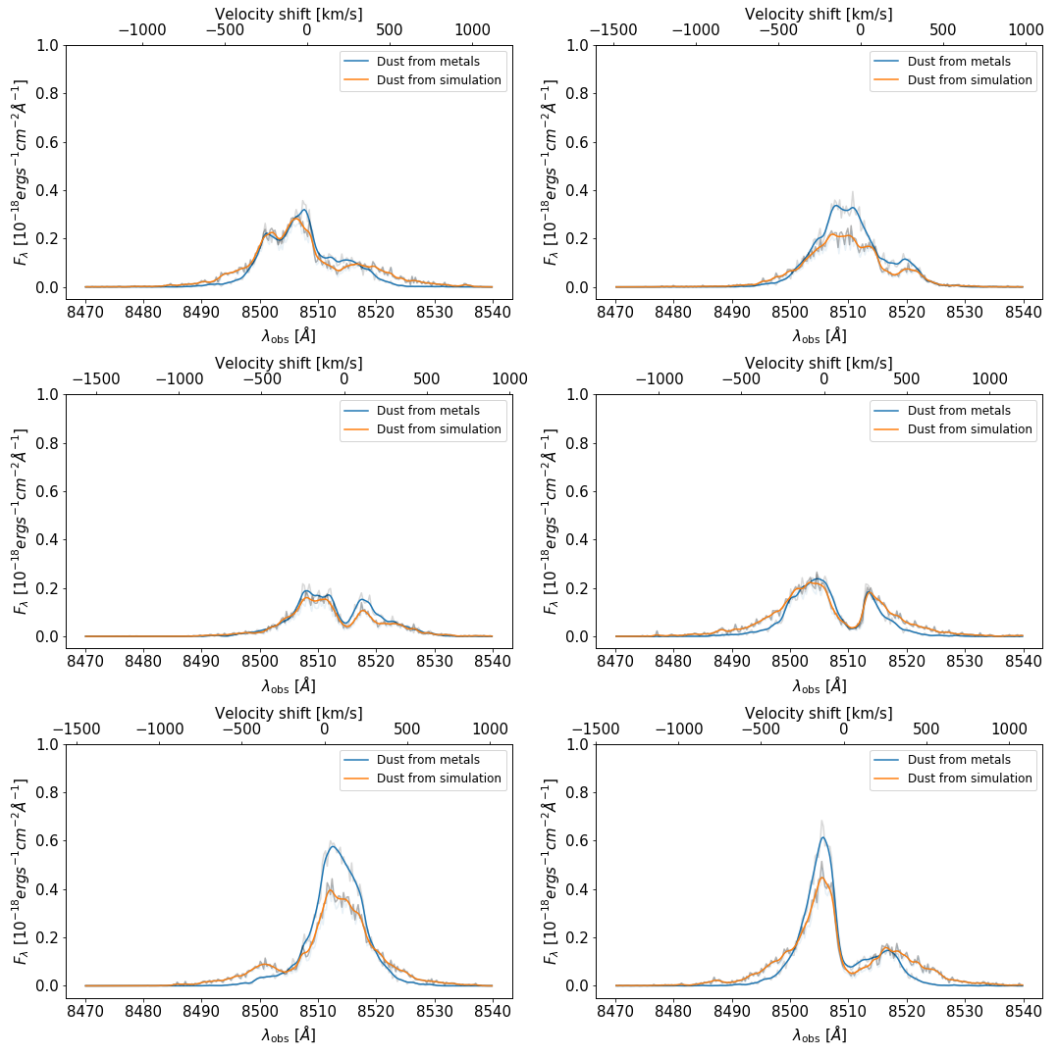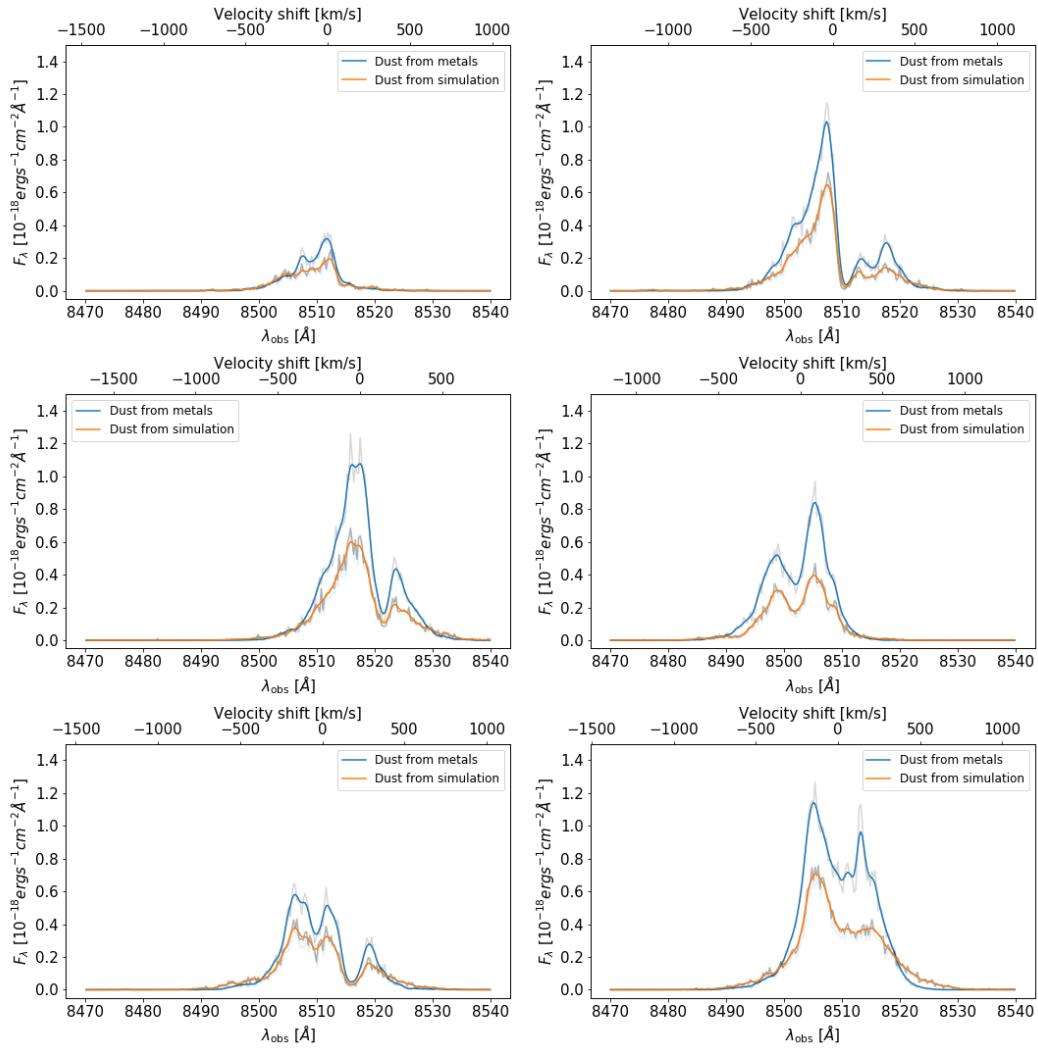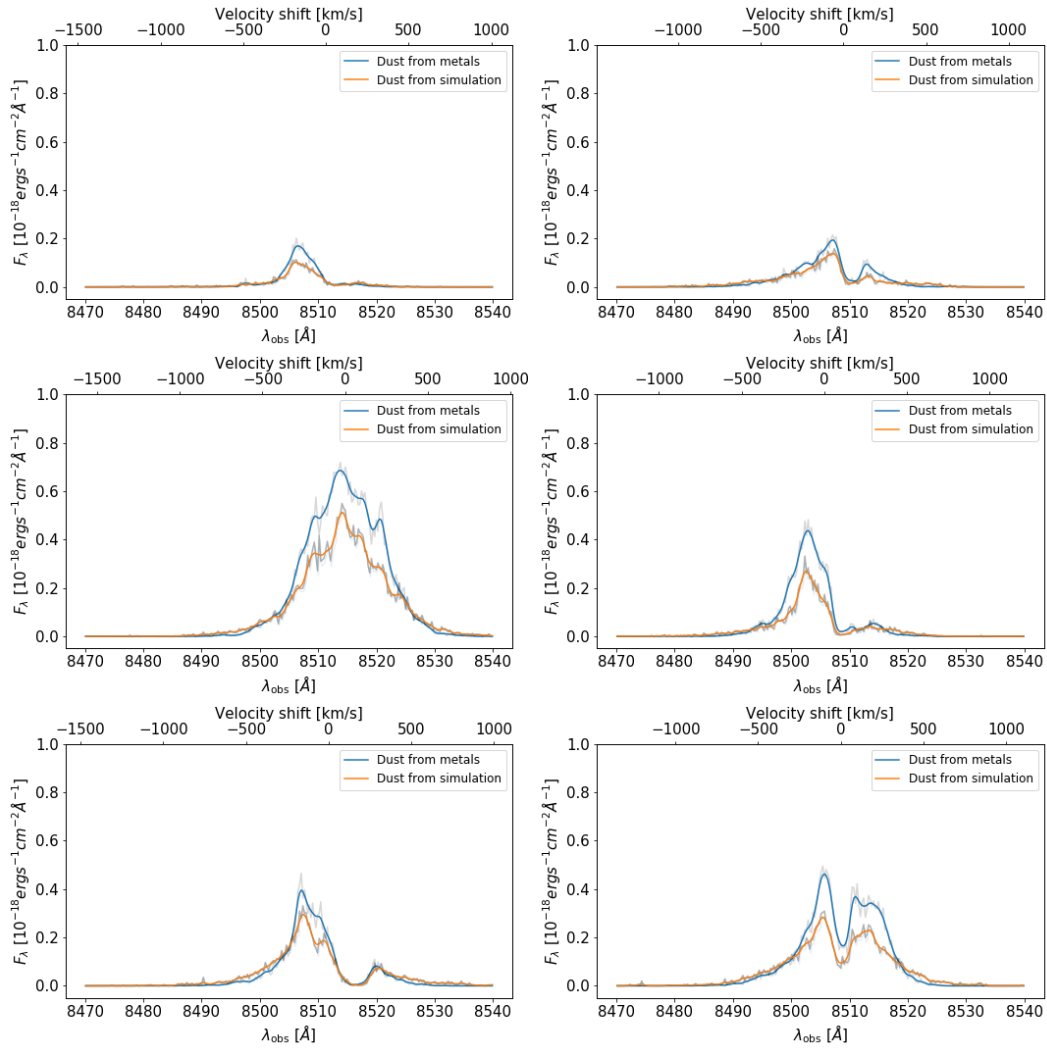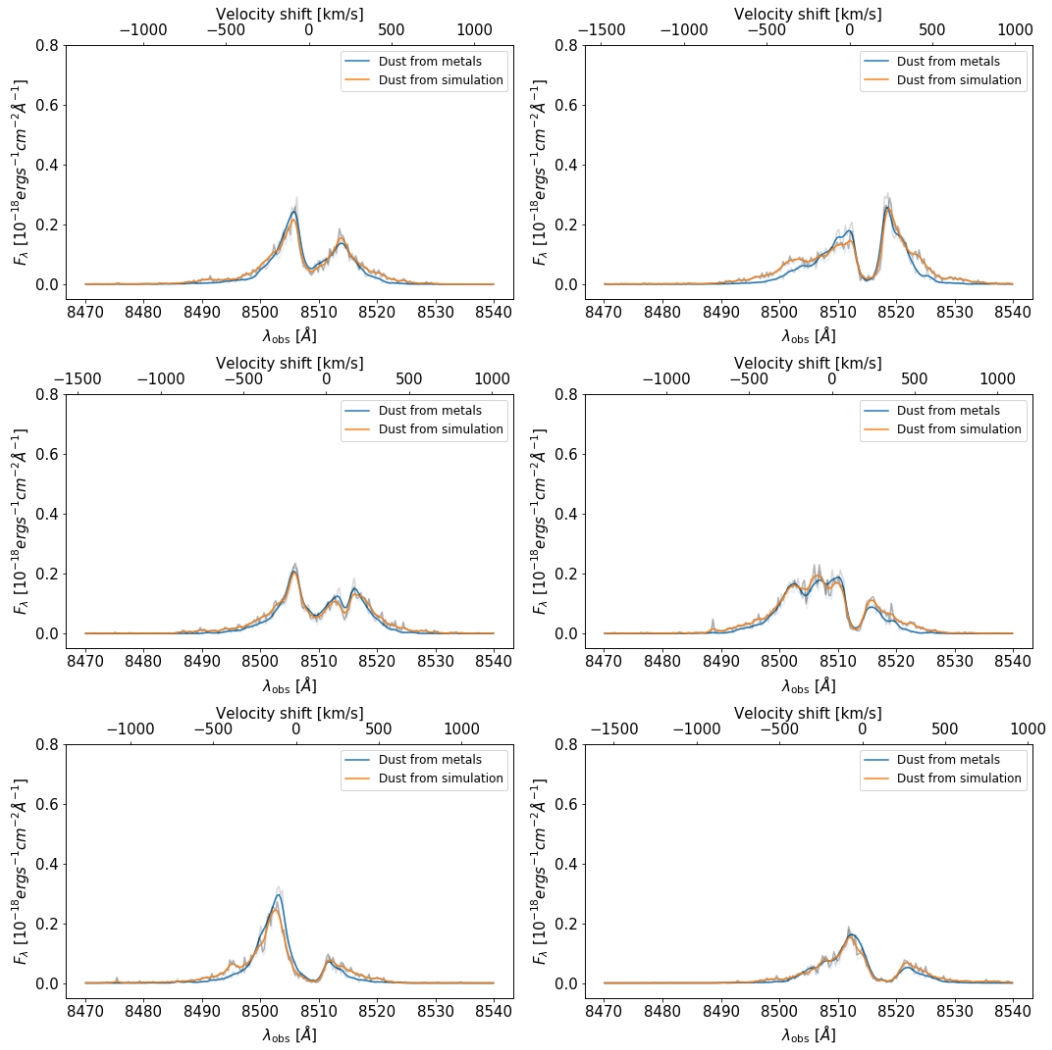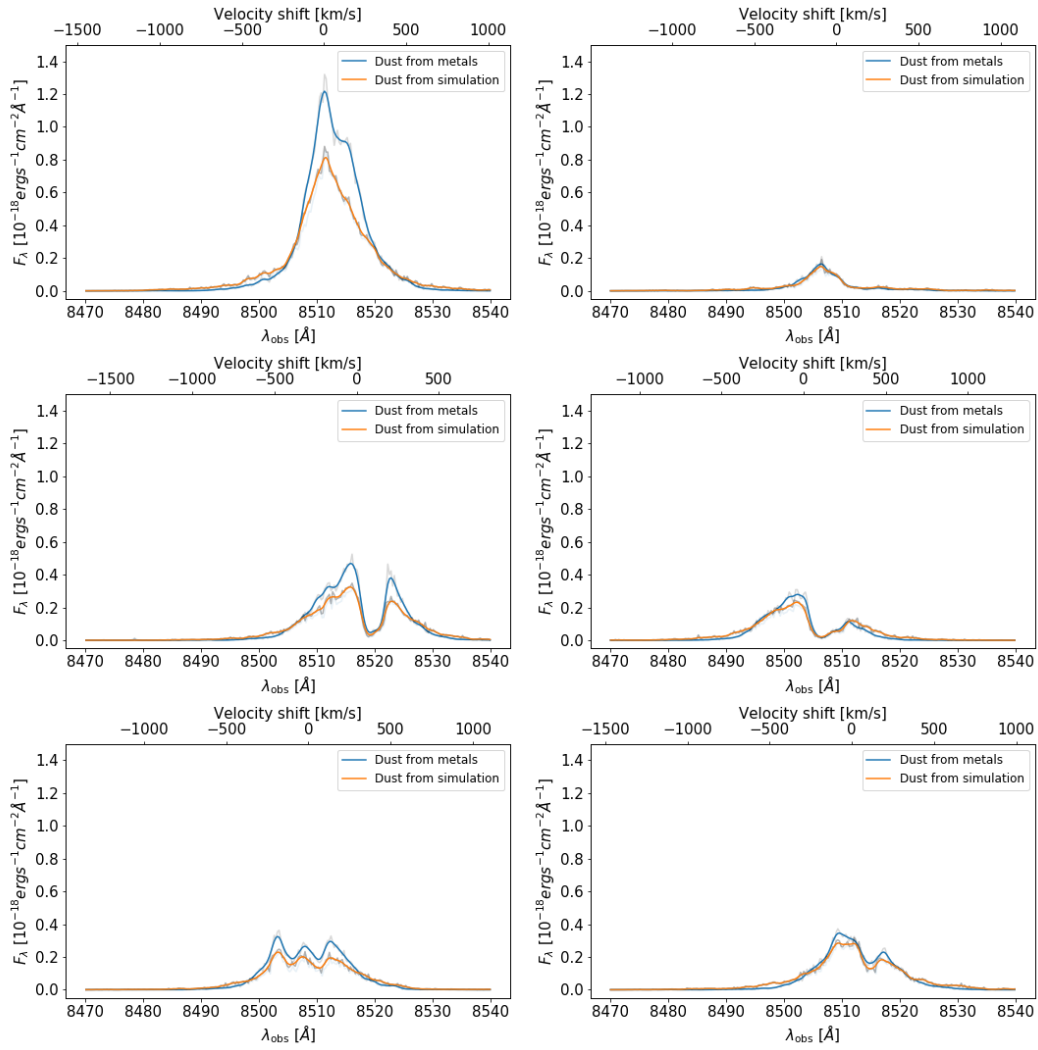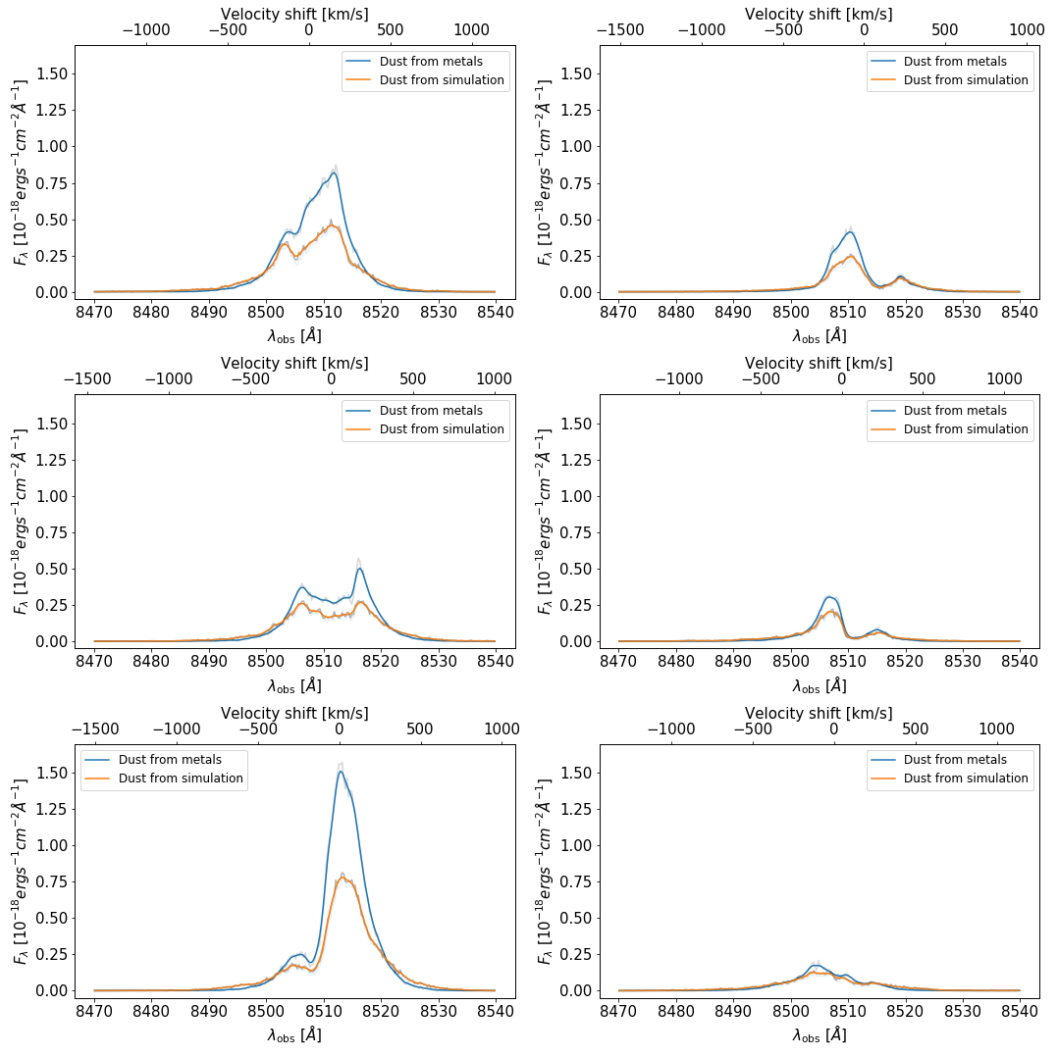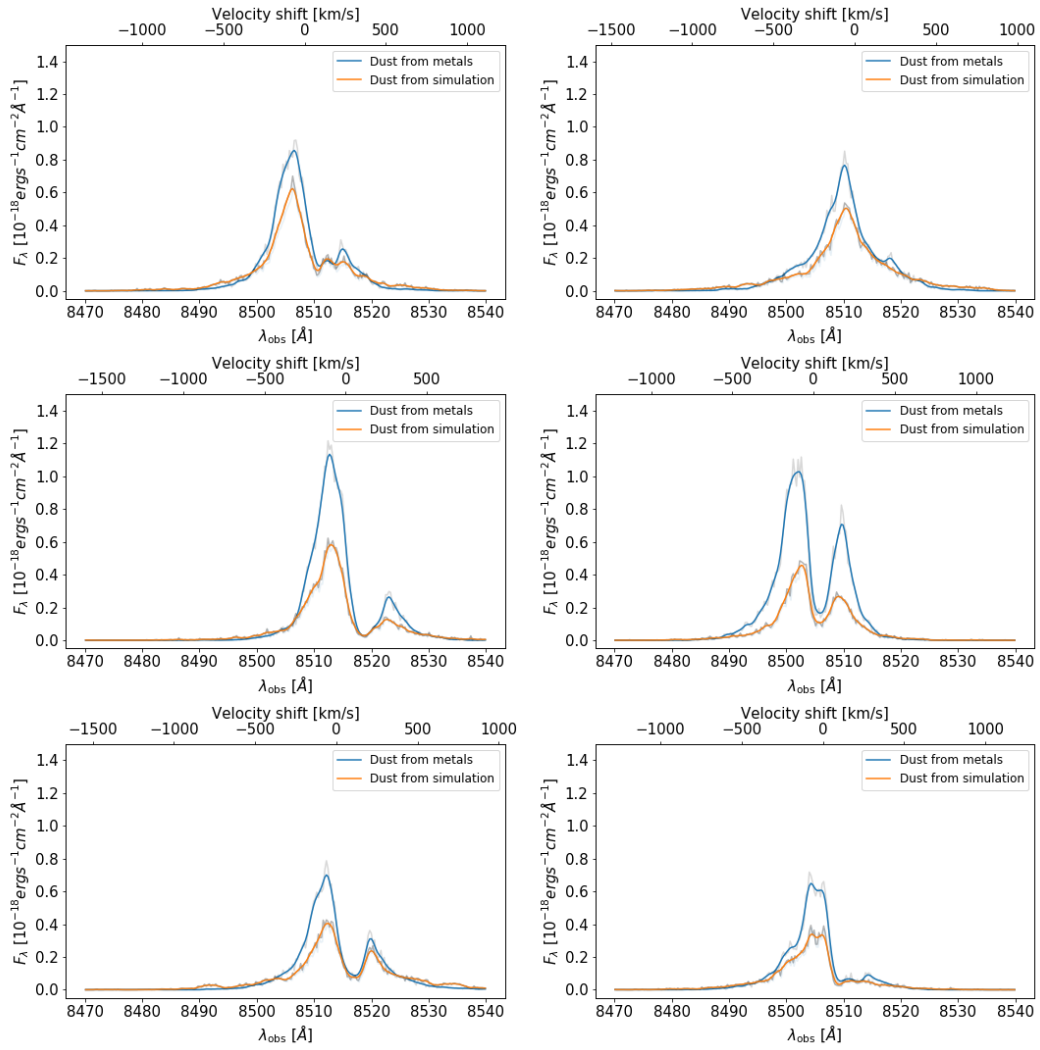
Figure 5.2: Galaxy ID 65038 (sample B)
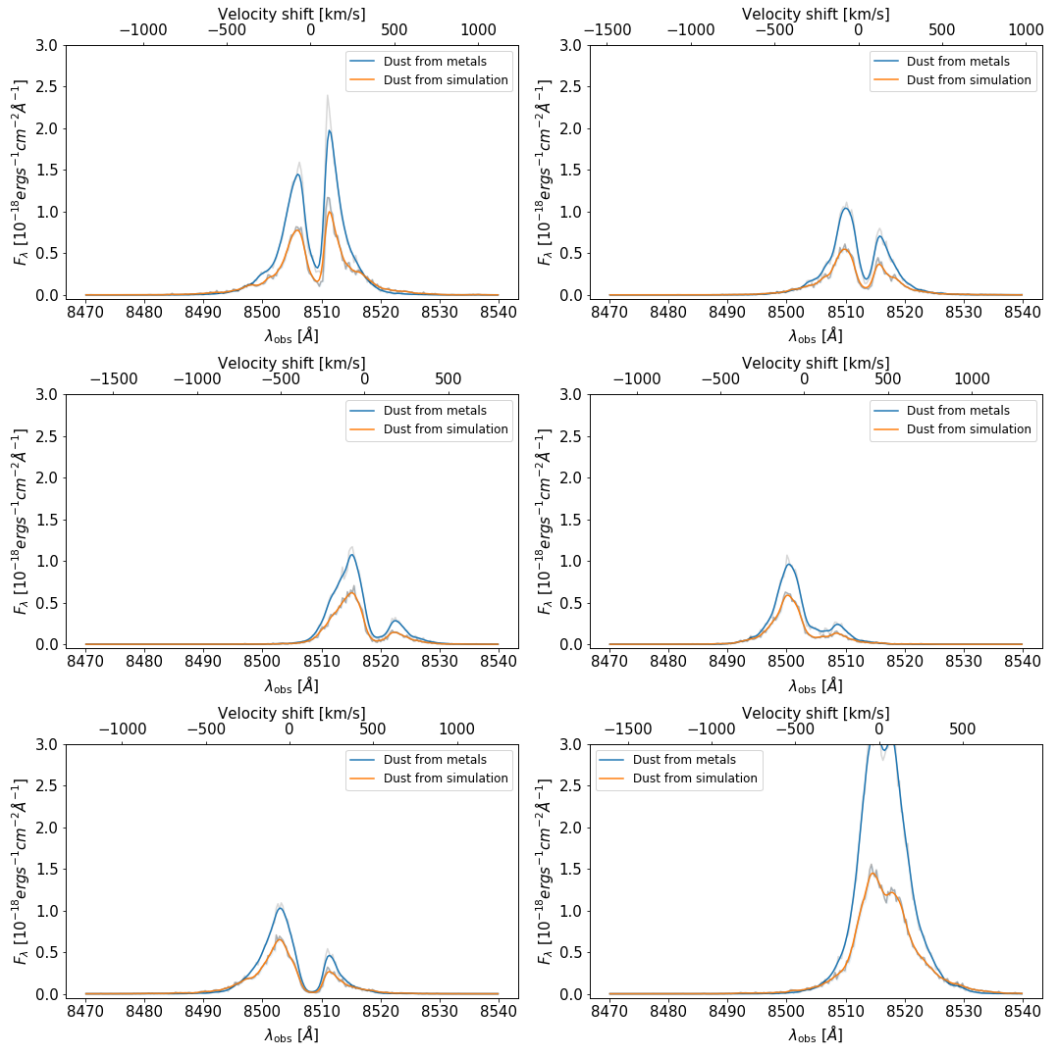
Figure 5.3: Galaxy ID 64846 (sample B)
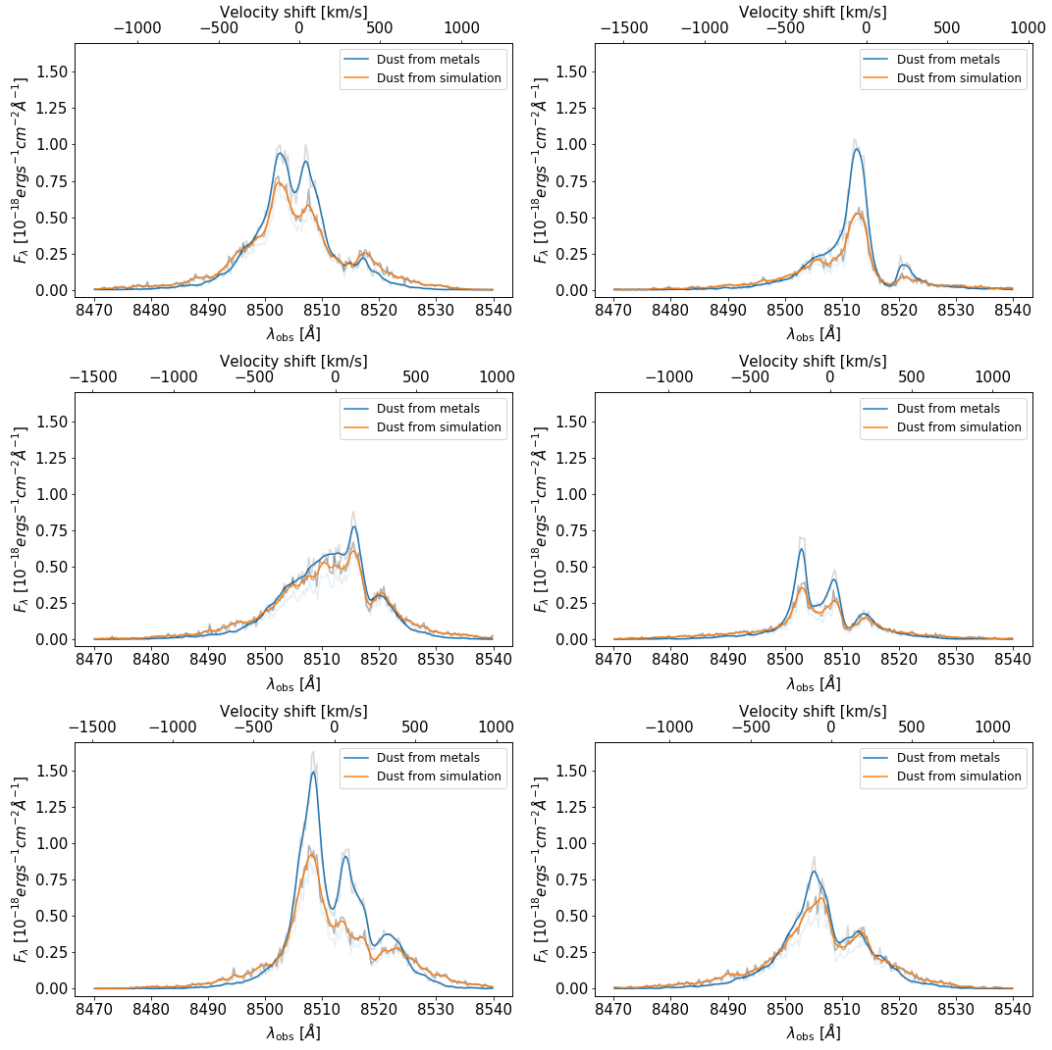
Figure 5.4: Galaxy ID 2899 (sample C)
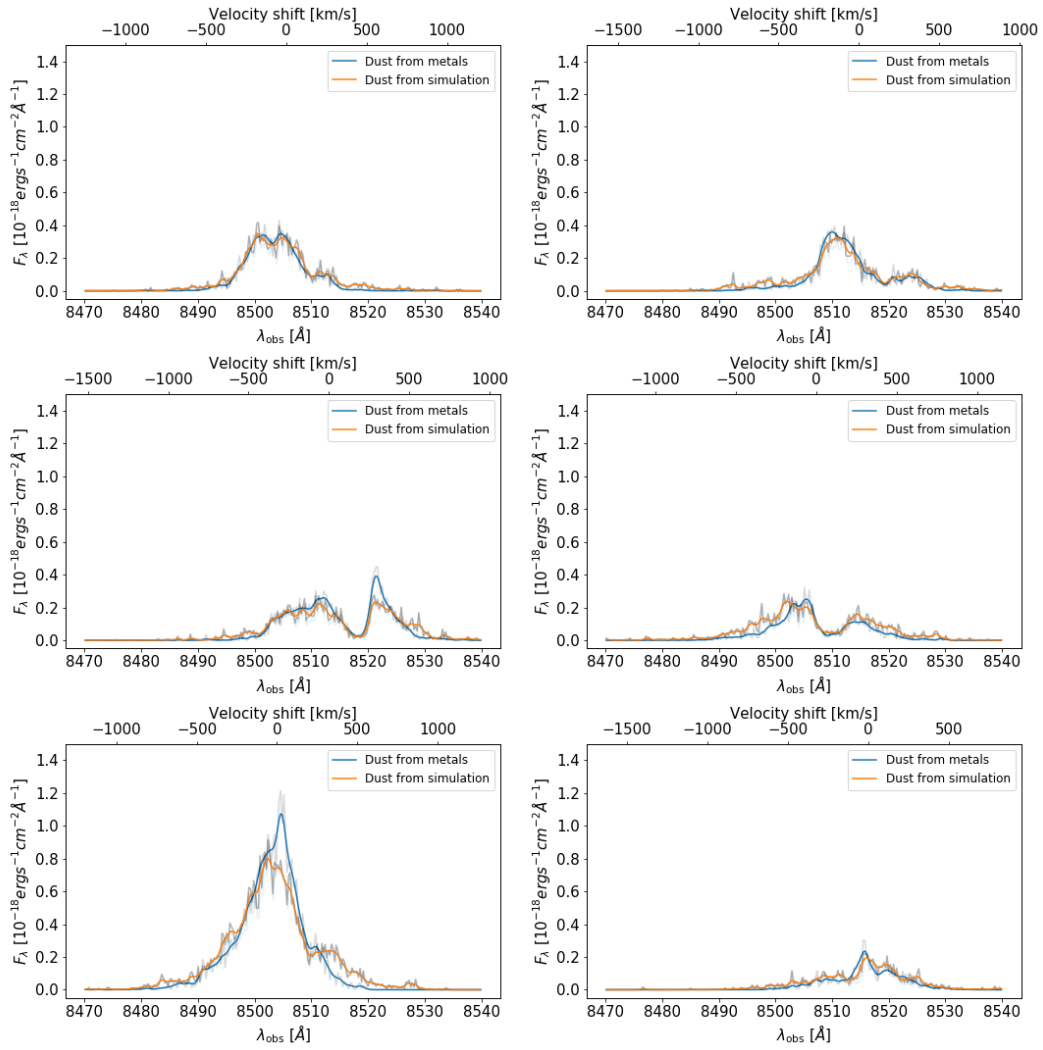
Figure 5.5: Galaxy ID 24688 (sample C)

Figure 5.6: Galaxy ID 55468 (sample C)

Figure 5.7: Galaxy ID 36112 (sample C)

Figure 5.8: Galaxy ID 41163 (sample C)

Figure 5.9: Galaxy ID 3639 (sample C)

Figure 5.10: Galaxy ID 42655 (sample C)

Figure 5.11: Galaxy ID 8776 (sample C)

Figure 5.12: Galaxy ID 39021 (sample C)
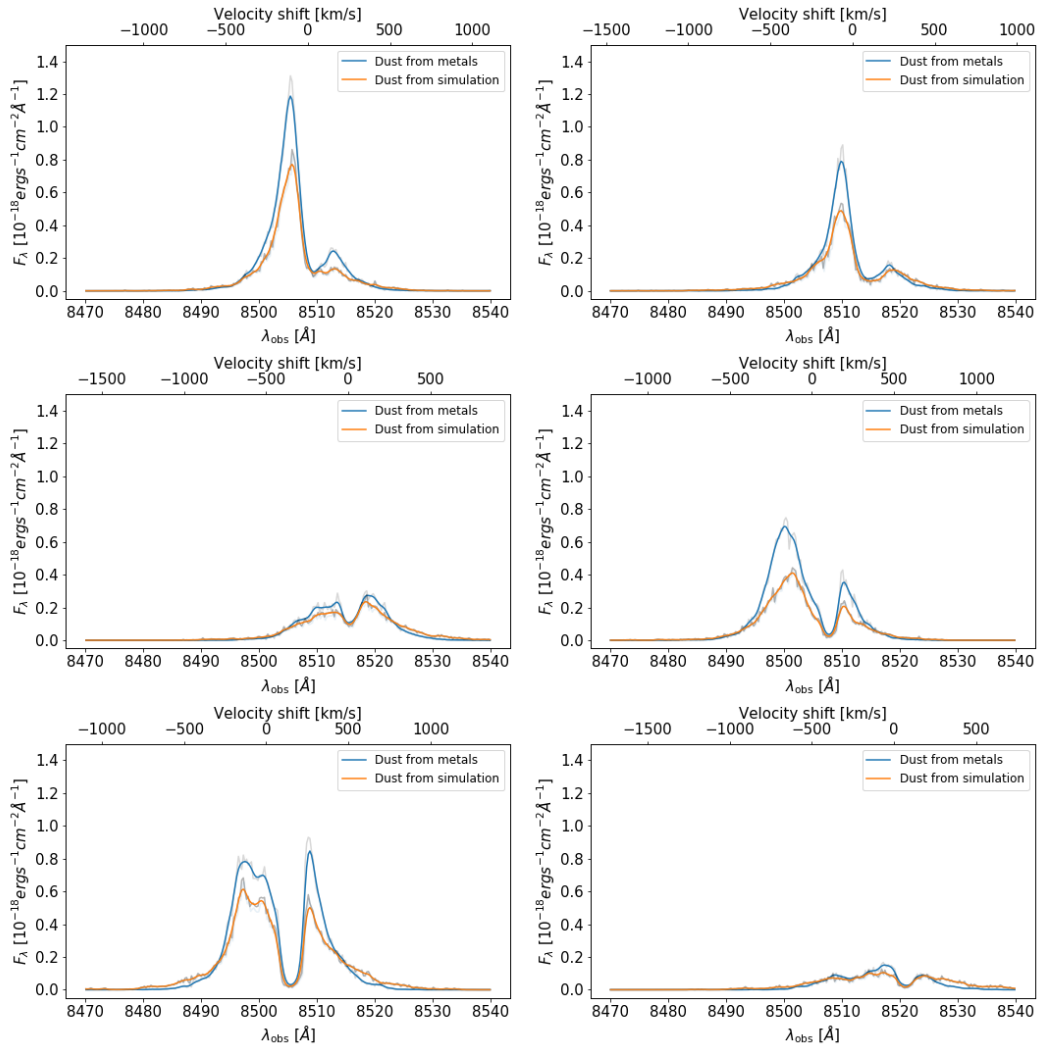
Figure 5.13: Galaxy ID 76168 (sample C)
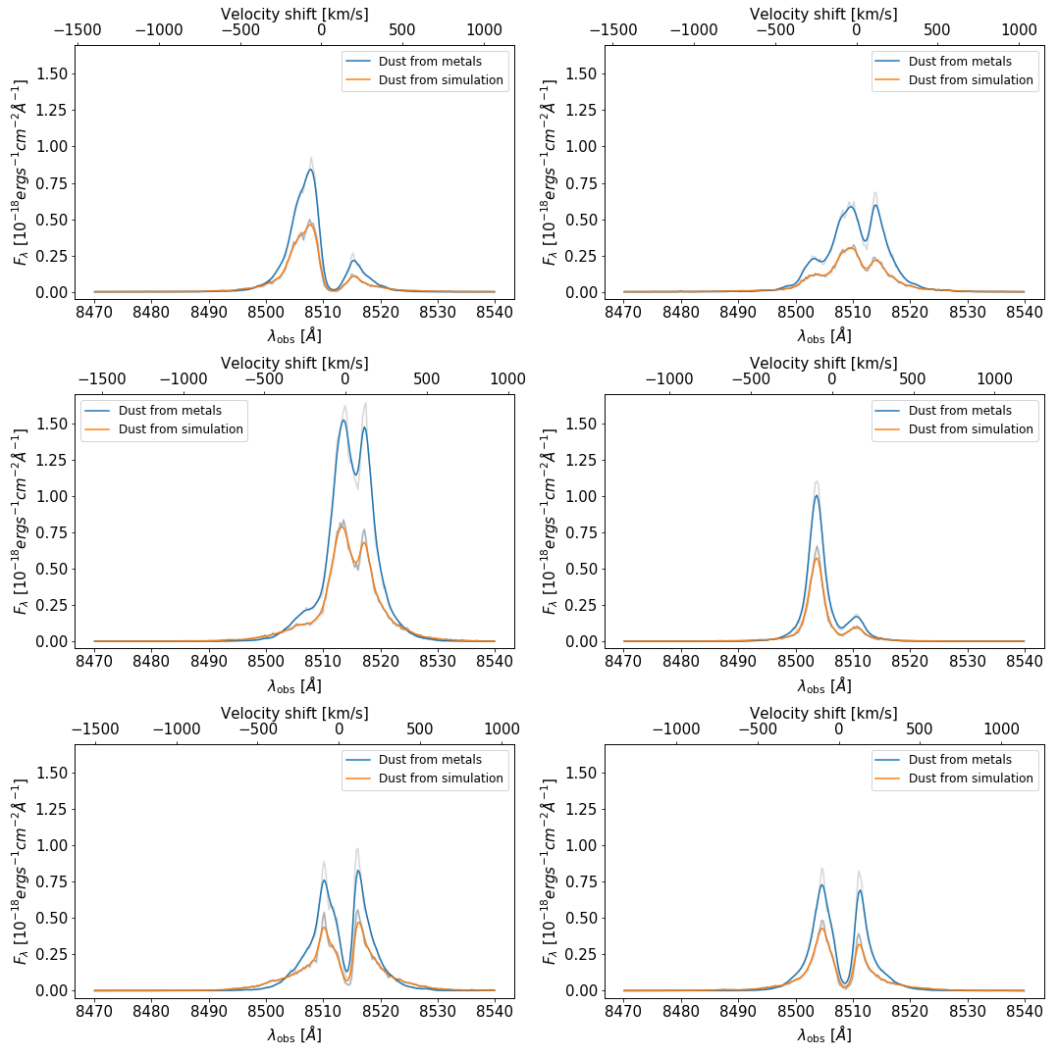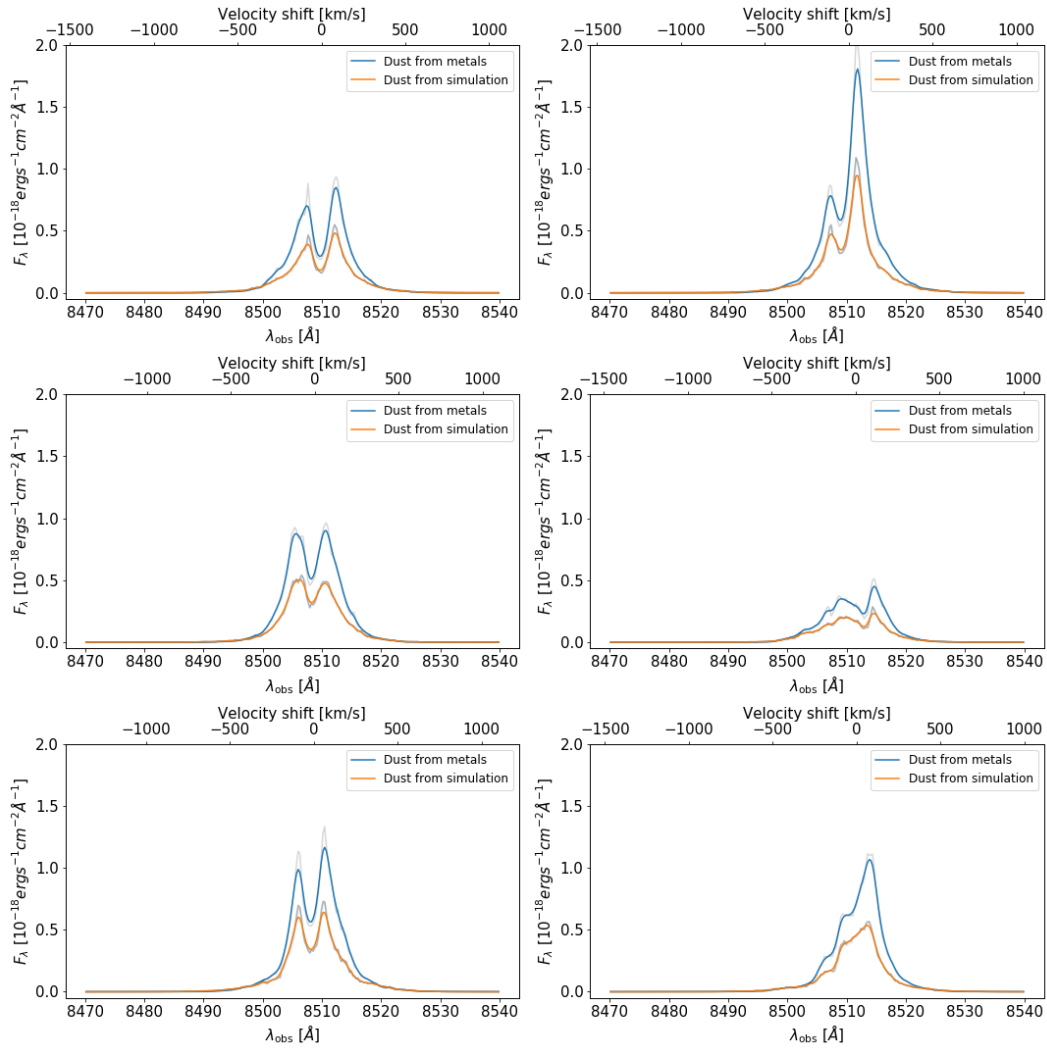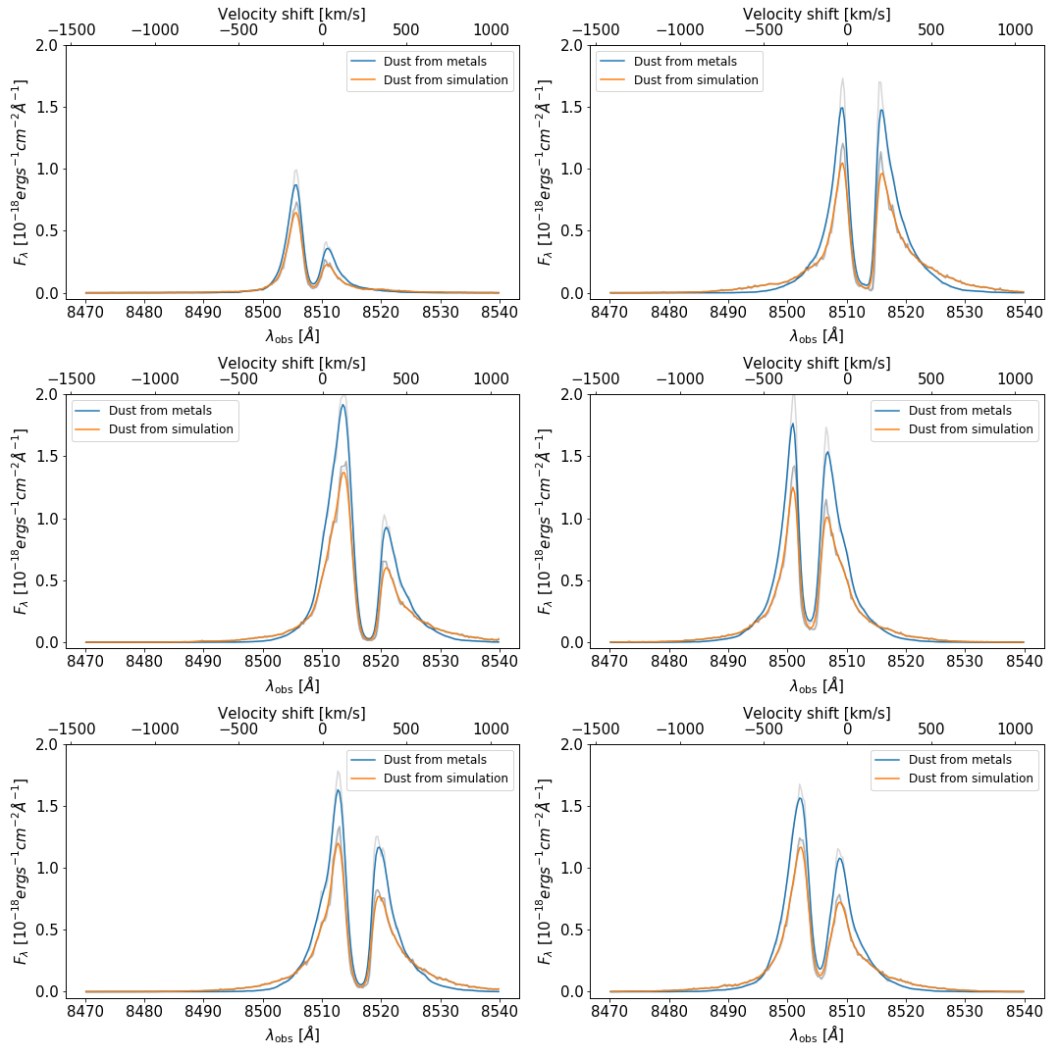
Figure 5.14: Galaxy ID 10345 (sample C)

Figure 5.15: Galaxy ID 57172 (sample C)

Figure 5.16: Galaxy ID 67244 (sample C)